THE EFFECTS OF FILL-NONUNIFORMITIES ON THE DENSIFIED STATES OF CYLINDRICAL GREEN P/M COMPACTS

by

Edward M. Gaboriault Jr.

A Thesis

Submitted to the Faculty

of the

WORCESTER POLYTECHNIC INSTITUTE

in partial fulfillment of the requirements for the

Degree of Master of Science

in

Mechanical Engineering

by

May 2003

APPROVED:

Professor Mark W. Richman, Thesis Advisor

Professor Diran Apelian, Committee Member

Professor Zhikun Hou, Committee Member

Professor John M. Sullivan Jr., Graduate Committee Representative

ABSTRACT

We focus attention on single-punch compaction of metal powders in cylindrical dies. In one case, we consider solid cylindrical compacts, and take the die walls to be frictionless in order to isolate the effects of initial nonuniformities in powder fill on the final green density distribution of the compact. First, a model is introduced in which the die is filled with *n* distinct powders that occupy concentric annular regions within the die. The model requires that the balance of mass, the balance of momentum, and a realistic equation of state be satisfied in each region, and includes a plausible constitutive relation that relates the induced radial pressure in each powder region to the corresponding axial pressure and the relative movements of the interfaces that confine the region. For specified powder properties, the model predicts the movements of the interface between the powders, the final density in each region, the pressure maintained in each region, and the total compaction load required. In the special case of two powders (n=2), we predict how the radial movement of the single interface depends on the mismatch between the properties of the two powders. For large values of *n*, and for powder properties that change gradually from one powder to the next, the model approximates a single powder filled nonuniformly in the die. Finally, a model is developed for a single powder with continuously varying powder properties. Formally, the model may be obtained by taking the limit of the *n*-powder model as *n* becomes unbounded. Employing the continuous model, we determine how nonuniformities in initial fill density can be offset by nonuniformities in other powder properties to yield perfectly uniform green densities.

In a second case, we consider axisymmetric, hollow, cylindrical compacts, and include the effects of friction at the die wall and the core rod. The ratio of the induced radial pressure to the applied axial pressure is assumed to be constant throughout the compaction, and Coulomb friction acts between the powder and the die wall as well as between the powder and the core rod. We derive a closed form solution for the axial and radial variation of the axial pressure, radial pressure, and shear stress throughout the compact. This solution is combined with a plausible equation of state to predict the final green density distribution and the variation of applied load throughout the compact.

ACKNOWLEDGEMENTS

This work was funded by the Powder Metallurgy Research Center (PMRC) of the Metal Processing Institute (MPI) at Worcester Polytechnic Institute (WPI). The author is grateful to all the industrial members of the PMRC for their support. In particular, I would like to acknowledge the technical insights provided by George Jucha of Ametek, Inc., Bill Jandeska of General Motors Corporation, Owe Mars of Hoganas North America, Inc., Sim Narasimhan of Hoeganaes Corporation, and Juan Trasorras of Federal-Mogul Sintered Products. In addition, I would like to thank the director of MPI, Diran Apelian, for his technical expertise and constant encouragement.

Special thanks goes to my thesis advisor, Mark W. Richman. His wisdom, patience and direction were instrumental in the preparation of this document. I would also like to thank John M. Sullivan Jr. and Zhikun Hou for their participation in the defense process.

This document would not have been completed were it not for the friends and family I hold most dear. I would like to thank Charlie Morse, Jason Bacon, Kate McCorry, Philippe Le Menn, and Jocelyn and Peter Sherman for their faith and kind words. I would especially like to thank my love, Katie Archambault. Her patience during the preparation of this document was nothing short of amazing. She believed in me when I did not. Above all, I would like to thank my parents, Edward and Mary Gaboriault, for their support, understanding, encouragement, and sacrifice.

TABLE OF CONTENTS

LIST OF FIGURES

Chapter 1

Chapter 2

Chapter 3

Chapter 4

CHAPTER 1

Introduction

Powder Metallurgy (P/M) encompasses a diverse set of near net-shape manufacturing processes that convert elemental or alloy metal powders into useful engineering components. There are five operations central to the powder metallurgy process.

The first step in the P/M process is powder production. Typically less than 1mm in size, powder particles are produced with a wide range of techniques, depending on the desired size, shape, and composition of the bulk powder. Commonly used powder production techniques include atomization, reduction, electrolytic deposition, mechanical comminution, and mechanical alloying.

The second step is powder blending. Metal powders of different sizes and types are often blended together to yield parts with specified strength, hardness, and porosity. Oftentimes an organic lubricant is incorporated during blending to facilitate compaction and ejection.

The third step is powder consolidation. Pressure is applied to the blended powder to create parts with densities higher than the apparent density of the powder. The most popular consolidation technique used today is uniaxial compaction. Other methods of consolidation include isostatic pressing, extrusion, and metal injection molding.

The fourth step is sintering. Before it can be used for commercial applications, the P/M part is heated without melting (sintered) to remove lubricant and create metallurgical bonds between individual powder particles. The inter-particle bonds created during sintering enhance the physical and mechanical properties of the part.

When the sintered part does not fulfill its engineering requirements, it is subjected to secondary finishing operations. This is the fifth and final step of the P/M process. Finishing operations are used to improve dimensional tolerances, refine surface finish, increase strength and hardness, or modify microstructure. Common finishing operations include repressing via coining or sizing, impregnation with oil or resin, heat treating, and machining.

This thesis is concerned with powder metal compacts produced by uniaxial compaction in a rigid die. The typical compaction apparatus consists of a metal die and an upper and lower punch. For instances where more complex parts are required, core rods are positioned within the die to create holes or internal steps in the compact. The compaction process begins when a feed shoe delivers a controlled quantity of metal powder to the die. After filling, the upper punch moves towards the lower punch to compact the powder bed. If the lower punch is stationary, this process is called single-action pressing. If both punches are moving toward each other, the process is called double-action pressing. When a desired pressure or compaction height is obtained, the upper punch is withdrawn and the lower punch moves upward to eject the pressed green part. The green part is strong enough to be handled, but not strong enough for engineering use. Once the part is ejected, the bottom punch is lowered and the feed shoe moves back over the die to deliver powder for another part. A diagram detailing the compaction phase of the P/M process is shown in Figure 1.1.

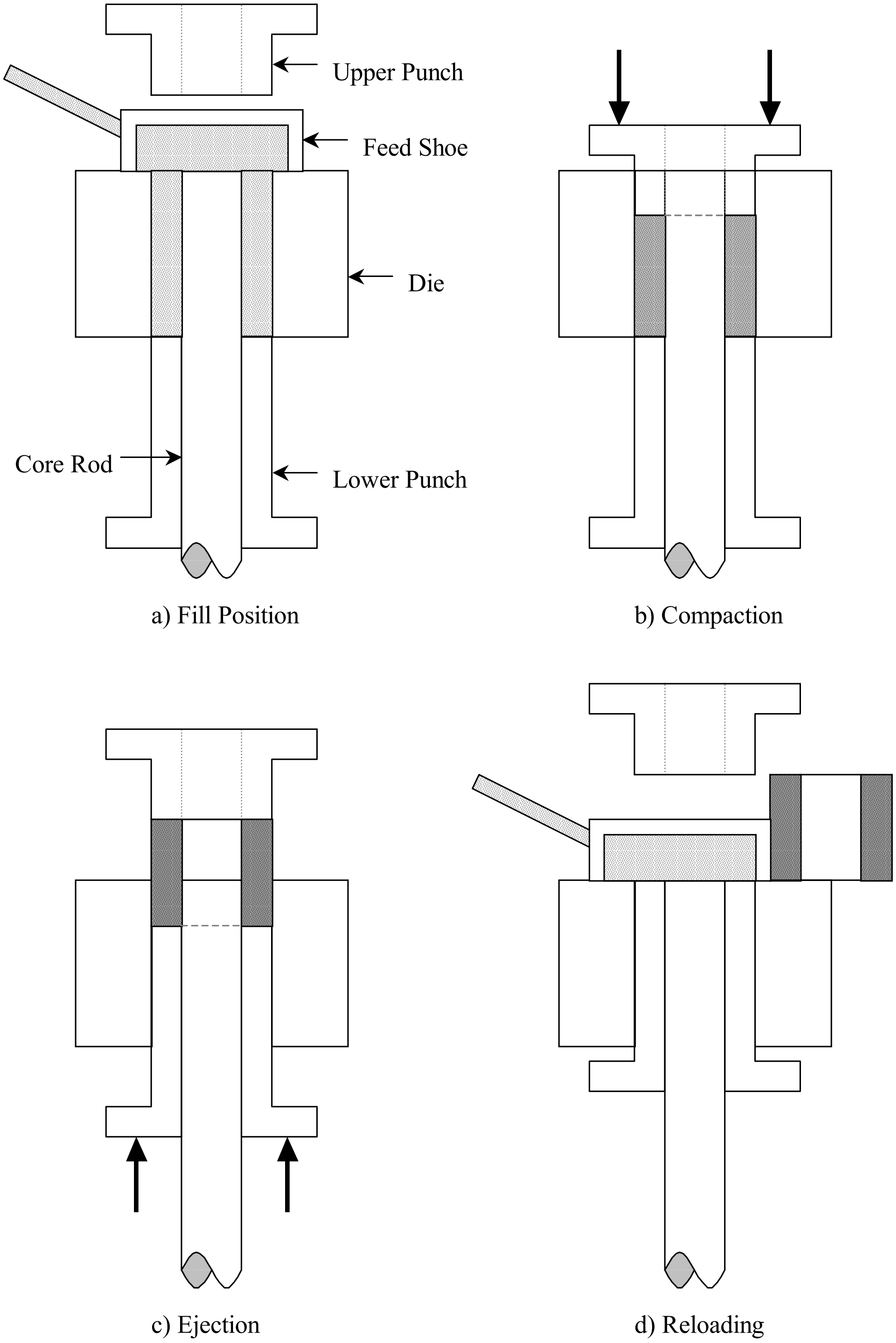

a) Fill Position b) Compaction

c) Ejection d) Reloading

Figure 1.1: Diagram of the powder metal compaction process.

The density distribution of the green compact is of particular interest because less dense regions are inherently weaker and will shrink more readily during sintering than regions of higher density. Such differences in behavior can lead to microcracks that ultimately undermine the strength of the part after repeated engineering use. Nonuniformities in green density are caused primarily by nonuniform powder filling before compaction and friction between the die wall and the powder during compaction.

1.1 Review of Previous Work

A fundamental understanding of the physical mechanisms that govern powder compaction is central to the economics of the P/M process. Hence, compaction modeling has received significant attention over the years. There are two main approaches to compaction modeling. "Micro-mechanical" or discrete element models (DEM) consider the discrete nature of the powder particles. These "particulate" models describe how the basic physical laws affect the movement of individual powder particles. "Macro-mechanical" models, on the other hand, treat the powder mass as a continuum. These continuum models describe how the pressure and density distributions within the compacting powder bed depend on relevant powder properties and geometry of the compaction apparatus.

Micro-mechanical modeling describes the particle-particle and particle-wall interactions that take place when powder is compacted. Information pertinent to such modeling may include the average number of contacts, volume fraction of particles, contact area, and center-to-center distances of adjacent particles. Micro-mechanical modeling was initially applied to the mechanics of soils and rocks and later to the flow of granular media in industry. Cooper and Eaton [1962] were among the first to use micro-mechanical models to describe the compaction of powder metals. They characterized compaction as two separate probabilistic processes, the filling of large voids by sliding and the filling of small voids by plastic flow. Today, the micro-mechanical model is used primarily to determine the local yield behavior of complex powders. For example, Fleck et al. [1992] used a micro-mechanical model to study the yielding of a metal powder bonded by isolated contacts. The primary drawback of the micro-mechanical model is its computational expense. To accurately model the interplay of adjacent powder particles during compaction, an extremely small time step must be used. On today's fastest supercomputers, it is possible to simulate the compaction of only a few thousand particles. Consequently, micro-mechanical modeling is insufficient to characterize the global behavior of a compacting powder mass.

The macro-mechanical approach is the predominant modeling technique for powder metal compaction. Whereas the micro-mechanical model provides information about the local behavior of a powder, the macro-mechanical model provides useful engineering information such as density distribution and post-compaction shape. Mathematically, macro-mechanical models involve the solution of a boundary value problem with partial differential equations for equilibrium, compatibility, and a material-dependent constitutive relation. The finite-element-method (FEM) is the most common numerical technique used to solve this system of equations. Less common solution techniques include the finite-difference-method (FDM), and the boundary-element-method (BEM).

Aydin et al. [1997] characterize macro-mechanical models as either first-order, elasticity, or plasticity models. The first-order model is a low dimensional model that determines stress from equilibrium, and relates pressure to density without explicit consideration of deformation. The first-order model was conceived over a century ago when Janssen [1895] described the compaction of powder in a cylindrical container. Walker [1966] modified this solution and proposed what is the now classical Janssen-Walker analysis. A variation of the Janssen-Walker analysis is presented by German [1994] in his introductory powder metallurgy text. Thompson [1981] presented a more detailed first-order model that addresses both the axial and radial variations of pressure and density in the green compact.

Elasticity models are multi-dimensional models that relate an increment in stress to an increment in strain. The factor of proportionality for this relation is typically not constant and often depends on the strains themselves. Thus, elasticity models for powder compaction are inherently nonlinear. Mroz and Zeinkiewicz [1984] discuss elasticity models for powder compaction in their comprehensive mechanics of materials textbook. First-order models and elasticity models are simple, easy to implement, and highlight the underlying physics of compaction. Input data is readily obtained by testing the bulk stress-strain behavior of the powder. These models are sufficient to model the final state of the compact while still under the pressure of the compacting punch, but they cannot deal effectively with unloading and they offer no insight into the mechanisms that characterize the densification of a compacting powder.

Plasticity models consist of an elastic stress-strain relation and a flow rule or yield criteria that specifies how the deforming powder transitions from an elastic state to a plastic state. Yield criteria for macro-mechanical plasticity models are chosen empirically based upon observed stress-strain behavior. If the powder being compacted is ductile and loaded monotonically, a continuous, quadratic yield function is often used. Work done in this regard includes Shima [1975], Morimoto et al. [1982], Trasorras et al. [1994], Trasorras et al. [1995], and Krishnaswami and Trasorras [1995]. Cap models are used to model complex powders subjected to complex loading conditions. These models have two yield surfaces, one for shear failure and another for hardening. Various examples of cap models include Crawford and Lindskog [1983], Trasorras et al. [1989], Watson and Wert [1993], Gethin et al. [1995], and Chtourou et al. [1996]. Unlike less sophisticated models, plasticity models can handle the complex loading and unloading that characterizes real-world powder compaction. Unfortunately, these models are mathematically complex and extensive testing must be done to determine the required material properties.

1.2 Summary of Approach

In Chapter 2, we examine the effects of radial inhomogeneities introduced by nonuniform pre-compaction powder filling on post-compaction green density distributions. In typical compaction analyses (for comprehensive reviews see Thummler and Oberacker [1993], German [1994], Aydin et al. [1997], and Trasorras et al. [1998]), the metal powder is assumed to be distributed uniformly throughout the die prior to compaction. Under these idealized conditions, the resulting nonuniformities in green density are caused entirely by the shear stresses and pressure gradients induced by die wall friction. However, in practice, due to such effects as uneven fill and particle size segregation, the initial fill itself is never perfectly uniform. In order to focus entirely on the effects of the initial nonuniformities, we neglect die wall friction, and present a model for the compaction of initially inhomogeneous powders in smooth cylindrical dies. Single powders with continuously varying inhomogeneities are approximated by n concentric, annular, regions occupied by powders with n distinct sets of powder properties. The model requires that the balance of mass, the balance of momentum, and a realistic equation of state be satisfied in each region, and includes a plausible constitutive relation that relates the induced radial pressure in each powder region to the corresponding axial pressure and the relative movement of the interfaces that confine the region. For prescribed compaction loads, die geometries, and initial inhomogeneities, the model predicts the final green density distributions, the variation of the axial pressures throughout the compact, the induced radial and tangential pressures, and the final locations of the interfaces that confine each region. As a special case, we set n=2 so that compaction behavior of two-powder parts can be observed. In particular, we focus on how material differences between the two powders effects the radial location of the interface that separates them.

In Chapter 3, we develop, from first principles, a model for a single powder with powder properties that vary continuously in the radial direction. This model may also be obtained by taking the appropriate limit of the discrete *n*-powder model presented in Chapter 2. We employ the model to further demonstrate how radial variations in powder properties prior to compaction effect the density distribution of a green compact. Of greater significance are solutions to the inverse problem, in which we purposely introduce certain pre-compaction inhomogeneities in order to offset the effect of others. The intention is to have the interactions between all the inhomogeneities neutralize one another to yield perfectly uniform green densities.

In Chapter 4, we present the results of a relatively simple model that predicts both the axial and radial variations of the pressure and density throughout hollow, cylindrical, bushing-like parts just after compaction. The model satisfies axial and radial force balance throughout the compact, employs a Coulomb friction law at the core rod and at the outside die wall, and assumes a simple relation between the axial and radial pressures. We employ the model to predict the dependence of pressure and green density distributions on die wall friction, core rod friction, geometry of the compact, and relevant powder properties. Such a solution for hollow cylindrical geometries is important because bushings and guide valves are, in themselves, common powder metal parts. Moreover, closed form solutions that apply to relatively simple geometries are valuable for comparison to experimental results on similar geometries, and for verification of numerical codes that may in turn be used on more complex geometries.

Our approach in Chapter 4 is influenced heavily by the approach taken by Thompson [1981] in his model for compaction of solid cylindrical parts in frictional dies. The model has the advantage of simplicity (which we have retained), but contains several flaws (which we have repaired). The flaws in Thompson's model may be summarized as follows. First, while symmetry dictates that the shear stress at the centerline must vanish, Thompson incorrectly assumes that the gradient of the shear stress in the radial direction also vanishes at the centerline. This, in turn, forces Thompson's model to predict that the pressure and therefore the density is constant along the centerline of the part, and that the shear stress is proportional to the cube of the radial distance. The first of these predictions is clearly inconsistent with long known experimental results (see, for example, Duwez and Zwell [1949]). Second, it is based on the *a priori* assumption that the distribution of pressure on the upper face of the part varies parabolically with radial distance from the centerline of the compact. Although experimental results indicate that pressure increases monotonically with radial distance from the centerline on the top surface of the compact, the assumption that the variation is parabolic is unduly restrictive. Third, Thompson employs the additional assumption that if the pressure on the upper face is parabolic, then so too is the pressure at any axial distance from the top surface. While it is possible to satisfy axial equilibrium under these strict assumptions, it is not possible to also satisfy radial equilibrium. As a result, Thompson's model ignores the radial equilibrium equation. Fourth, in order to obtain a complete solution, Thompson employs two mass conservation equations. One applies to the whole compact, and is clearly correct. However, the second applies to a differential cylinder about the centerline of the compact, and implicitly assumes that there is no radial strain at the centerline during compaction. Finally, because Thompson's ad hoc approach is developed only for solid cylinders, there is no clear way to generalize it to hollow cylinders. In particular, Thompson's model does not contain the flexibility to satisfy the shear stress conditions on both the inner and outer die walls of a hollow cylinder.

CHAPTER 2

Compaction In Frictionless, Cylindrical Dies:
n-powder Compacts

2.1 Balance of Mass and Momentum

We are concerned here with a cylindrical die of radius b that is filled before compaction with n distinct powders of apparent densities η_i (for i=1 to n). The first powder (for which i=1) occupies a solid inner cylindrical region of radius r_1, and the remaining powders (for which i=2 to n) occupy progressively larger annular regions of the inner radii $r_{i\text{-}1}$ and outer radii r_i. Defined in this manner, the outer radius r_n of the n^{th} powder is identical to the radius b of the die. In principle, the powders can have distinct properties. When n=2, for example, we will vary the properties of the two powders and track the movement of the interface between them during compaction to determine the effects of each property. For larger values of n, the array of n powders will be used to approximate a single powder with properties that vary continuously due to nonuniform filling.

The powders are compacted by a total axial force F, which induces pressure distributions throughout the powders denoted by p_i (i=1 to n). Before compaction the die is filled to a height L, and after compaction the height of the compact is H. The green densities of the n compacted regions are ρ_i, and the interface between the i^{th} and the $(i+1)^{\text{th}}$ regions is located at a radius denoted by a_i. Because the die wall is assumed to be rigid, the interface location a_n between the n^{th} region and the wall must be equal to r_n and b. The pre- and post-compaction states are shown in Figures 2.1 and 2.2.

If throughout the compact there were no expansion or contraction in the radial direction, then the final interface locations a_i would equal the corresponding initial locations r_i, and the green densities ρ_i would increase linearly with decreasing H from the apparent densities η_i. However, in general, the interface locations a_i will be unequal to r_i. Differences between a_i and r_i are important because they describe radial movements that yield densities that can differ by several percent from the corresponding densities that would result in the absence of such movements. An exact determination of the interface locations is complex because the movement of *each* interface will depend on the compressive properties of *all n* powders, as well as on their tendencies to expand radially when subjected to axial pressures. For each powder, both the compressive property and the tendency to expand radially are measured by powder properties that we will introduce shortly.

If the initial fill were perfectly uniform, friction forces exerted on the powder by the die wall would produce nonuniformities in the green density distribution. On the other hand, even if the die wall were frictionless, nonuniformities in the initial fill would produce nonuniformities in the green density distribution. Because the purpose of this chapter is to focus on the latter of these phenomena, the die wall is taken to be frictionless in all that follows. Under these circumstances, the pressures p_i, the green densities ρ_i, the final interface locations a_i, and the final height H are all unknown constants to be determined as functions of the apparent densities η_i, the applied load F, the filled height

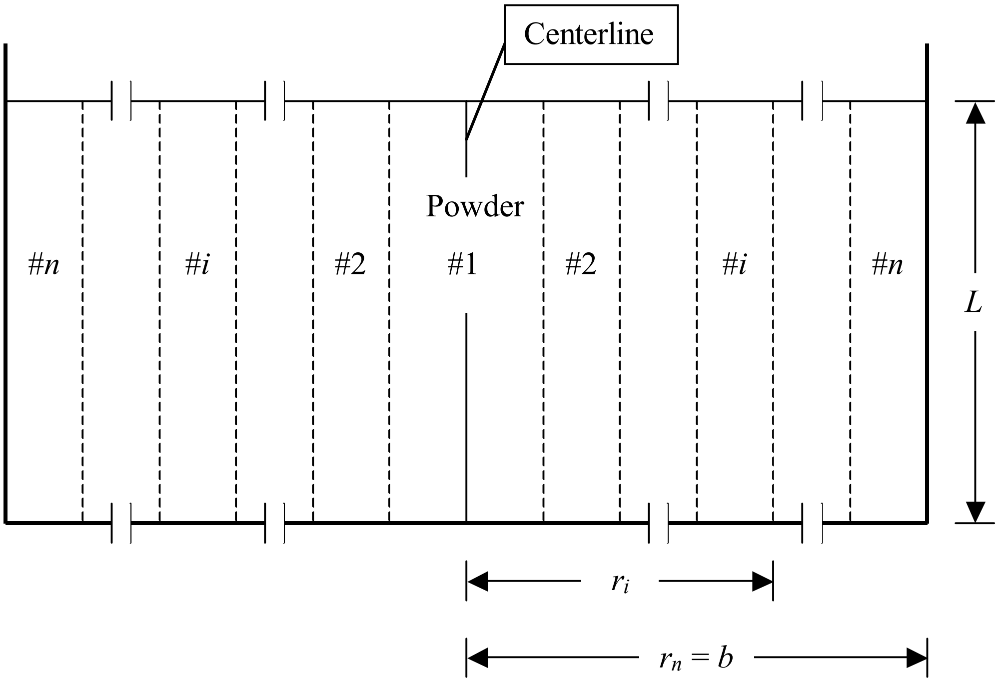

Figure 2.1: Pre-compaction geometry.

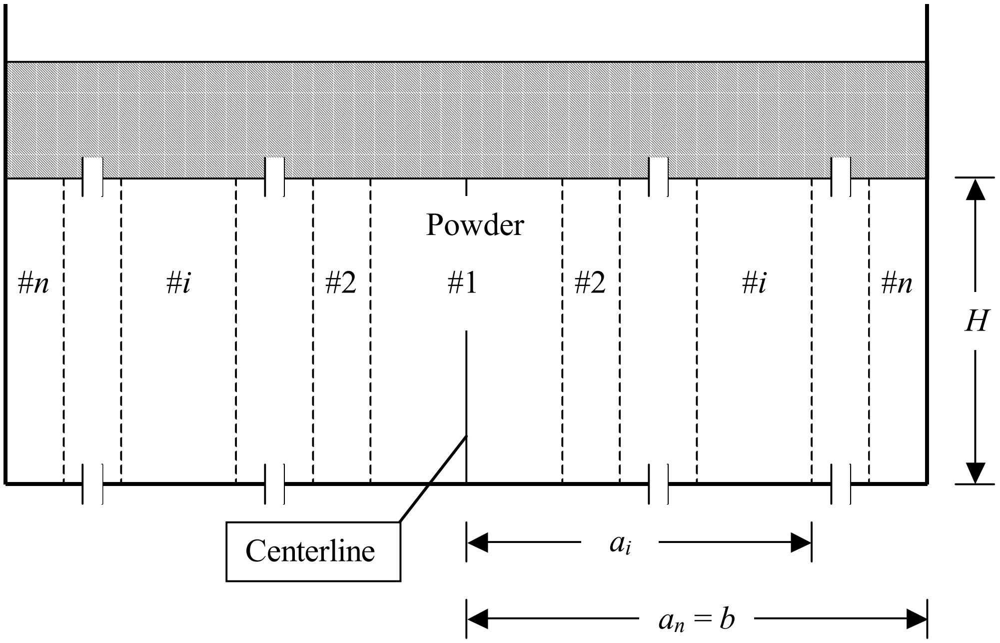

Figure 2.2: Post-compaction geometry.

L, the die radius b, the initial interface locations r_i, and the appropriate material properties of the n powders. For large values of n, the variations of the pressures and densities from one powder to the next are step-wise approximations to the continuous variations that occur in a compact that is produced from a single nonuniform powder. The approximation improves as the number of powders increases.

The interfaces between regions are defined only if there is no mass transferred between regions during compaction. Under these circumstances, the balance of mass requires that the mass in each region before compaction be the same as the mass after compaction. Consequently,

$$\frac{\rho_i}{\eta_i} = \frac{\left(r_i^2 - r_{i-1}^2\right)L}{\left(a_i^2 - a_{i-1}^2\right)H} \quad , \qquad (i=1 \text{ to } n) \qquad (2.1)$$

in which here and what follows $r_0 \equiv a_0 \equiv 0$ because the compact is a solid cylinder, and $r_n \equiv a_n \equiv b$ because the die wall is rigid.

At equilibrium, the total compaction load F applied in the axial direction must be balanced by the corresponding axial loads developed in each region. The individual pressures p_i must therefore be related to the load F according to axial force balance,

$$\pi \sum_{i=1}^{n} \left(a_i^2 - a_{i-1}^2\right) p_i = F \quad . \qquad (2.2)$$

Because the powders tend to expand in both the radial and tangential directions when subjected to axial forces, the presence of axial pressures p_i give rise to corresponding radial pressures σ_i and tangential pressures τ_i. Radial force balance within each region requires that,

$$\sigma_i = \tau_i \quad ; \qquad (i=1 \text{ to } n) \qquad (2.3)$$

radial force balance across each interface requires that,

$$\sigma_i = \sigma_{i+1} \quad . \qquad (i=1 \text{ to } n-1) \qquad (2.4)$$

The tangential momentum balance in each region is identically satisfied.

If the compaction load F, fill height L, initial interface locations r_i, and apparent densities η_i are prescribed, then the $5n$ unknown constants are the compacted height H, the final interface locations a_i (except $a_n \equiv r_n \equiv b$), the green densities ρ_i, the axial pressures p_i, the radial pressures σ_i, and the tangential pressures τ_i. Equations (2.1) through (2.4) are $3n$ equations that by themselves are not sufficient to determine the unknowns.

2.2 Equations of State and Constitutive Relations

Constitutive relations describing the powder behavior in each region are required to complete the system. In each region, an equation of state relates the local value of the density ρ_i to the corresponding values of the total pressure ($p_i + \sigma_i + \tau_i$). A relatively simple equation of state has the form:

$$\rho_i = \eta_i \left[1 + k_i \left(p_i + \sigma_i + \tau_i\right)\right] \quad , \qquad (i=1 \text{ to } n) \qquad (2.5)$$

where the local compressibility k_i of the i^{th} powder is the slope of the variation of ρ_i with $(p_i + \sigma_i + \tau_i)$. However, the local compressibility of each powder is itself a decreasing function of density, so that equation (2.5) actually describes a nonlinear relationship between density and total pressure. As ρ_i increases from the apparent density η_i, the local compressibility k_i decreases monotonically from its initial value β_i. Moreover, as ρ_i approaches its maximum theoretical value D_i, the local compressibility approaches zero. The simplest relation between k_i and ρ_i that satisfies these conditions is

$$k_i = \beta_i \left[1 - \frac{\rho_i - \eta_i}{D_i - \eta_i} \right] \quad . \qquad (i\text{=1 to } n) \qquad (2.6)$$

In what follows, we refer to β_i as the compressibility of the i^{th} powder. By eliminating k_i between equations (2.5) and (2.6), we obtain the following equation of state for the i^{th} powder:

$$\frac{\rho_i}{\eta_i} = \frac{(D_i - \eta_i) + \beta_i D_i (p_i + \sigma_i + \tau_i)}{(D_i - \eta_i) + \beta_i \eta_i (p_i + \sigma_i + \tau_i)} \quad . \qquad (i\text{=1 to } n) \qquad (2.7)$$

In order to write down a constitutive relation for the induced axial pressure σ_i, we first consider the extreme case in which the powders just inside and just outside the i^{th} powder offer no resistance to radial expansion of the i^{th} powder. In this case, the radial pressure σ_i and the tangential pressures τ_i both vanish, and the pair of radial interface locations that enclose the i^{th} powder are denoted by $a_{i\text{-}1}$=$A_{i\text{-}1}$ and a_i=A_i. The relationship between A_i and $A_{i\text{-}1}$ is obtained by using the balance of mass (2.1) to eliminate density from the equation of state (2.7), and by setting σ_i and τ_i equal to zero in the intermediate result. In this manner, we obtain,

$$A_i^2 - A_{i-1}^2 = \frac{L\left(r_i^2 - r_{i-1}^2\right)}{H}\left[\frac{\left(D_i - \eta_i\right) + \beta_i \eta_i p_i}{\left(D_i - \eta_i\right) + \beta_i D_i p_i}\right] \quad , \qquad (i\text{=1 to } n) \qquad (2.8)$$

where $A_0 \equiv r_0 \equiv 0$ and $A_n \equiv r_n \equiv b$.

Equation (2.8) suggests that, in more generality, the value of the radial pressures σ_i depend on the difference $\left(a_i^2 - a_{i-1}^2\right)$. If, for example, $\left(a_i^2 - a_{i-1}^2\right)$ is given by equation (2.8), then σ_i vanishes. On the other hand, if the interfaces containing the i^{th} powder experience no radial movements during compaction, then $\left(a_i^2 - a_{i-1}^2\right)$ is equal to $\left(r_i^2 - r_{i-1}^2\right)$, and the induced radial pressure σ_i is the simple product of the fluidity α_i of the i^{th} powder and the applied axial pressure p_i, so that $\sigma_i = \alpha_i p_i$. Defined in this way, the fluidity α_i generally measures the tendency of the i^{th} powder to expand radially when compacted axially. If, in particular, the i^{th} powder is confined within a rigid annulus, then α_i gives the ratio of the induced radial pressure to the applied axial pressure. In general, therefore, we expect that values of fluidity vary between 0 and 1. When $\alpha_i = 0$, the i^{th} powder has no tendency to expand radially when compressed axially. When $\alpha_i = 1$, the powder is incompressible and the radial pressure induced in a rigid annulus is exactly equal to the applied axial pressure.

In what follows, we generalize the relationship $\sigma_i = \alpha_i p_i$ to cases in which the inner and/or outer interfaces of the annulus containing the i^{th} powder move radially inward or outward. We use simple interpolation between the values of σ_i=0 when $\left(a_i^2 - a_{i-1}^2\right) = \left(A_i^2 - A_{i-1}^2\right)$, and $\sigma_i = \alpha_i p_i$ when $\left(a_i^2 - a_{i-1}^2\right) = \left(r_i^2 - r_{i-1}^2\right)$ to model the dependence of the radial pressure on the corresponding axial pressure and the location of the interfaces that contain the i^{th} powder. In this manner we obtain,

$$\sigma_i = \alpha_i p_i \left[1 - \Gamma_i\right] \quad , \qquad (i=1 \text{ to } n) \qquad (2.9)$$

in which

$$\Gamma_i = \frac{\left(a_i^2 - a_{i-1}^2\right) - \left(r_i^2 - r_{i-1}^2\right)}{\left(A_i^2 - A_{i-1}^2\right) - \left(r_i^2 - r_{i-1}^2\right)} \quad . \qquad (i=1 \text{ to } n) \qquad (2.10)$$

Although equation (2.9) is obtained from linear interpolation between two known values of σ_i, it actually describes a nonlinear relation between σ_i and p_i because of the dependence of $\left(A_i^2 - A_{i-1}^2\right)$ on p_i described by equation (2.8).

In a typical formulation of the problem, the values of fill height L, axial force F, initial interface locations r_i (including die radius $r_n \equiv b$), fluidities α_i, compressibilities β_i, apparent densities η_i, and maximum theoretical densities D_i are all prescribed. Mass balances (2.1), axial force balance (2.2), radial force balances (2.3) and (2.4), equations of state (2.7), and constitutive relations (2.9) are $5n$ equations that determine the following $5n$ unknowns: the final height H; the final interface locations a_i (i=1 to n-1); the final densities ρ_i (i=1 to n); the axial pressures p_i (i=1 to n); the radial pressures σ_i (i=1 to n); and the tangential pressures τ_i (i=1 to n).

2.3 Forward and Inverse Problems

The algebraic system of equations presented here is nonlinear because of the nonlinear relation between density and pressure described by the equations of state (2.7), and because of the nonlinear relation between axial pressure and radial pressure described by constitutive relation (2.9). Although it is not possible to find explicit algebraic solutions for each of the unknowns, it is possible to eliminate some of the unknowns and reduce the number of equations that must be solved simultaneously.

To this end, we employ equations (2.3), (2.9), and (2.1), to eliminate τ_i, σ_i, and ρ_i from equation (2.7). In this manner, the equation of state for the i^{th} powder becomes,

$$\frac{\left(r_i^2 - r_{i-1}^2\right)L}{\left(a_i^2 - a_{i-1}^2\right)H} = \frac{\left(D_i - \eta_i\right) + D_i\left[1 + 2\alpha_i\left(1 - \Gamma_i\right)\right]\beta_i p_i}{\left(D_i - \eta_i\right) + \eta_i\left[1 + 2\alpha_i\left(1 - \Gamma_i\right)\right]\beta_i p_i} \quad . \qquad (i=1 \text{ to } n) \qquad (2.11)$$

In addition, we employ constitutive relations (2.9) to write the radial momentum balances (2.4) across the interfaces in terms of the corresponding axial pressures. In this way we obtain,

$$\alpha_1\left(\frac{\beta_i}{\beta_1}\right)\left(1 - \Gamma_1\right)\beta_1 p_1 = \alpha_i\left(1 - \Gamma_i\right)\beta_i p_i \quad , \qquad (i=2 \text{ to } n) \qquad (2.12)$$

where Γ_i is given by equations (2.10) and (2.8) in terms of the unknowns a_i and p_i.

In the forward problem, we prescribe values of the fluidities α_i, the compressibility ratios β_i/β_1, the apparent-to-maximum density ratios η_i/D_i, the relative locations r_i/b of the interfaces before compaction, and the relative compressed height H/L. Equations (2.11) and (2.12) determine the n dimensionless pressures $\beta_i p_i$ and the n-1 dimensionless post-compaction interface locations a_i/b. Balance of the axial momentum (2.2) then determines the required dimensionless force $\beta_1 F/\pi b^2$; balances of mass (2.1) determine the resulting density ratios ρ_i/D_i; constitutive relations (2.9) determine the resulting dimensionless radial pressures $\beta_i\sigma_i$; and radial momentum balances (2.3) determine the corresponding dimensionless tangential pressures $\beta_i\tau_i$. Solved in this manner, it is necessary only to solve $2n$-1 equations (2.11) and (2.12) simultaneously. The calculations for the remaining $3n$+1 uncoupled unknowns are elementary.

Initial nonuniformities due to uneven fill are approximated by prescribing values of fluidity α_i, compressibility β_i, and apparent density η_i that vary gradually from one region to the next. The solution to the forward problem described above predicts the resulting region-to-region variations in the green compact. Of particular interest are the variations of pressure p_i and green density ρ_i. In the absence of die wall friction, these variations are due entirely to the nonuniformities in initial fill.

Perhaps of even greater interest are the solutions to inverse problems in which certain pre-compaction inhomogeneities are purposely introduced to offset the effect of others. The intention is to have the interactions between all the inhomogeneities neutralize one another to yield perfectly uniform green densities. If, for example, the fluidities α_i and compressibilites β_i vary in known ways due to uneven fill, then it is possible to determine the corresponding variations of the pre-compaction densities η_i that are necessary to yield prescribed uniform densities ρ_i in the green state. To this end, the balance of mass (2.1) is rewritten in the following form:

$$\frac{\eta_i}{D_i} = \left[\frac{\left(a_i^2 - a_{i-1}^2\right)H}{\left(r_i^2 - r_{i-1}^2\right)L}\right]\frac{\rho_i}{D_i} \quad . \qquad (i\text{=1 to } n) \qquad (2.13)$$

In order to solve the inverse problem, we employ equation (2.13) to eliminate η_i wherever it appears explicitly and implicitly (through Γ_i) in equations (2.11) and (2.12). For a desired uniform value of green density ratio ρ_i/D_i, and for prescribed values of α_i, β_i/β_1, r_i/b, and H/L, equations (2.11) and (2.12) modified in this manner determine $\beta_i p_i$ and a_i/b. Balance of mass (2.13) then determines the initial fill density ratios η_i/D_i required to produce the pre-determined uniform green density level. The dimensionless force $\beta_1 F/\pi b^2$, the dimensionless radial pressures $\beta_i\sigma_i$, and the dimensionless tangential pressures $\beta_i\tau_i$ are determined as in the forward problem described above.

2.4 Solution Procedure

In principle, we can solve the set of 2*n*-1 equations that govern either the forward or inverse problems by Newton-Raphson iteration. For brevity, we write equation (2.11) in the form F_i=0 (for *i*=1 to *n*). We rewrite equation (2.12) in the form:

$$\left(\frac{\beta_i}{\beta_1}\frac{\beta_1}{\beta_{i-1}}\right)\left(\frac{\alpha_{i-1}}{\alpha_i}\right)\left(1-\Gamma_{i-1}\right)\beta_{i-1}p_{i-1} = \left(1-\Gamma_i\right)\beta_i p_i \quad , \qquad (i\text{=2 to } n) \qquad (2.14)$$

and write equation (2.14) in the form $F_i=0$ for ($i=n+1$ to $2n-1$), where F_{n+1}, F_{n+2}, …to F_{2n-1} correspond to equation (2.14) for $i=2, 3,$ …to n, respectively.

In addition, we define a new unknown δ_i^2 according to

$$\delta_i^2 \equiv a_i^2 - a_{i-1}^2 \qquad , \qquad (i=1 \text{ to } n) \qquad (2.15)$$

so that

$$F_{2n} \equiv \sum_{i=1}^{n} \delta_i^2 - b^2 = 0 \qquad . \qquad (2.16)$$

In this way, the $2n$ equations have the form:

$$\left.\begin{aligned} F_i &= F_i\left(\delta_i^2, p_i\right) = 0 && ;\ (i = 1 \text{ to } n) \\ F_i &= F_i\left(\delta_i^2, \delta_{i-1}^2, p_i, p_{i-1}\right) = 0 && ;\ (i = n+1 \text{ to } 2n-1) \\ F_{2n} &= F_{2n}\left(\delta_i^2\right) = 0 && \end{aligned}\right\} \qquad . \qquad (2.17)$$

The n-dimensional vector of these functions is denoted by $\mathbf{F}$, with components F_i. The unknowns may also be written as an n-dimensional vector $\mathbf{v}$ in which the components v_i are given by

$$\mathbf{v}_i = \begin{Bmatrix} p_i & \text{for } i = 1 \text{ to } n \\ \delta_i^2 & \text{for } i = n+1 \text{ to } 2n \end{Bmatrix} \qquad . \qquad (2.18)$$

The values of $\mathbf{v}$ at the m^{th} iteration are denoted by $\mathbf{v}_m$ and the values of the function evaluated at $\mathbf{v}_m$ are denoted by $\mathbf{F}_m$.

The Newton-Raphson iteration is based on the repeated use of

$$[\mathrm{J}](\mathbf{v}_{m+1} - \mathbf{v}_m) = -\mathbf{F}_m \quad , \tag{2.19}$$

where $[\mathrm{J}]$ is the Jacobian whose components J_{ij} are the derivatives $\partial \mathrm{F}_i / \partial \mathrm{v}_j$. For known values of $\mathbf{v}_m$, equation (2.19) determines $\mathbf{v}_{m+1}$ via Gauss-Jordan elimination.

2.5 Results and Discussion: Two-powder Compacts (*n*=2)

We have carried out the solution procedure described in Section 2.4 for dies filled with two powders (n=2) in order to study the effects that disparities between α_1 and α_2 and between β_1 and β_2 have on the radial movement of the interface that separates the powders and on the pressures transmitted through each powder. Because there is only one interface location to track, we rename the initial location r_1 of the interface to be r, and the final location a_1 of the interface to be a.

Figure 2.3 shows the variation of the dimensionless interface location a/r with compressibility ratio β_1/β_2, for fluidities α_1=α_2=.5, relative apparent densities η_1/D_1=η_2/D_2=.444, and geometry b/r=2, when H/L=.9, .7, and .5. The difference between the two powders described here is only in their respective compressibilities, β_1 and β_2. When the inner powder is less compressible than the outer powder (i.e. β_1/β_2<1), the inner powder expands and the outer powder contracts radially at any stage of the compaction. When the inner powder is more compressible than the outer powder (i.e. β_1/β_2>1), the radial movements are reversed. Consequently, for any value of H/L during

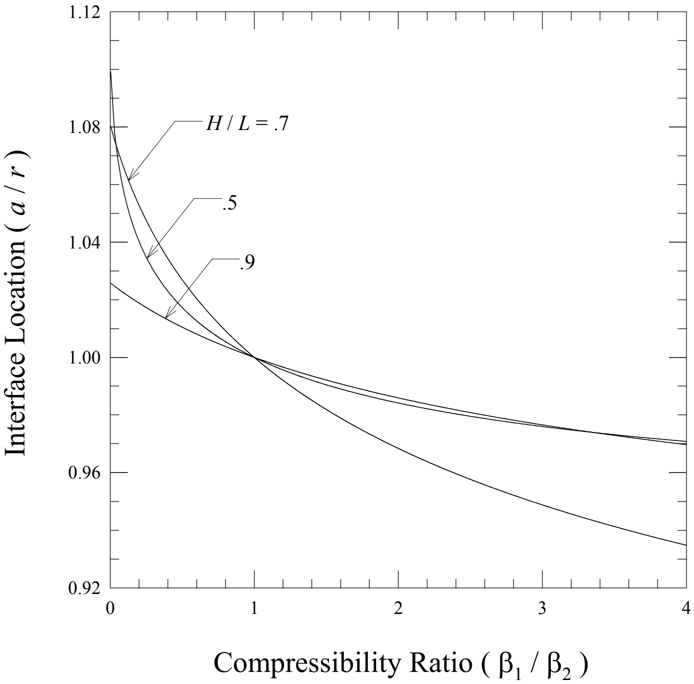

Figure 2.3: The variation of *a*/*r* with β_1/β_2 when $\alpha_1=\alpha_2=.5$, $\eta_1/D_1=\eta_2/D_2=.444$, and *b*/*r*=2, for *H*/*L*=.9, .7, and .5.

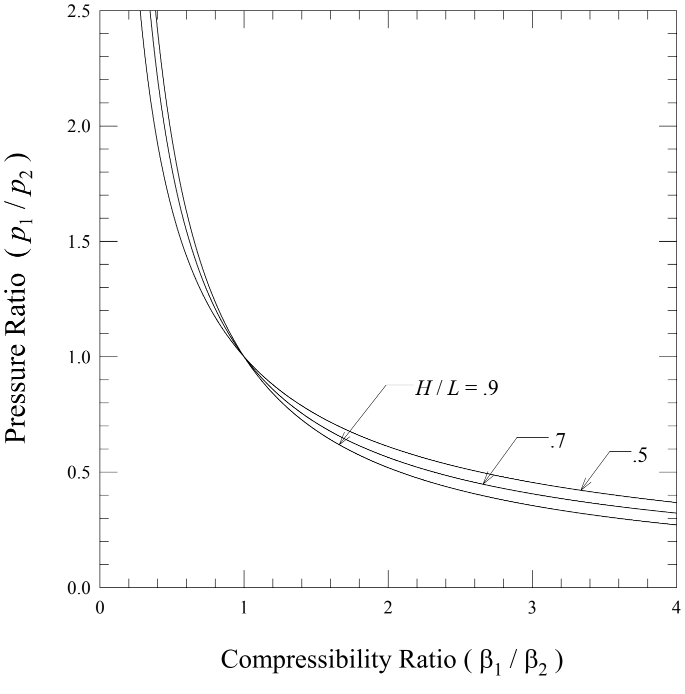

Figure 2.4: The variation of p_1/p_2 with β_1/β_2 when $\alpha_1=\alpha_2=.5$, $\eta_1/D_1=\eta_2/D_2=.444$, and *b*/*r*=2, for *H*/*L*=.9, .7, and .5.

compaction, as β_1/β_2 increases from zero the final radial location a of the interface moves radially inward. When $\beta_1/\beta_2=1$, the powders are identical and the interface location a remains unchanged from its original position r. This result demonstrates that particles in a uniform powder compacted in a frictionless die move in the axial direction only.

In Figure 2.4, we show the corresponding variation of the pressure ratio p_1/p_2. As β_1/β_2 increases, the inner region becomes increasingly more compressible than the outer region. Therefore, as β_1/β_2 increases, the required pressure p_1 in the inner powder decreases relative to the pressure p_2 in the outer powder. When $\beta_1=\beta_2$ (i.e. $\beta_1/\beta_2=1$), the powders are identical, so the axial pressures p_1 and p_2 are equal.

Figures 2.5 and 2.6 show the variations of a/r and p_1/p_2 with β_1/β_2 when $\alpha_1=.75$, $\alpha_2=.25$, $\eta_1/D_1=\eta_2/D_2=.444$, and $b/r=2$, for H/L =.9, .7, and .5. Whereas the powders described in Figures 2.3 and 2.4 had equal fluidities, the fluidity of the inner powder described in this set of figures is greater than the fluidity of the outer powder. Because α_1 is greater than α_2, the inner powder has a greater tendency to expand radially than the outer powder. Therefore, when the compressibilities are equal (i.e. $\beta_1/\beta_2=1$), the inner powder expands outward (i.e. $a/r>1$). In order to offset this tendency, the inner powder must be more compressible than the outer powder (i.e. $\beta_1/\beta_2>1$) for the interface location to remain fixed (i.e. $a/r=1$) during compaction. Interestingly, the value of p_1/p_2 corresponding to no radial movement (i.e. $a/r=1$) is less than 1. This is due to two effects. First, the inner powder is more compressible than the outer powder (i.e. $\beta_1/\beta_2>1$). Therefore, less pressure is required to compact the inner powder than is required to

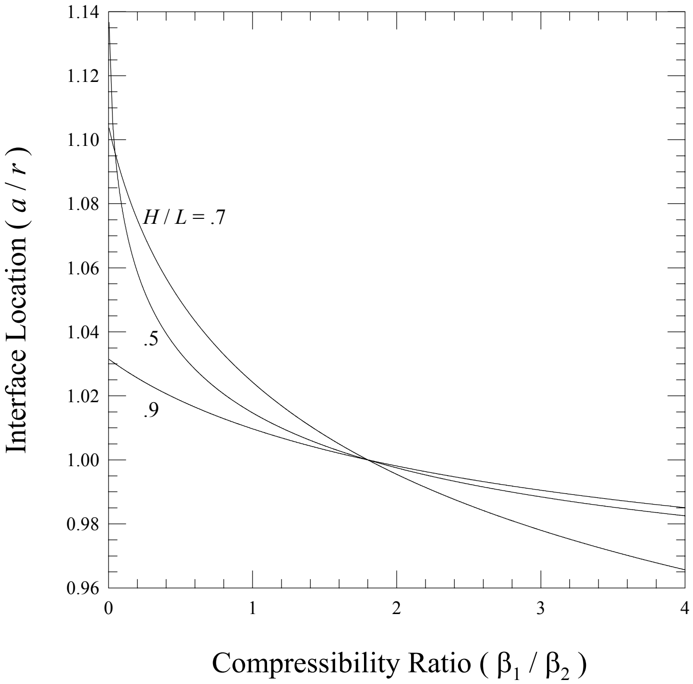

Figure 2.5: The variation of *a*/*r* with β_1/β_2 when α_1=.75, α_2=.25, η_1/D_1=η_2/D_2=.444, and *b*/*r*=2, for *H*/*L*=.9, .7, and .5.

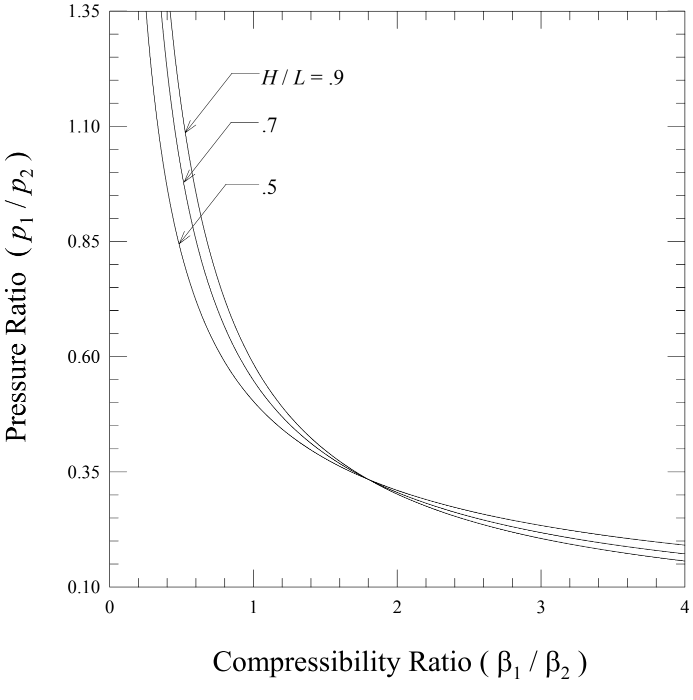

Figure 2.6: The variation of p_1/p_2 with β_1/β_2 when α_1=.75, α_2=.25, η_1/D_1=η_2/D_2=.444, and *b*/*r*=2, for *H*/*L*=.9, .7, and .5.

compact the outer powder. Second, because α_1 is greater than α_2, the inner region has a greater capacity to generate radial pressures in response to axial pressures. Therefore, less axial pressure is required in the inner powder than in the outer powder to satisfy radial equilibrium.

Figures 2.7 and 2.8 show the variations of a/r and p_1/p_2 with β_1/β_2 when α_1=.25, α_2=.75, $\eta_1/D_1=\eta_2/D_2$=.444, and b/r=2, for H/L =.9, .7, and .5. This case differs from that shown in Figures 2.5 and 2.6 because the values of α_1 and α_2 are reversed. Again, both a/r and p_1/p_2 decrease with increasing β_1/β_2, as expected. Here, the inner powder (with α_1=.25) is less inclined to expand radially than the outer powder (with α_2=.75). Thus, the inner powder must be less compressible than the outer powder (i.e. $\beta_1/\beta_2<1$) to ensure that there is no movement of the interface. The value of p_1/p_2 that corresponds to no radial interface movement is greater than 1 because the inner powder is less compressible than the outer powder when a/r=1, and because α_1 is less than α_2.

Figure 2.9 shows the variation of the dimensionless interface location a/r with α_1 when α_2=.5, β_1/β_2=1, $\eta_1/D_1=\eta_2/D_2$=.444, and b/r=2, for H/L=.9, .7, and .5. When α_1 is equal to α_2, the powders are identical and the interface does not move ($a=r$). For values of α_1 less than α_2, the inner powder is less apt than the outer powder to expand radially in response to the applied axial pressure. Under these circumstances, the inner powder contracts radially, and a is less than r. Conversely, when α_1 is greater than α_2, the inner powder is more apt than the outer powder to expand in the radial direction, and a is greater than r.

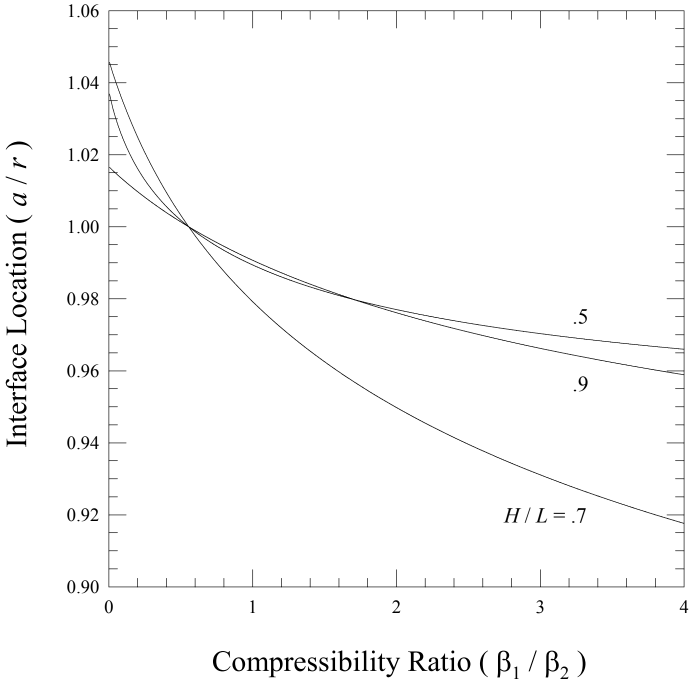

Figure 2.7: The variation of *a*/*r* with β_1/β_2 when α_1=.25 and α_2=.75, $\eta_1/D_1=\eta_2/D_2$=.444, and *b*/*r*=2, for *H*/*L*=.9, .7, and .5.

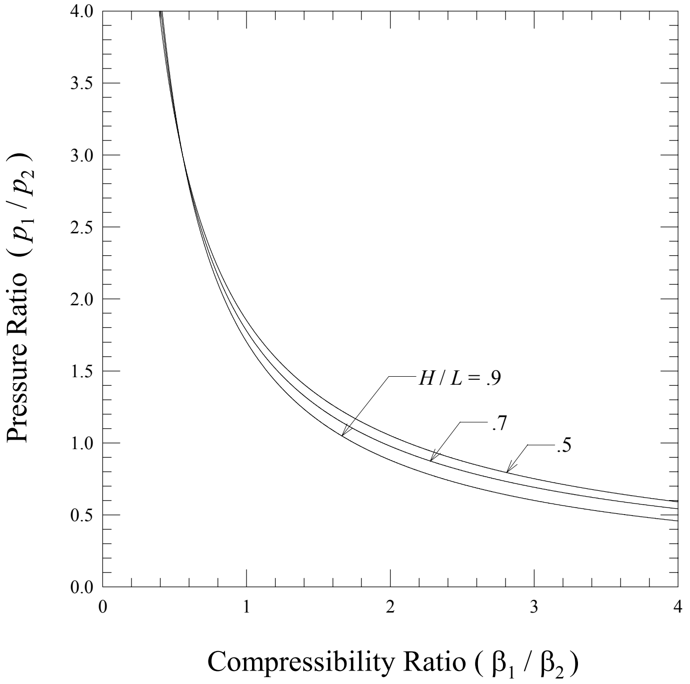

Figure 2.8: The variation of p_1/p_2 with β_1/β_2 when α_1=.25, α_2=.75, $\eta_1/D_1=\eta_2/D_2$=.444, and *b*/*r*=2, for *H*/*L*=.9, .7, and .5.

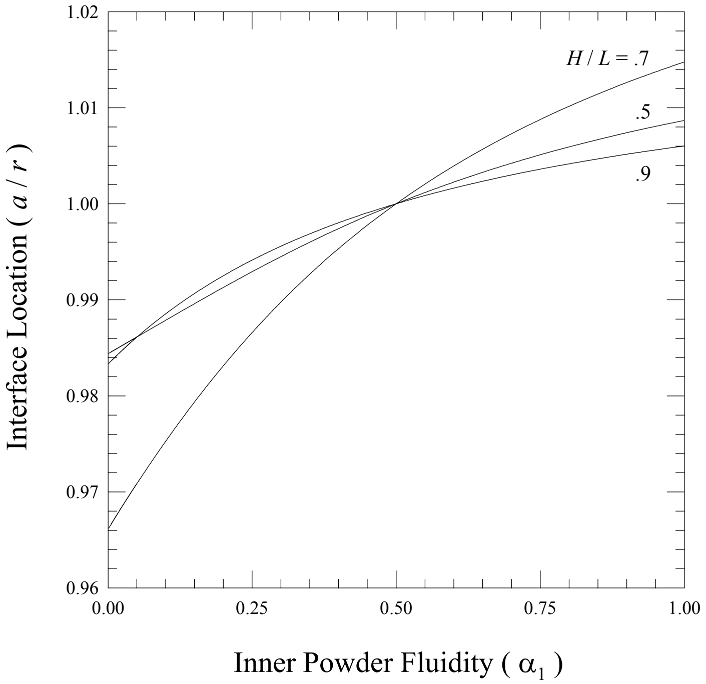

Figure 2.9: The variation of *a*/*r* with α_1 when α_2=.5, β_1/β_2=1, $\eta_1/D_1=\eta_2/D_2$=.444, and *b*/*r*=2, for *H*/*L*=.9, .7, and .5.

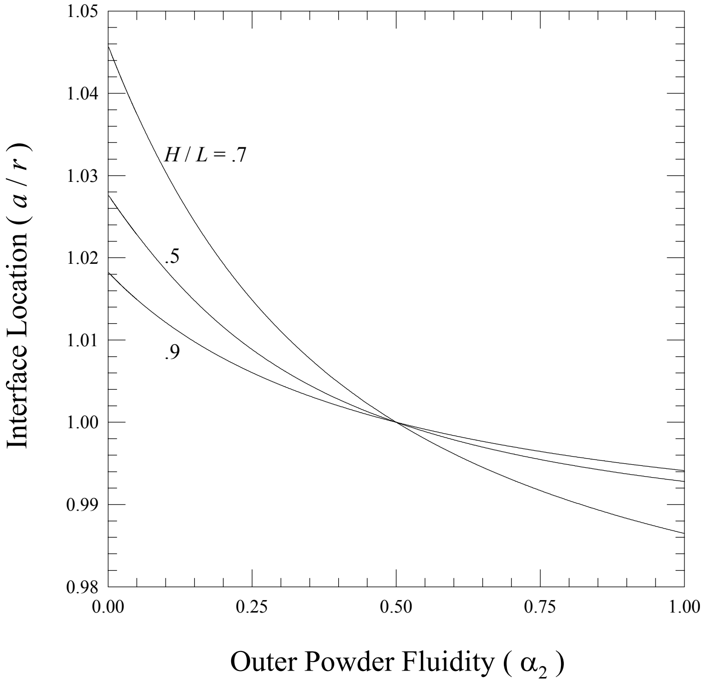

Figure 2.10: The variation of *a*/*r* with α_2 when α_1=.5, β_1/β_2=1, $\eta_1/D_1=\eta_2/D_2$=.444, and *b*/*r*=2, for *H*/*L*=.9, .7, and .5.

Figure 2.10 shows the variation of the dimensionless interface location a/r with α_2 when α_1=.5, β_1/β_2=1, η_1/D_1=η_2/D_2=.444, and b/r=2, for H/L=.9, .7, and .5. As before, when α_1 is equal to α_2, the powders are identical and a is equal to r. With increasing α_2, the tendency of the outer powder to expand radially inward increases. As a result, the outward radial movement of the interface decreases with increasing α_2.

Figures 2.11 and 2.12 show the variations of the pressure ratio p_1/p_2 corresponding to Figures 2.9 and 2.10 respectively. In Figure 2.11, as α_1 increases, the capacity of the inner region to generate radial pressures in response to an applied axial pressure increases. Consequently, the pressure p_1 required to maintain radial equilibrium decreases relative to p_2. By contrast, in Figure 2.12, as α_2 increases the capacity of the outer region to generate radial pressure increases in response to an axial pressure. Thus, the required value of p_2 decreases relative to p_1.

Interestingly, Figures 2.3, 2.5, 2.7, 2.9, and 2.10 all demonstrate that the variation of a/r with the height ratio H/L is not monotonic. In Figure 2.13, we show the variation of a/r as H/L varies continuously from 1 to .4, when α_1=α_2=.5, β_1/β_2=1, η_1/D_1=.444, and b/r=2, for η_2/D_2=.4, .444, and .5. Here, the powders differ only in their relative apparent density ratios. When η_2/D_2=.444, the powders are identical and the location of the interface remains fixed as the compaction proceeds. For values of η_2/D_2 (i.e. η_2/D_2=.5) that are greater than η_1/D_1 (=.444), the outer powder is initially closer to its maximum density and therefore less compressible than the inner powder. Consequently, the outer powder expands radially, and a/r is less than 1. As the interface continues to move

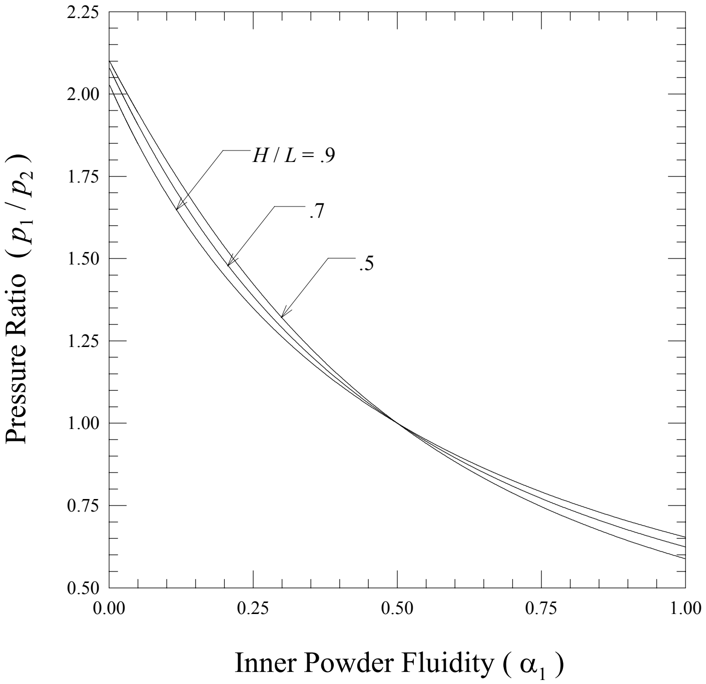

Figure 2.11: The variation of p_1/p_2 with α_1 when α_2=.5, β_1/β_2=1, η_1/D_1=η_2/D_2=.444, and b/r=2, for H/L=.9, .7, and .5.

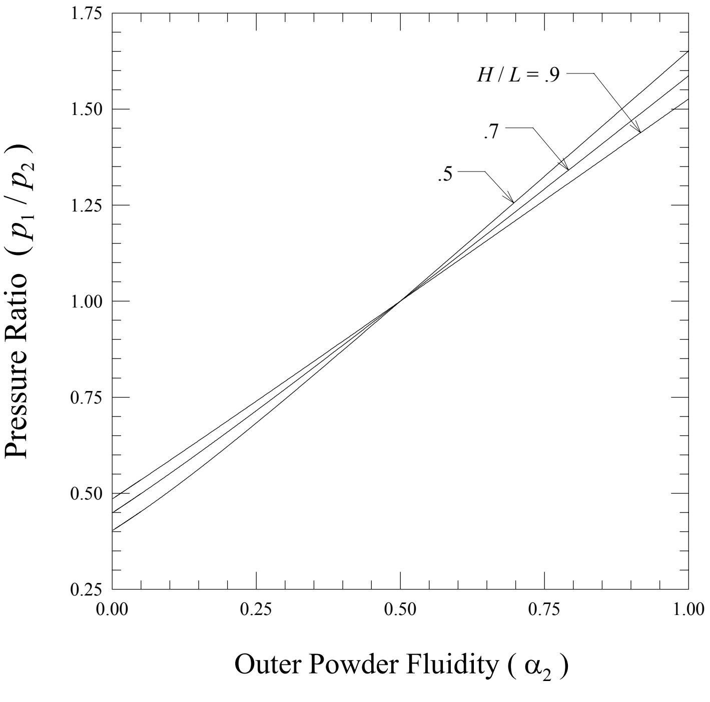

Figure 2.12: The variation of p_1/p_2 with α_2 when α_1=.5, β_1/β_2=1, η_1/D_1=η_2/D_2=.444, and b/r=2, for H/L=.9, .7, and .5.

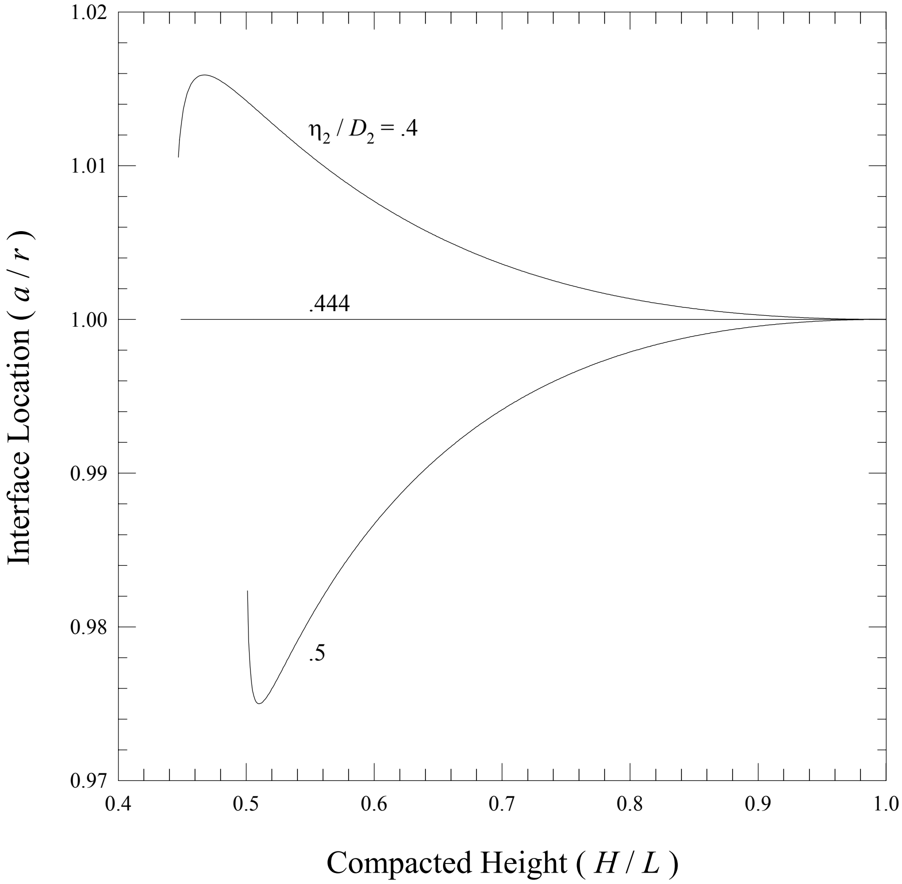

Figure 2.13: The variation of *a*/*r* with *H*/*L* when $\alpha_1=\alpha_2=.5$, $\beta_1/\beta_2=1$, $\eta_1/D_1= .444$, and $b/r=2$, for $\eta_2/D_2=.4$, .444, and .5.

radially inward, the inner powder densifies more quickly than the outer powder. Eventually, the inner powder is closer to its maximum density than the outer powder. Beyond this point, the inner powder is less compressible than the outer powder so the interface begins to move radially outward towards its initial position. For the case in which η_2/D_2 is less than η_1/D_1, the inverse behavior is observed.

Figure 2.14 shows the variation of a/r with H/L when α_1=.75, α_2=.25, β_1/β_2=1, η_1/D_1=.444, and b/r=2, for η_2/D_2=.4, .444, and .5. Whereas in Figure 2.13 the fluidities of the two powders were equal, here the fluidity of the inner powder is greater than that of the outer powder. In this case, even when η_1/D_1 and η_2/D_2 are equal (=.444), the interface moves outward because α_1 is greater than α_2. However, the radial movement of the interface causes the density of the outer powder to increase more rapidly than the density of the inner powder. As it becomes more dense, the outer powder becomes less compressible than the inner powder. Eventually, the decrease in compressibility reverses the effects of the fluidities, and the interface moves radially inward. When η_2/D_2 is less than η_1/D_1, greater inward radial movement is required to reverse the effects of the fluidities because the outer powder is initially less dense than the inner powder. By contrast, when η_2/D_2 is greater than η_1/D_1, less inward radial movement is required to reverse the effects of the fluidities because the outer powder is initially more dense than the inner powder. Interestingly, when η_2/D_2=.5, the decrease in compressibility associated with the densification of the outer powder causes the interface to return to its initial position at H/L=.556. As H/L decreases beyond .556, the interface moves radially inward, the inner powder densifies more rapidly than the outer powder,

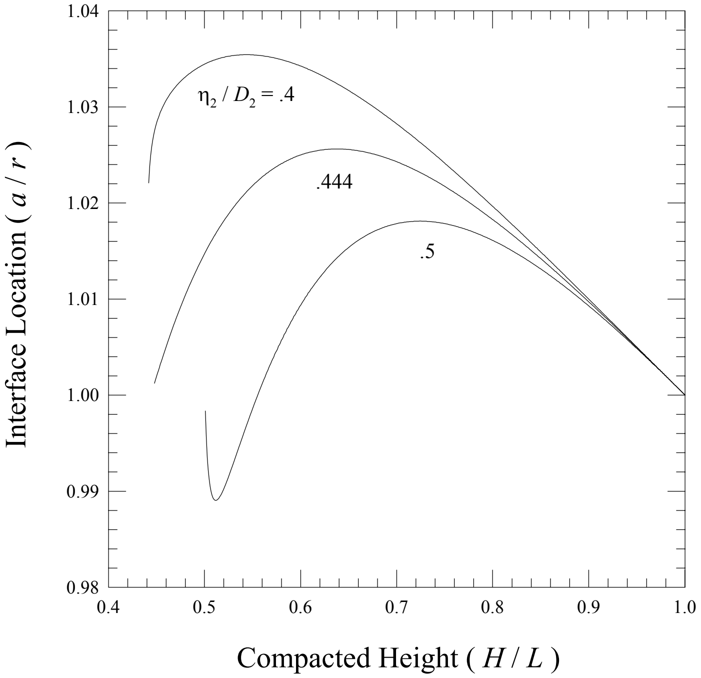

Figure 2.14: The variation of *a*/*r* with *H*/*L* when α_1=.75, α_2=.25, β_1/β_2=1, η_1/D_1=.444, and *b*/*r*=2, for η_2/D_2=.4, .444, and .5.

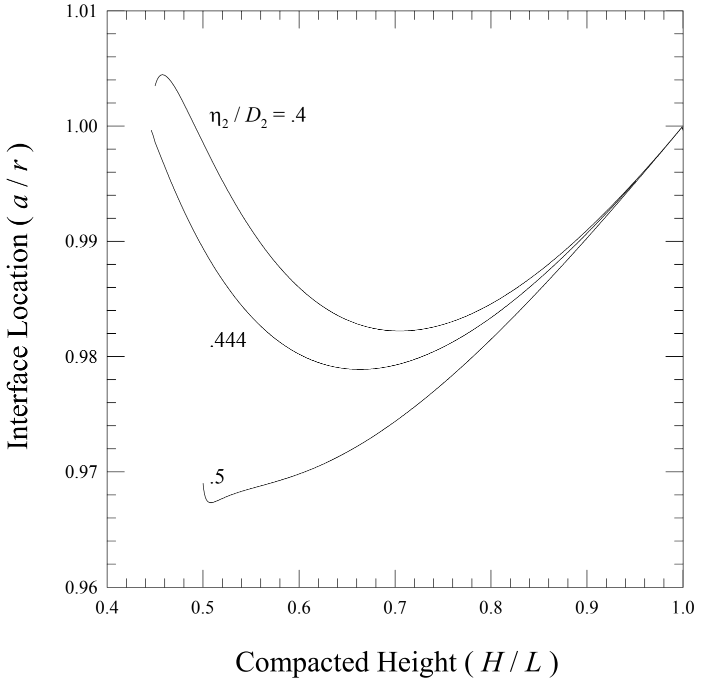

Figure 2.15: The variation of *a*/*r* with *H*/*L* when α_1=.25, α_2=.75, β_1/β_2=1, η_1/D_1=.444, and *b*/*r*=2, for η_2/D_2=.4, .444, and .5.

and eventually (at H/L=.512) the corresponding increase in compressibility of the inner powder reverses the direction of the movement of the interface.

Figure 2.15 shows the results obtained when the values of α_1(=.25) and α_2(=.75) are reversed. In this case, the interface moves radially inward as the compaction begins because α_1 is less than α_2. As the interface moves inward, the inner powder densifies more quickly, and the corresponding increase in compressibility of the inner powder eventually reverses the radial motion of the interface. As expected, the reversal occurs at increasingly later stages of the compaction as the initial density of the outer powder increases.

In Figure 2.16 we show the variation of the dimensionless load $\beta_1 F/\pi b^2$ with relative height H/L for $\alpha_1=\alpha_2=.5$, $\eta_1/D_1=\eta_2/D_2=.444$, and $b/r=2$, when $\beta_1/\beta_2=.5$, 1.0, 1.5, and 2.0. In particular, when $\beta_1/\beta_2=1.0$, the results are for the compaction of a single powder. In all cases the required compaction load increases as the compacted height decreases, as expected. The Figure 2.16 demonstrates that when the compressibility β_1 of the inner material is fixed, for example, the total load required to compress the green part to a prescribed height increases as the compressibility of the outer material decreases.

Of particular interest are the combinations of inner and outer powders that yield no movement of the interface between them. For such powders, $a(=a_1)$ is equal to $r(=r_1)$ so the balance of mass (2.1) reduces to,

$$\frac{\rho_1}{\eta_1}=\frac{\rho_2}{\eta_2}=\frac{L}{H} \quad . \tag{2.29}$$

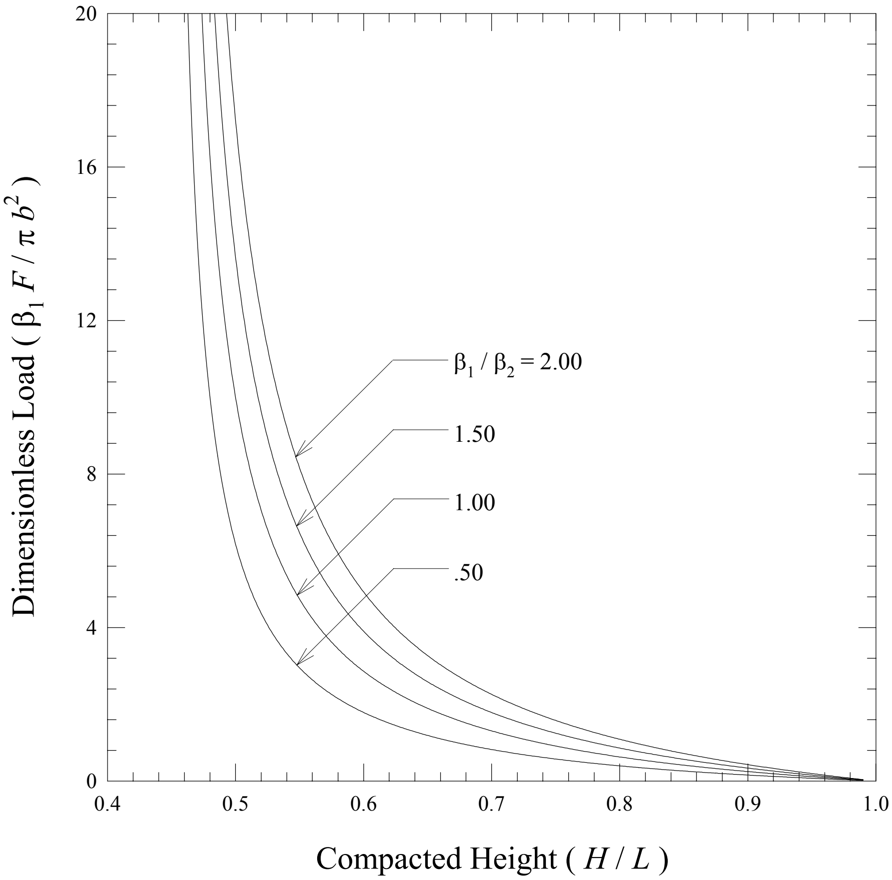

Figure 2.16: The variation of dimensionless load $\beta_1 F/\pi b^2$ with relative height H/L for $\alpha_1=\alpha_2=.5$, $\eta_1/D_1=\eta_2/D_2=.444$, and $b/r=2$, when $\beta_1/\beta_2=.5$, 1.0, 1.5, and 2.0.

According to equation (2.10), when a is equal to r, Γ_1 and Γ_2 both vanish and the constitutive relation (2.9) becomes,

$$\sigma_1 = \alpha_1 p_1 \qquad , \tag{2.30}$$

for the inner powder and

$$\sigma_2 = \alpha_2 p_2 \qquad , \tag{2.31}$$

for the outer powder. From equation (2.5) for i=1, we eliminate τ_1 and σ_1 by employing equation (2.3) for i=1 and equation (2.30). In this manner, the equation of state for the inner powder becomes,

$$\frac{\rho_1}{\eta_1} = 1 + k_1(1 + 2\alpha_1)p_1 \qquad . \tag{2.32}$$

Similarly, we eliminate τ_2 and σ_2 from equation (2.7) for i=2 by employing (2.3) for i=2 and equation (2.31). The equation of state for the outer powder is then,

$$\frac{\rho_2}{\eta_2} = 1 + k_2(1 + 2\alpha_2)p_2 \qquad . \tag{2.33}$$

Finally, we employ equations (2.29) to eliminate ρ_1/η_1 and ρ_2/η_2 from equations (2.32) and (2.33) and we employ equations (2.30), (2.31), and (2.4) to eliminate p_1 and p_2 from the intermediate result. In this manner, we find that, in order for the interface to remain at its pre-compacted radial location, the properties of the powder must satisfy the simple relation,

$$\alpha_1 = \frac{K\alpha_2}{1+2\alpha_2(1-K)} \quad , \tag{2.34}$$

where $K \equiv k_1/k_2$. According to equation (2.6), k_i is given by

$$k_i = \beta_i \left[1 - \frac{(L/H)-1}{(D_i/\eta_i)-1} \right] \quad , \qquad \text{(i=1 or 2)} \tag{2.35}$$

in which equation (2.29) has been used to eliminate ρ_i and η_i.

In general, the relationship between the powder fluidities described in equation (2.34) depends on β_1/β_2, η_1/D_1, η_2/D_2, and H/L. For the special case where η_1/D_1 and η_2/D_2 are equal, K reduces to the ratio β_1/β_2 and the relationship between α_1 and α_2 depends solely on the ratio of the compressibilities β_1/β_2.

In Figure 2.17, equation (2.34) is employed to generate the locus of points in the α_1-α_2 plane for which the interface moves neither radially inward nor outward (i.e. $a=r$), when $\eta_1/D_1=\eta_2/D_2$ for β_1/β_2=.5, .75, 1.0, 1.33, and 2.0. When, for example, $\beta_1/\beta_2=1.0$, the powders are of equal compressibilities, the interface remains fixed only if they are also of equal fluidities, and equation (2.34) reduces to the requirement that $\alpha_1=\alpha_2$. In principle, as the inner powder becomes more compressible relative to the outer powder, its fluidity relative to the fluidity of the outer powder must increase for the interface to remain at its initial position. For increasing β_1/β_2, this phenomenon is described in

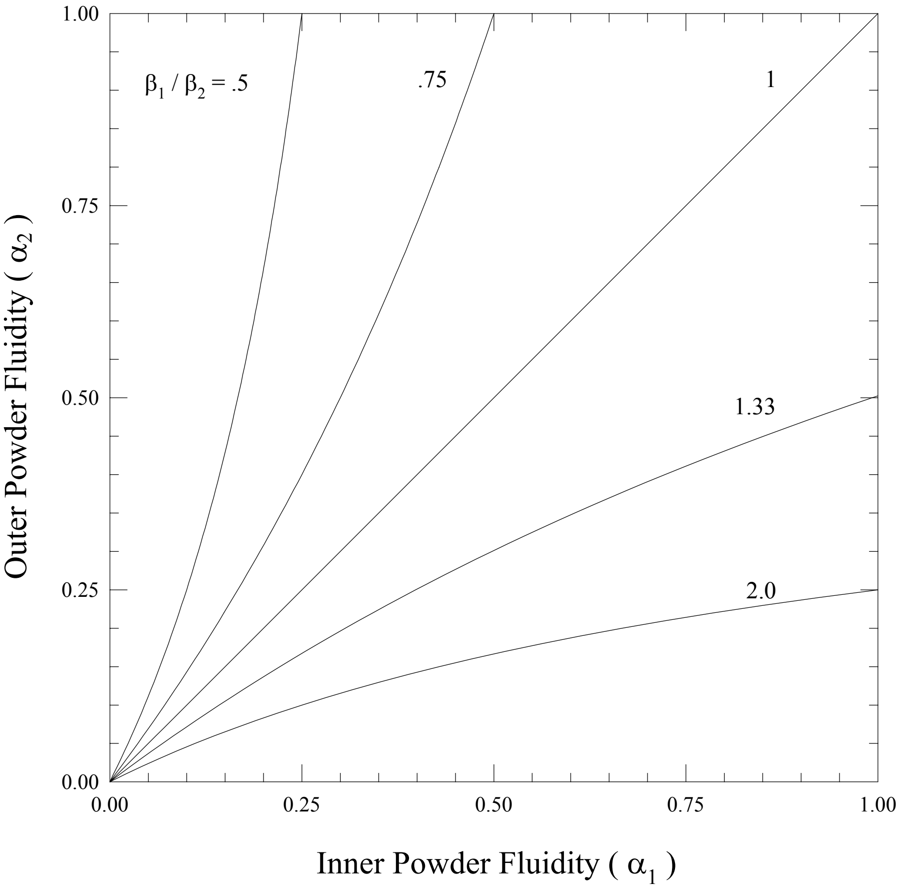

Figure 2.17: The locus of points in the α_1-α_2 plane for which *a* equals *r* when, $\eta_1/D_1=\eta_2/D_2$ for β_1/β_2=.5, .75, 1.0, 1.33, and 2.0.

Figure 2.17 by a shift of the curves away from the α_2-axis and toward the α_1-axis. Conversely, as the inner powder becomes less compressible relative to the outer powder, the shift is toward the α_2-axis and away from the α_1-axis.

In Figure 2.18, equation (2.34) is used to generate the locus of points in the α_1-α_2 plane for which a equals r, when η_1/D_1=.435, β_1/β_2=1, and H/L=.5, for η_2/D_2=.4, .435, and .476. When η_2/D_2=.435, the powders are of equal relative apparent densities; under these circumstances, equation (2.34) indicates that the interface remains fixed only if α_1 equals α_2. When η_2/D_2=.4, then the outer powder is further from its maximum density than is the inner powder. Under these circumstances, the outer powder is more compressible than the inner powder, and the interface will not move only if the fluidity of the outer powder is greater than the fluidity of the inner powder. Conversely, when η_2/D_2=.476, then the outer powder is closer to its maximum density than is the inner powder, so its fluidity must be less than the fluidity of the inner powder. These phenomena are described in Figure 2.18 by a shift of the curves toward the α_2-axis when η_2/D_2=.4, and a shift toward the α_1-axis when η_2/D_2=.476. Figure 2.19 shows a similar plot in which the relative apparent density of the outer powder is fixed and the relative apparent density for the outer powder is varied. As expected, if mirrored about the line corresponding to α_1=α_2, then Figures 2.18 and 2.19 are identical.

Figures 2.20 and 2.21 demonstrate the effect of H/L on the relationship between α_1 and α_2 for unequal values of the relative apparent densities η_1/D_1 and η_2/D_2. In Figure 2.20, we show the locus of points in the α_1-α_2 plane for which a equals r, when

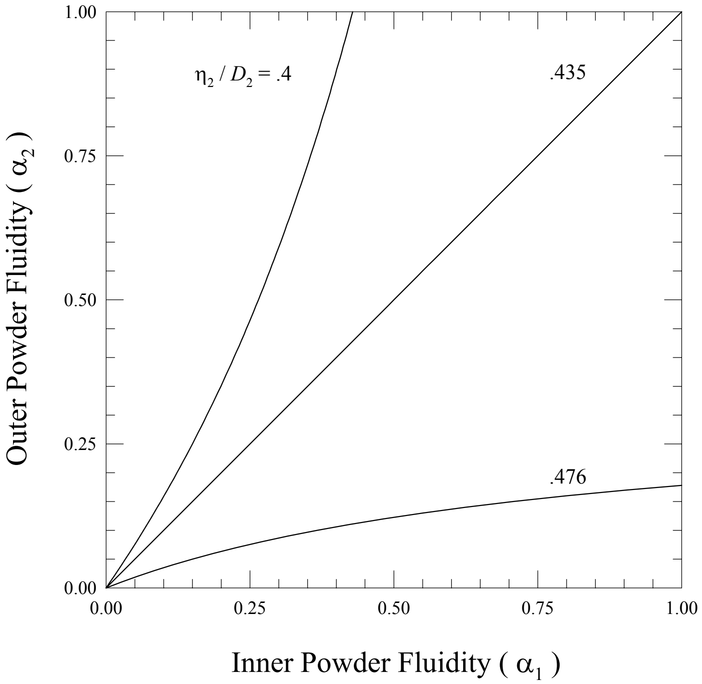

Figure 2.18: The locus of points in the α_1-α_2 plane for which a equals r, when η_1/D_1=.435, β_1/β_2=1, and H/L=.5, for η_2/D_2=.476, .435, and .4.

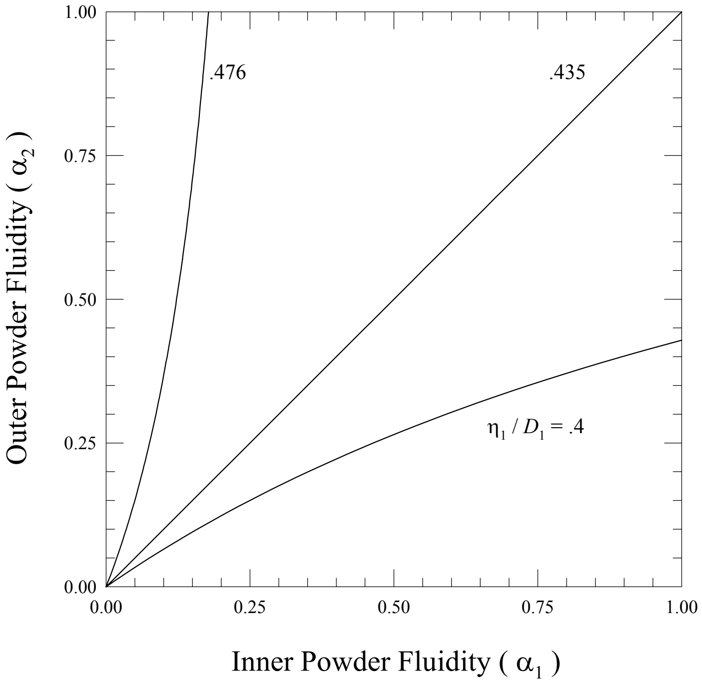

Figure 2.19: The locus of points in the α_1-α_2 plane for which a equals r, when η_2/D_2=.435, β_1/β_2=1, and H/L=.5, for η_1/D_1=.476, .435, and .4.

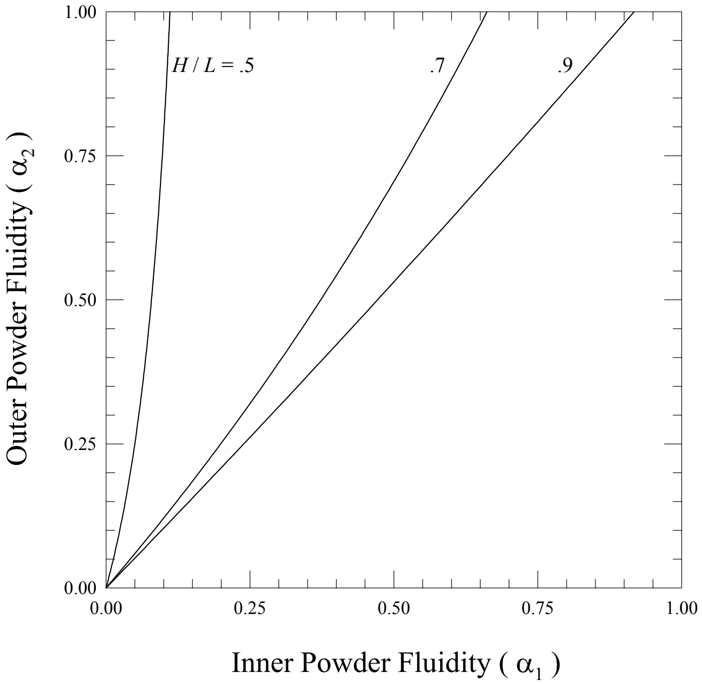

Figure 2.20: The locus of points in the α_1-α_2 plane for which *a* equals *r*, when η_1/D_1=.476, η_2/D_2=.4, and β_1/β_2=1, for *H*/*L*=.9, .7, and .5.

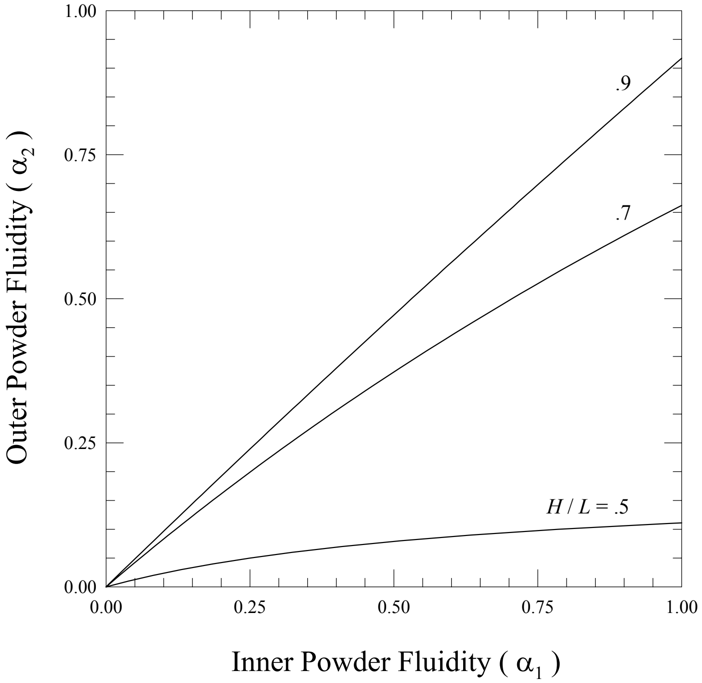

Figure 2.21: The locus of points in the α_1-α_2 plane for which *a* equals *r*, when η_1/D_1=.4, η_2/D_2=.476, and β_1/β_2=1, for *H*/*L*=.9, .7, and .5.

η_1/D_1=.476, η_2/D_2=.4, and β_1/β_2=1 for H/L=.9, .7, and .5. The inequality in relative apparent densities makes the inner powder less compressible and more apt to expand radially than the outer powder. Consequently, for all H/L, the fluidity of the inner powder must be less than that of the outer powder. As H/L decreases while the interface maintains its original location, the inner powder is always closer to its maximum density than the outer powder. Its compressibility therefore decreases more rapidly than that of the outer powder, and the fluidity of the outer powder must be increasingly greater than the fluidity of the inner powder to compensate for the changes in compressibilities. In Figure 2.21, we show a similar plot in which the values of η_1/D_1 (=.4) and η_2/D_2 (=.476) have been reversed. As expected, if mirrored about the line representing α_1=α_2, Figures 2.20 and 2.21 are identical.

In Figure 2.22, we show the variation of a/r with H/L when η_1/D_1=.476, η_2/D_2=.4, β_1/β_2=1, and b/r=2, for pairs of fluidities α_1=.05 and α_2=.25, α_1=.0633 and α_2=.35, and α_1=.0789 and α_2=.5. The particular combinations of α_1 and α_2 used to generate this figure are obtained from Figure 2.20 for the case where H/L=.5. For the three cases shown here, α_2 is much greater than α_1 so that the interface has an initial tendency to contract inward. As H/L decreases, however, the inner powder approaches its maximum density faster than the outer powder approaches its maximum. Consequently, the movement of the interface eventually reverses direction. Finally, as expected from Figure 2.20, the interface returns to its initial position when H/L=.5. In Figure 2.23, we show corresponding variations of a/r with H/L in which the values of η_1/D_1 (=.4) and

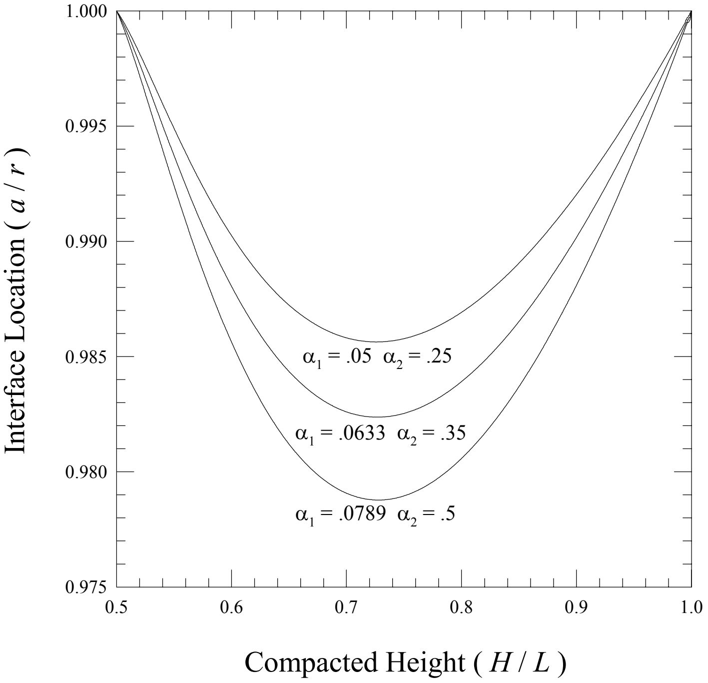

Figure 2.22: The variation of *a*/*r* with *H*/*L* when η_1/D_1=.476, η_2/D_2=.4, β_1/β_2=1, and *b*/*r*=2, for α_1=.05 and α_2=.25, α_1=.0633 and α_2=.35, and α_1=.0789 and α_2=.5.

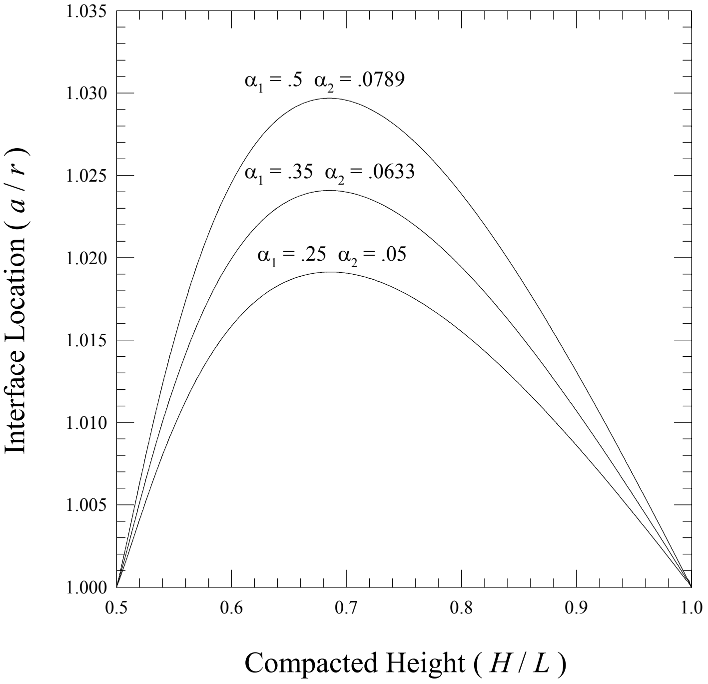

Figure 2.23: The variation of *a*/*r* with *H*/*L* when η_1/D_1=.4, η_2/D_2=.476, β_1/β_2=1, and *b*/*r*=2, for α_1=.5 and α_2=.0789, α_1=.35 and α_2=.0633, and α_1=.25 and α_2=.05.

η_2/D_2 (=.476) have been reversed from those used in Figure 2.22. The trends observed here are therefore also reversed.

The area above and below the curves in the locus plots shown in Figures 2.17 through 2.21 corresponds, respectively, to pairs of powders for which the interface moves radially inward ($a<r$) and outward ($a>r$). Because the final interface location plays an important role in the green state density distribution of the two-powder compact, it is useful to determine the exact combination of powders that yield a desired post-compaction interface location. To determine the conditions that yield a prescribed post-compaction interface location, we take a to be a known parameter, treat α_2 as an unknown, and modify the solution procedure described in section 2.4 accordingly.

In Figure 2.24, we show the locus of points in the α_1-α_2 plane for a/r=.98, .99, 1, 1.01, 1.02, 1.03, and 1.04 when $\beta_1/\beta_2=1$, $\eta_1/D_1=\eta_2/D_2$, H/L=.5, and b/r=2. Because the powders are of equal compressibilities and relative apparent densities, the interface will not move (i.e. a/r=1.0) only if $\alpha_1=\alpha_2$. For values of α_1 less than α_2, the interface moves radially inward. This inward movement increases as the disparity between the two fluidities increases. For α_1 greater than α_2, the interface moves radially outward, and again the movement increases as the disparity between α_1 and α_2 increases.

In Figure 2.25, we show the locus of points in the α_1-α_2 plane for a/r=.99, 1, 1.01, 1.02, 1.03, 1.04, and 1.05 when β_1/β_2=.5, $\eta_1/D_1=\eta_2/D_2$, H/L=.5, and b/r=2. With β_1/β_2=.5, the interface now has an inherent tendency to expand radially outward. To cancel this tendency and prevent the interface from moving at all, α_2 must be greater than

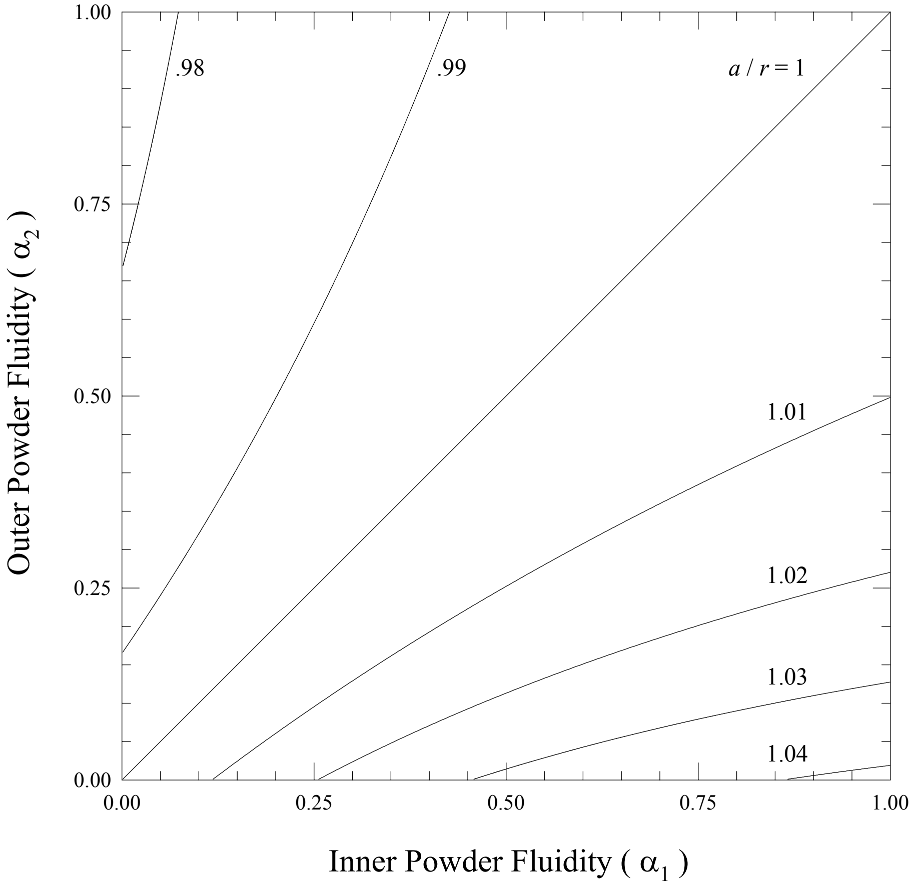

Figure 2.24: The locus of points in the α_1-α_2 plane when $\beta_1/\beta_2=1$, $\eta_1/D_1=\eta_2/D_2$, $H/L=.5$, and $b/r=2$, for $a/r=.98$, .99, 1.00, 1.01, 1.02, 1.03, and 1.04.

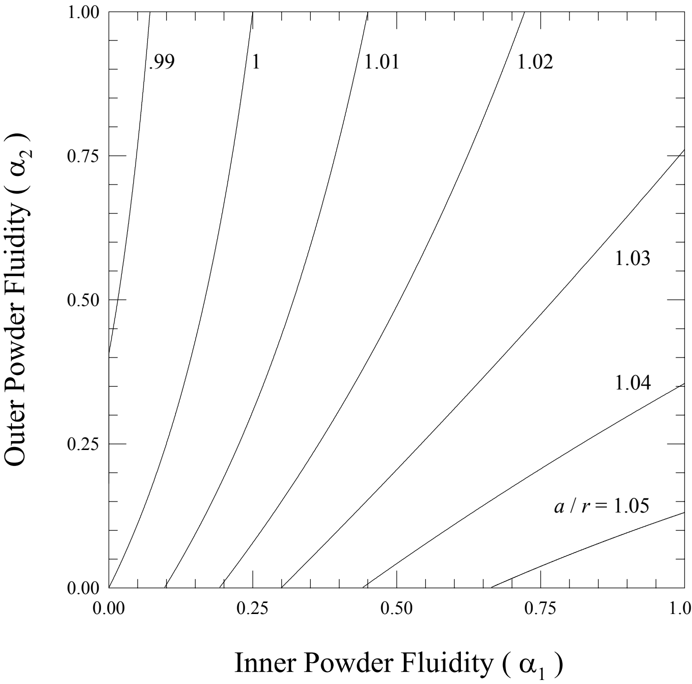

Figure 2.25: The locus of points in the α_1-α_2 plane when β_1/β_2=.5, $\eta_1/D_1=\eta_2/D_2$, H/L=.5, and b/r=2, for a/r=.99, 1.00, 1.01, 1.02, 1.03, 1.04, and 1.05.

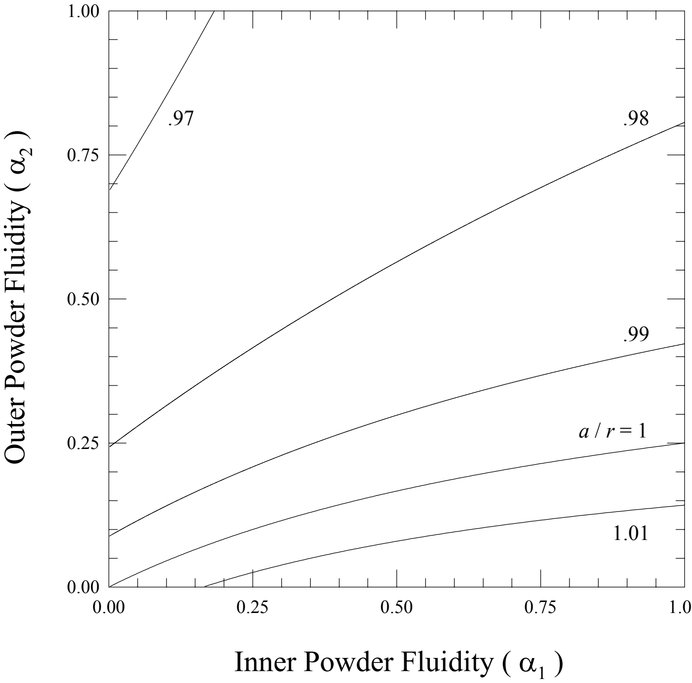

Figure 2.26: The locus of points in the α_1-α_2 plane when β_1/β_2=2, $\eta_1/D_1=\eta_2/D_2$, H/L=.5, and b/r=2, for a/r=.97, .98, .99, 1.00, and 1.01.

α_1. This required disparity in the fluidities results in a shift of the curve for a/r=1.0 away from its position in Figure 2.24 (when β_1/β_2=1) toward the α_2-axis. Likewise, the curves in Figure 2.25 corresponding to any other prescribed value of a/r undergo qualitatively similar shifts.

In Figure 2.26, we show the locus of points in the α_1-α_2 plane for a/r=.97, .98, .99, 1, and 1.01 when β_1/β_2=2, η_1/D_1=η_2/D_2, H/L=.5, and b/r=2. With β_1/β_2=2, the interface has a tendency to move radially inward. This tendency to move inward causes the curves for prescribed values of a/r to shift away from their positions in Figure 2.24 (when β_1/β_2=1) toward the α_1-axis.

Finally, we examine the effects of disparate relative apparent densities on the fixed a/r loci. To this end, in Figure 2.27 we show the locus of points in the α_1-α_2 plane for a/r=1, 1.01, 1.02, 1.03, 1.04, 1.05, and 1.06 when β_1/β_2=1, η_1/D_1=.476, η_2/D_2=.4, H/L=.5, and b/r=2. Since η_1/D_1 is greater than η_2/D_2 the inner powder acts as if it is less compressible than the outer powder. This situation is similar to two powders with equal relative apparent densities but with the compressibility β_1 of the inner powder less than the compressibility β_2 of the outer powder. Consequently, the curves in Figure 2.27 shift in a manner that is qualitatively similar to those described in Figure 2.25. In Figure 2.28 we show the locus of points in the α_1-α_2 plane for a/r=.95, .96, .97, .98, .99, and 1 when β_1/β_2=1, η_1/D_1=.4, η_2/D_2=.476, H/L=.5, and b/r=2. Here η_1/D_1 is less than η_2/D_2, so the inner powder behaves as if it is more compressible than the outer powder. The shifts in

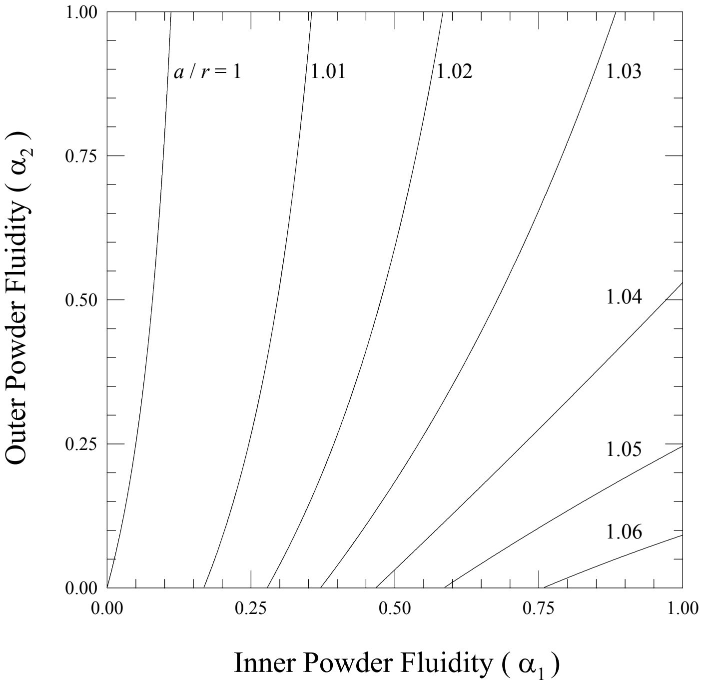

Figure 2.27: The locus of points in the α_1-α_2 plane when $\beta_1/\beta_2=1$, $\eta_1/D_1=.476$, $\eta_2/D_2=.4$, $H/L=.5$, and $b/r=2$, for $a/r=1.00$, 1.01, 1.02, 1.03, 1.04, 1.05, and 1.06.

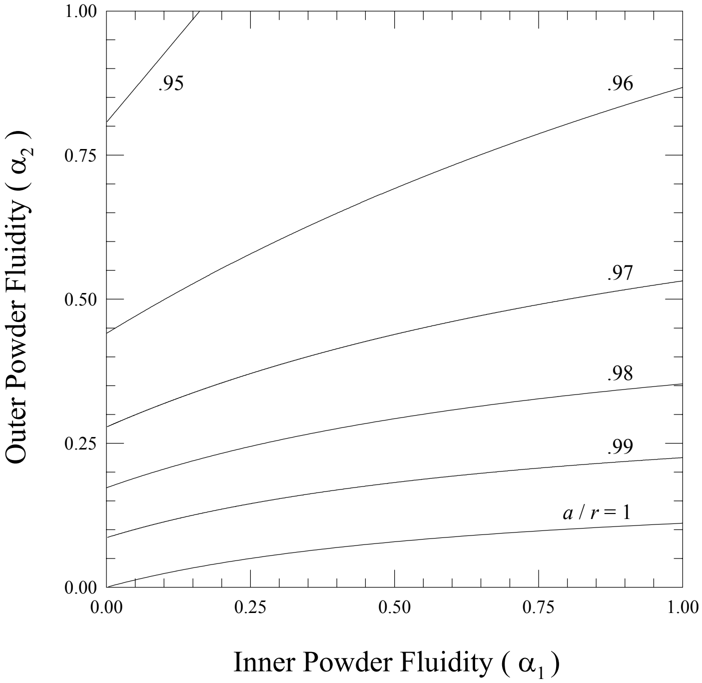

Figure 2.28: The locus of points in the α_1-α_2 plane when $\beta_1/\beta_2=1$, $\eta_1/D_1=.4$, $\eta_2/D_2=.476$, $H/L=.5$, and $b/r=2$, for $a/r=.95$, .96, .97, .98, .99, and 1.00.

these curves relative to those in Figure 2.24 are therefore similar to those shown in Figure 2.26.

2.6 Results and Discussion: Twenty-powder Compacts (n=20)

The model developed in sections 2.1 through 2.3 is for a cylindrical die with n concentric, annular regions of powder. Each powder has its own distinct properties. In section 2.5, we set n=2 in order to study the compaction behavior of two-powder parts. Most importantly, the results demonstrate the effects of mismatches in the compressibilities, fluidities, and relative apparent densities of the powder. At this point, we increase n so that a single powder with continuously varying powder properties can be approximated.

To determine an appropriate value of n, we consider a test case in which the compacted height H/L=.5; all β_i are equal to one another; η_i/D_i is everywhere equal to (1/2.25)=.444; but due to uneven powder blend the fluidity α_i increases linearly from .25 at the centerline of the die to .75 at the die wall. This continuous variation of α_i can be approximated with increasing accuracy as n increases. In Figure 2.29 we show stepwise approximations of the α_i-variation for n=2, 4, 10, and 20. In Figures 2.30 and 2.31 we show the corresponding variations of green density ρ_i/D_i and pressure $\beta_1 p_i$ with final radial position a_i/b. In each, the solid curves are comprised of straight lines connecting consecutive data points. For n=2, the variations of pressure and density must be linear because only two points are plotted. As n increases, the variations of pressure and

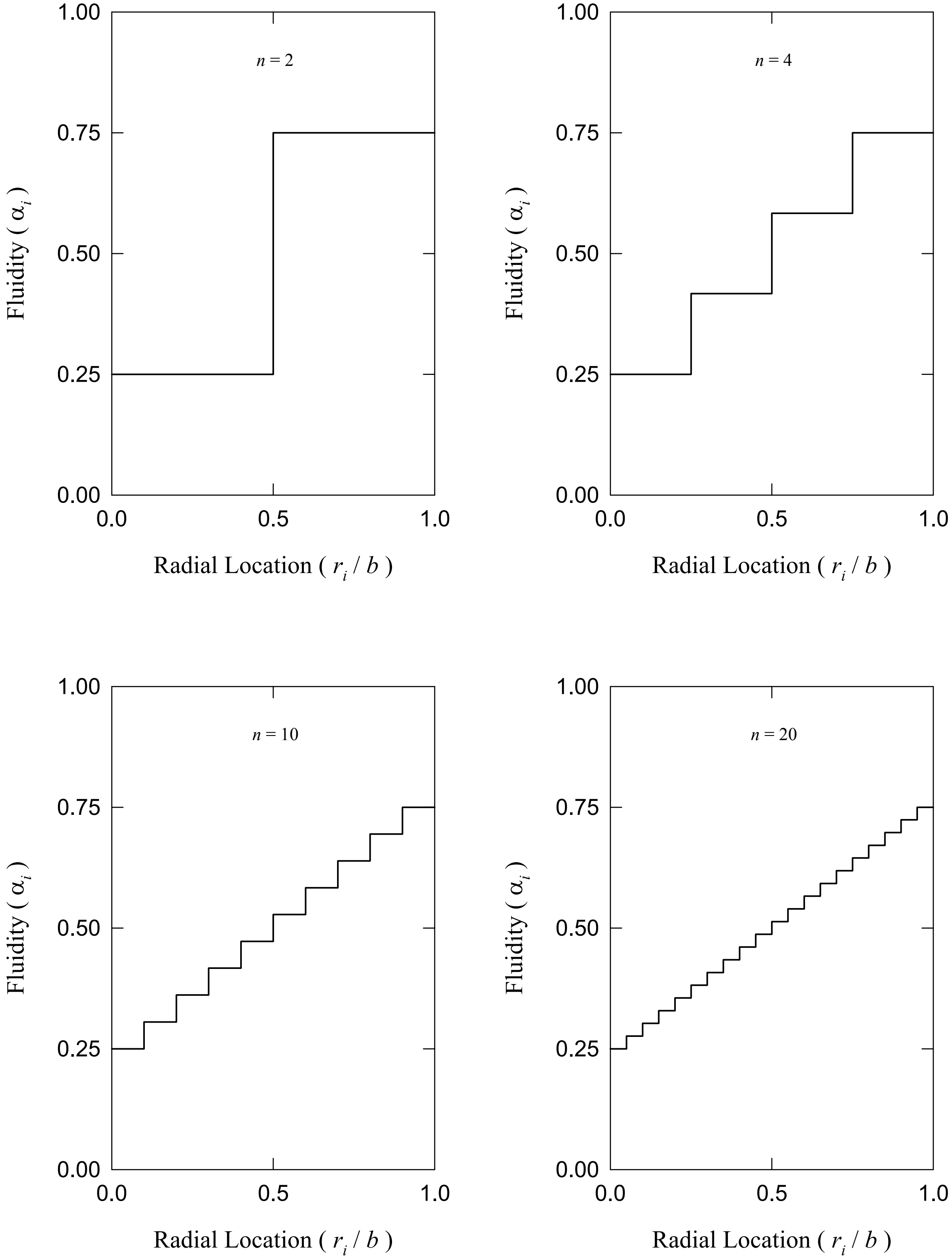

Figure 2.29: The variations of α_i for *n*=2, 4, 10, and 20 used in Figures 2.30 and 2.31.

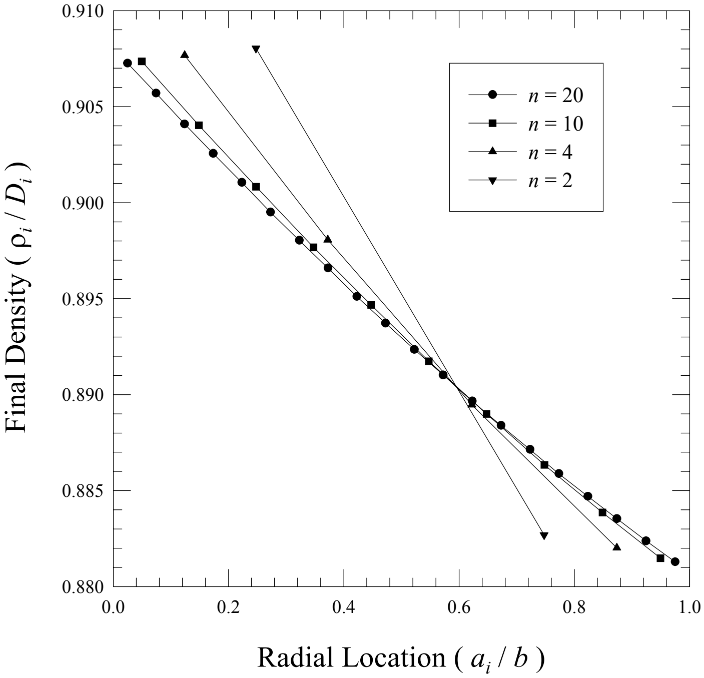

Figure 2.30: The variations of green density ρ_i/D_i with final radial position a_i/b when α_i varies linearly from .25 at the centerline to .75 at the die wall, η_i/D_i=.444, $\beta_1=\beta_2=\ldots=\beta_n$, and H/L=.5, for n=2, 4, 10, and 20.

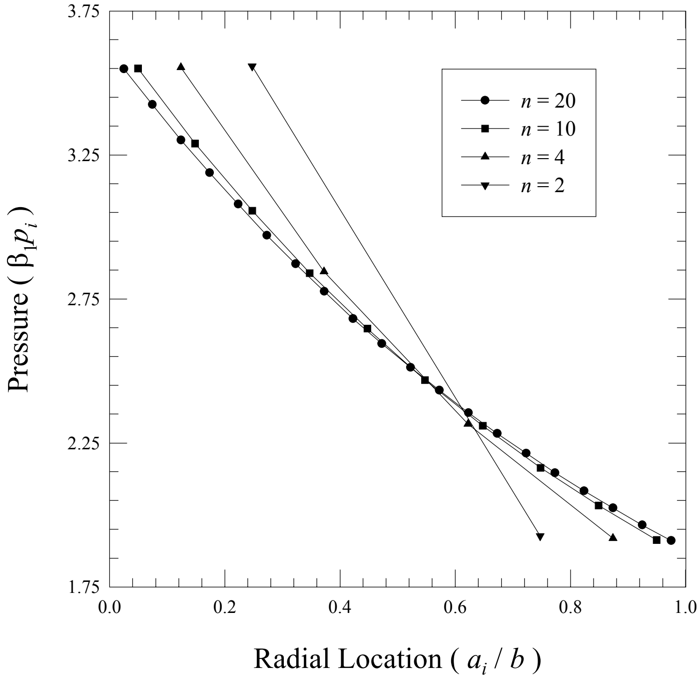

Figure 2.31: The variations of pressure $\beta_1 p_i$ with final radial position a_i/b when α_i varies linearly from .25 at the centerline to .75 at the die wall, η_i/D_i=.444, $\beta_1=\beta_2=\ldots=\beta_n$, and H/L=.5, for n=2, 4, 10, and 20.

density with radial location become nonlinear. In addition, as n increases, both the pressure and density converge to variations that do not change appreciably beyond those corresponding to n=10. We conclude that 20 concentric powders more than adequately approximates a single powder during compaction. For this reason, in all that follows, we choose n=20.

As a test, we consider the case in which all β_i are equal to one another; α_i=.5 for i=1 to n; but due to uneven fill η_i/D_i increases linearly from (1/2.5)=.40 at the centerline of the die, to (1/2.25)=.444 at the die wall. In Figure 2.32, we show as a solid line through distinct data points the resulting variation of green densities ρ_i/D_i with final radial positions a_i/b when the compacted height is H/L=.5. Not surprisingly, because the initial fill density increases with radial distance from the centerline, so too does the final green density distribution. However, in order to gain insight into the effects of radial movements on final green density distributions, we have superposed as a dashed line the values of ρ_i/D_i that would be predicted if the radial movements of the interfaces were neglected. According to equation (2.6), the local compressibility of the powder decreases with increasing density. In this case, therefore, the more dense regions far from the centerline are less compressible and experience net expansions in the radial direction, while the less dense regions near the centerline are more compressible and experience net contractions in the radial directions. Consequently, the densities far from the centerline are smaller than, and the densities near the centerline are greater than those predicted without accounting for radial movements.

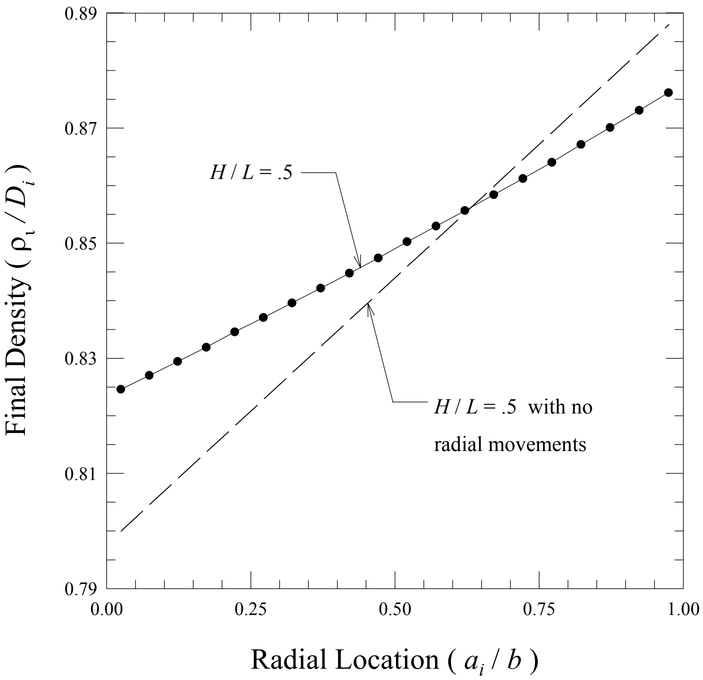

Figure 2.32: The variation of ρ_i/D_i with a_i/b when η_i/D_i varies linearly from .4 at the centerline to .444 at the die wall, α_i=.5, $\beta_1=\beta_2=\ldots=\beta_n$, and n=20, for H/L=.5. Shown as a dashed curve is the variation of ρ_i/D_i neglecting radial movements.

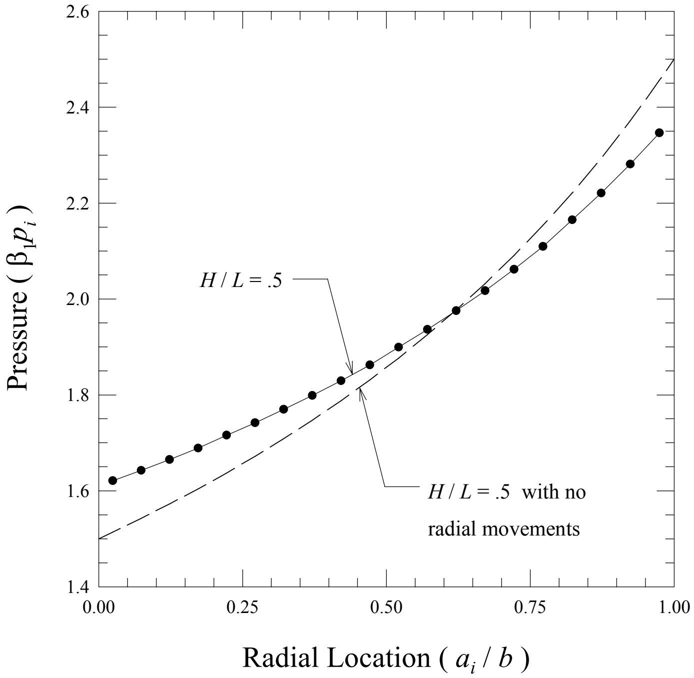

Figure 2.33: The variation of $\beta_1 p_i$ with a_i/b corresponding to the two cases shown in Figure 2.32.

In Figure 2.33, we show the corresponding variations of pressure $\beta_1 p_i$. In this case, due to nonuniform fill the local compressibility of the powder decreases with distance from the centerline. In order to compensate for this effect, the pressure must vary in the opposite way. However, because the density of the material near the centerline is greater than that predicted without accounting for radial movements, it is less compressible and therefore requires a higher pressure than that predicted by the dashed curve. Similarly, the density far from the centerline is smaller than that predicted without radial movements, so that the corresponding pressure is lower than that predicted by the dashed curve.

In Figure 2.34 we show the results of three inverse problems. In each problem, we specify the initial pre-compaction variations of α_i and β_i, and then compute the initial density variation required to yield a perfectly uniform post-compaction green density distribution. In the first inverse problem, all β_i are equal to one another, but due to uneven powder blend α_i increases linearly from .25 at the centerline to .75 at the die wall. The distribution of initial density η_i/D_i that yields a perfectly uniform green density $\rho_i/D_i=(2/2.25)=.888$ at $H/L=.5$ is shown as a solid curve through solid circles. Where the values of α_i are relatively low, the material tends to contract radially and densify more readily. Where the values of α_i are relatively high, the material tends to expand radially and densify less readily. Such effects would cause inhomogeneities in the final density distribution if the initial density distribution was uniform. To compensate for these effects, the initial densities must be lower where the radial contractions occur, and must

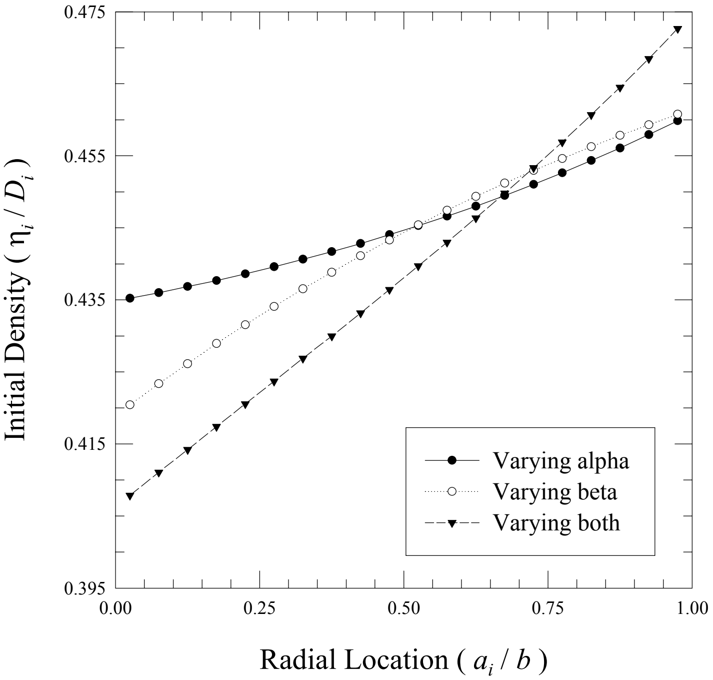

Figure 2.34: The variations of η_i/D_i with a_i/b required to yield $\rho_i/D_i \equiv .888$ at $H/L=.5$ when: a) α_i varies linearly from .25 at the centerline to .75 at the die wall and $\beta_1=\beta_2=\ldots=\beta_n$ (solid circles); b) $\alpha_i=.5$ and β_i/β_1 varies linearly from 1 at the centerline to .5 at the die wall (open circles); c) α_i varies from .25 at the centerline to .75 at the die wall and β_i/β_1 varies linearly from 1 at the centerline to .5 at the die wall (solid triangles).

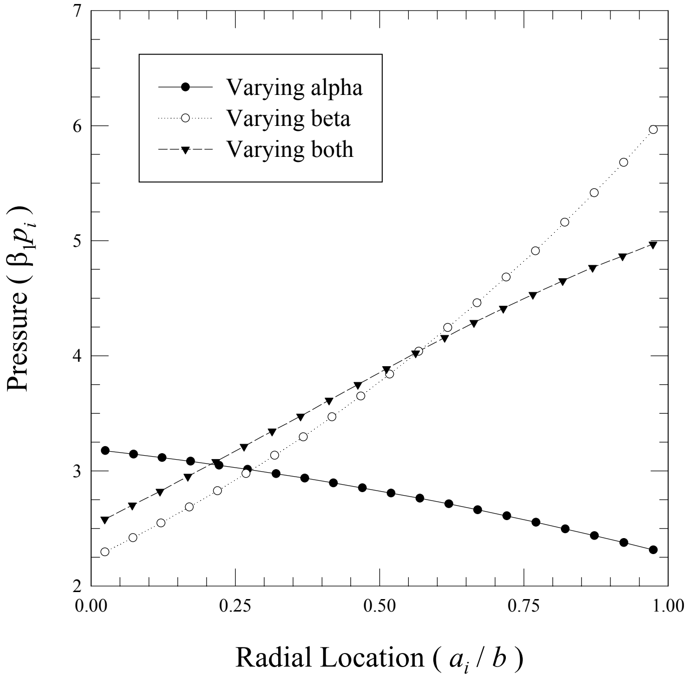

Figure 2.35: The variation of $\beta_1 p_i$ with a_i/b for n=20 corresponding to the three cases in Figure 2.34.

be higher where the radial expansions occur. Consequently, the initial density must increase with increasing α_i and (in this case) with increasing distance from the centerline.

In the second inverse problem shown in Figure 2.34, we consider the case in which β_i/β_1 decreases linearly from 1 at the centerline to .5 at the die wall and α_i=.5 for all i=1 to n. The distribution of initial density η_i/D_i that yields a perfectly uniform green density ρ_i/D_i=(2/2.25)=.888 at H/L=.5 is shown as a solid curve through open circles. Where the values of β_i are relatively high, the material tends to contract radially and densify more readily. Where the values of β_i are relatively low, the material tends to expand radially and densify less readily. To ensure uniform final densities, the initial densities must therefore be lower where β_i is higher, and higher where β_i is lower. Consequently, the initial density increases with decreasing β_i and (in this case) with increasing distance from the centerline.

In the last inverse problem shown in Figure 2.34, we combine the effects of the first two cases and consider a third case in which β_i/β_1 decreases linearly from 1 at the centerline to .5 at the die wall and α_i increases linearly from .25 at the centerline to .75 at the die wall. The distribution of initial density η_i/D_i that yields a perfectly uniform green density ρ_i/D_i=(2/2.25)=.888 at H/L=.5 is shown as a solid curve through solid triangles. The effects of radially increasing α_i and radially decreasing β_i on the required initial density variation are additive, so that there is a more pronounced variation of the required initial density when the fluidity and compressibility vary simultaneously.

Interestingly, although the final densities for the three inverse cases are uniform, the required pressure distributions are not. In Figure 2.35, we show the corresponding variation of pressure $\beta_1 p_i$ for the three cases described in Figure 2.34. Where α_i are relatively low, increased axial pressures are required to generate the radial pressures needed for radial equilibrium. Consequently, in the first case, the pressure must be higher near the centerline (where α_i are low) than it is near the outer edge (where α_i are high). Where β_i are relatively high, decreased pressures are required for compression of the powder. Consequently, in the second case, the pressure must be lower near the centerline (where β_i are high) than it is near the outer edge (where β_i are low). Whereas the effects of radially increasing α_i and radially decreasing β_i on the required initial density are additive, their effects on the pressure variation are competitive. As a result, the final pressure distribution is a compromise between the first two pressure distributions shown in Figure 2.35.

CHAPTER 3

Compaction In Frictionless, Cylindrical Dies: Single Powders With Radially Varying Properties

3.1 Balance of Mass and Momentum

We are concerned here with the single punch compaction of a powder in a frictionless cylindrical die of radius *b*. In the absence of friction, no axial variations of density and pressure are induced during compaction. Because of symmetry, there are no variations with angle of rotation about the centerline of the compact. It is therefore only necessary to introduce a radial coordinate *r* that measures distance from the centerline. Before the powder is compacted, the cylindrical die is filled to a height *L* with a powder of apparent density $\eta(r)$. Radial variation of apparent density is due to uneven fill. Uneven fill also causes radial variations $\alpha(r)$ and $\beta(r)$ in the powder fluidity and compressibility, respectively. The green compact has a height *H* and final density $\rho(r)$. Because of fill nonuniformities, powder particles move axially and radially during compaction. The radial location of a powder particle initially located at *r* before compaction is given by $a(r)$ after compaction. The pre- and post-compaction geometries are shown in Figures 3.1 and 3.2.

If we consider an annulus of height *L* bounded radially by *r* and $r+dr$ before compaction and a corresponding annulus of height *H* bounded by *a* and $a+da$ after

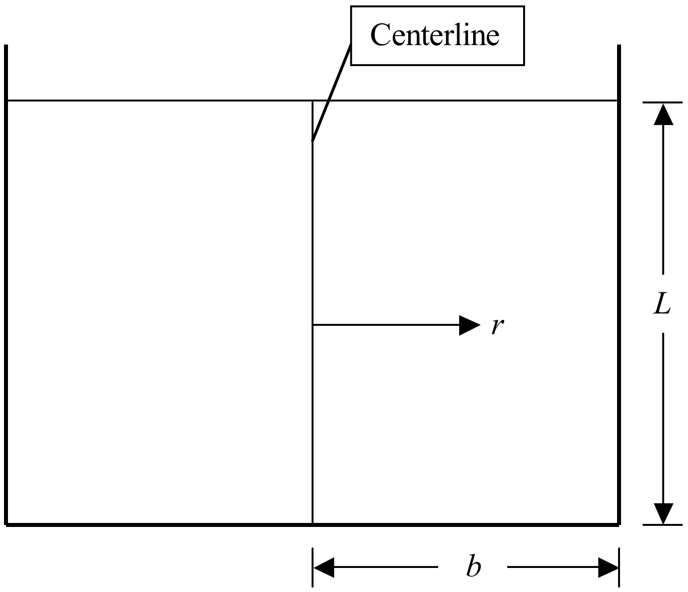

Figure 3.1: Pre-compaction geometry.

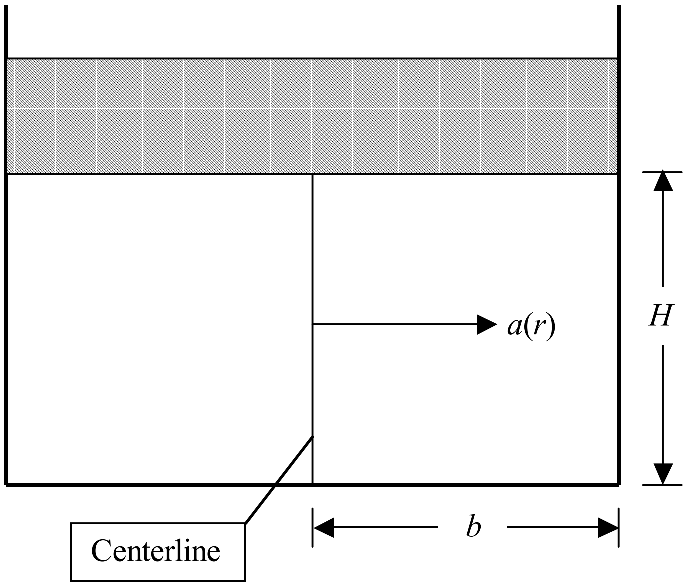

Figure 3.2: Post-compaction geometry.

compaction, the balance of mass requires that the mass contained in the two annuli be equal:

$$\eta\left[(r+dr)^2 - r^2\right]\pi L = \rho\left[(a+da)^2 - a^2\right]\pi H \quad . \tag{3.1}$$

Neglecting terms of order da^2 and dr^2 gives:

$$\frac{a}{r}\frac{da}{dr} = \frac{\eta}{\rho}\frac{L}{H} \quad . \tag{3.2}$$

The quantities r, $r+dr$, a, $a+da$, ρ, and η in equation (3.1) are the analogs to a_{i-1}, a_i, r_{i-1}, r_i, ρ_i, and η_i in equation (2.1) of the n-powder model. Equation (3.2) could also be obtained by taking the appropriate limit of equation (2.1). Although equation (3.2) is only a first order equation, the variation $a(r)$ must satisfy two boundary conditions. Powder particles that initially lie along the centerline remain there throughout compaction. Therefore,

$$a(r=0) = 0 \quad . \tag{3.3}$$

Likewise, powder particles at the outer die wall remain there throughout compaction. Therefore,

$$a(r=b) = b \quad . \tag{3.4}$$

To ensure axial momentum balance in the compact, the compaction load F must be balanced by the axial pressures $p(r)$ developed in the powder. The axial pressure $p(r)$ must therefore be related to,

$$F = 2\pi \int_0^b p(r) r dr \quad . \tag{3.5}$$

Equation (3.5) could also be obtained by taking the appropriate limit of equation (2.2) of the *n*-powder model.

The axial pressure developed in the powder during compaction induces a corresponding radial pressure σ and tangential pressure τ. To ensure radial momentum balance, these pressures must be equal and constant. Consequently,

$$\sigma = \tau = \text{constant} \quad , \tag{3.6}$$

which are the continuous limits of equations (2.3) and (2.4) of the *n*-powder model.

For given values of compaction load F and pre-compaction height L, as well as for prescribed non-uniform apparent density $\eta(r)$, the unknown functions of r are the green density $\rho(r)$, the axial pressure $p(r)$, and the final axial locations $a(r)$. The unknown constants are the final height H, the radial pressure σ, and the tangential pressure τ. Equations (3.2), (3.3), (3.4), (3.5), and (3.6) are not sufficient to determine these unknowns.

3.2 Equations of State and Constitutive Relations

To complete the system, we need additional relations between the pressures p(r), σ, and τ, and the density ρ(r). The equation of state is a constitutive relation that associates the post-compaction density ρ(r) to the total pressure (p+σ+τ). By exchanging the quantities ρ_i, η_i, D_i, β_i, p_i, σ_i, and τ_i in equation of state (2.7) for their continuous analogs, ρ, η, D, β, p, σ, and τ, respectively, we obtain,

$$\frac{\rho}{\eta} = \frac{(D-\eta)+\beta D(p+\sigma+\tau)}{(D-\eta)+\beta\eta(p+\sigma+\tau)} \quad . \tag{3.7}$$

Here, D is the maximum theoretical density and β is the compressibility of the powder. Due to uneven fill, the compressibility β(r) can vary with r.

In order to derive a constitutive relation for the induced radial pressure σ, we first introduce a general measure Δ of radial deformation, defined by,

$$\Delta \equiv a\frac{da}{dr} \quad . \tag{3.8}$$

Then by employing the balance of mass (3.2) to eliminate the density ρ from the equation of state (3.7), we find that,

$$\Delta = \frac{L}{H} r \left[\frac{(D-\eta)+\beta D(p+\sigma+\tau)}{(D-\eta)+\beta\eta(p+\sigma+\tau)} \right] \quad . \tag{3.9}$$

In order to write down a plausible relation between the induced radial pressure σ, and the deformation Δ, we consider two extreme cases. In the first extreme, an annulus of powder is confined between two rigid, frictionless, cylindrical walls during compaction. In this case, there is no radial movement of the powder (i.e. $a=r$), so that $\Delta=r$. Under these circumstances σ is equal to αp, where α is the fluidity of the powder.

In the second extreme, we consider a case in which the expansion of the annulus of powder is uninhibited by the radial pressure σ. In this case, both σ and τ vanish, and the corresponding value Δ_0 of Δ is given by equation (3.9) with $\sigma=\tau=0$.

In general, the radial movements of the powder will lie between these two extremes. Consequently, we simply interpolate linearly between $\sigma=0$ when $\Delta=\Delta_0$ and $\sigma=\alpha p$ when $\Delta=r$, to obtain a more general relation between σ and Δ. In this manner, we obtain,

$$\sigma = \alpha p\left[1-\Gamma\right] \qquad , \tag{3.10}$$

in which,

$$\Gamma = \frac{r-\Delta}{r-\Delta_0} \qquad . \tag{3.11}$$

Alternatively, equation (3.10) could be obtained by taking the appropriate limit of equation (2.9).

In this model, powder fill nonuniformities are described by the radial variations of apparent density $\eta(r)$, powder compressibility $\beta(r)$, and powder fluidity $\alpha(r)$. In a typical forward problem formulation, $\eta(r)$, $\alpha(r)$, $\beta(r)$, fill height L, final height H, and maximum theoretical density D are all prescribed. Mass balance (3.2) with conditions (3.3) and (3.4), axial force balance (3.5), radial force balance (3.6), equation of state (3.7), and constitutive relation (3.10) are five equations for the following seven unknowns: the final interface location $a(r)$; the final density $\rho(r)$; the axial pressure $p(r)$; the radial pressure σ; the tangential pressure τ; the axial force F; and a constant that results from the integration of the balance of mass.

3.3 Forward and Inverse Problems: Solution Procedure

As in the discrete case, described in the last chapter, the system of equations presented here is nonlinear and it is not possible to find explicit algebraic expressions for the unknowns. However it is possible to eliminate some of the unknowns in order to reduce the number of equations that must be solved simultaneously. To this end, we employ equation of state (3.7) with $\sigma=\tau$ to eliminate ρ from balance of mass (3.2). In this way, we find,

$$\frac{a}{r}\frac{da}{dr}=\frac{L}{H}\left[\frac{(D-\eta)+\beta\eta(p+2\sigma)}{(D-\eta)+\beta D(p+2\sigma)}\right] \quad . \tag{3.14}$$

In addition, we employ equation (3.14) and the definitions of Γ, Δ, and Δ_0 to write constitutive relation (3.10) explicitly in terms of σ and $p(r)$. In this manner, we obtain,

$$\sigma = \alpha p\left[1-\frac{r-\dfrac{Lr}{H}\left[\dfrac{(D-\eta)+\beta\eta(p+2\sigma)}{(D-\eta)+\beta D(p+2\sigma)}\right]}{r-\dfrac{Lr}{H}\left[\dfrac{(D-\eta)+\beta\eta p}{(D-\eta)+\beta D p}\right]}\right] \quad . \tag{3.15}$$

Equation (3.14) subjected to boundary conditions (3.3) and (3.4), and algebraic equation (3.15) can be solved in dimensionless form if the compressibility $\beta(r)$ is nondimensionalized by its centerline value $\beta_0 \equiv \beta(r=0)$.

In the forward problem, we prescribe the fluidity $\alpha(r)$, the compressibility ratio $\beta(r)/\beta_0$, the relative apparent density $\eta(r)/D$, and the relative compressed height H/L. Equations (3.14) and (3.15) determine the dimensionless pressure $\beta_0 p(r)$ and the dimensionless post-compaction radial location $a(r)/b$ to within an unknown constant radial pressure $\beta_0\sigma$ and an unknown constant of integration. The constants are determined by the two boundary conditions (3.3) and (3.4). With $a(r)/b$ and $\beta_0\sigma$ completely known, the relative green density $\rho(r)/D$ is determined by the equation of state (3.7), and the dimensionless compaction load $\beta_0 F/b^2$ is given by axial momentum balance (3.5).

In inverse problems, if the variations of the fluidity $\alpha(r)$ and the compressibility $\beta(r)/\beta_0$ are known, then it is possible to solve for the required initial pre-compaction relative density $\eta(r)/D$ that will yield a desired post-compaction relative density $\rho(r)/D$. Of particular interest are those density distributions $\eta(r)/D$ that yield uniform relative green densities $\rho(r)/D$ despite the presence of nonuniform $\alpha(r)$ and $\beta(r)/\beta_0$ in the initial fill. Solving for $\eta(r)/D$ in this manner is referred to as an inverse problem. Because

$\eta(r)/D$ is no longer prescribed, it must be found in terms of other quantities. To this end, we re-write equation of state (3.7) as a quadratic equation for $\eta(r)$:

$$\eta^2 + (\rho + D)(\beta(p + \sigma + \tau) - 1)\eta + \rho D = 0 \quad , \tag{3.16}$$

which yields

$$\eta = \frac{-(\rho + D)(\beta(p + \sigma + \tau) - 1) - \sqrt{(\rho + D)^2(\beta(p + \sigma + \tau) - 1)^2 - 4\rho D}}{2} \quad . \tag{3.17}$$

The second root of equation (3.17) is disregarded because it corresponds to values of $\eta(r)$ that are greater than D.

In order to solve the inverse problem, we employ equation (3.17) to eliminate η from equations (3.14) and (3.15). For a desired uniform value of the green density ratio ρ/D, and prescribed values $\alpha(r)$, $\beta(r)/\beta_0$, and H/L, the modified versions of equations (3.14) and (3.15) determine $\beta_0 p(r)$ and $a(r)/b$. The radial pressure $\beta_0\sigma$ and the constant of integration are again determined by the two boundary conditions. Once $a(r)/b$ and $\beta_0\sigma$ are known, the revised balance of mass (3.17) then determines the initial fill density ratio $\eta(r)/D$ needed to produce the desired green density. Finally, $\beta_0 F/b^2$ is given by axial momentum balance (3.5).

To solve the forward problem numerically, an initial guess for the radial pressure σ is required. At any r, for prescribed H/L, $\eta(r)$, $\alpha(r)$, $\beta(r)$ and D, equation (3.15) gives $p(r)$ by Newton-Raphson iteration. Equation (3.14) is a first order ordinary differential equation for $a(r)$ that can be integrated numerically from $r=0$ to $r=b$ using the Runge-Kutta method. The initial boundary condition required for this integration is given by equation (3.3). To determine the validity of the guessed value of radial pressure σ, the value of $a(r=b)$ is compared to b according to boundary condition (3.4). We then iterate on the guess of σ until the difference between the calculated value of $a(r=b)$ and b is within a specified error ε. The solution of the inverse problem is similar to the procedure for the forward problem except that equation (3.17) is used to eliminate η from equations (3.14) and (3.15).

3.4 Results and Discussion

In section 2.6, we approximated a single powder with continuously varying properties by dividing the powder into twenty concentric annular regions of powder. Each of these powders had its own properties. In this chapter, we have developed a model for the compaction of a single powder with continuously varying properties. In order to demonstrate that these models agree, we revisit a case first described in Figures 2.32 and 2.33. In this case, $\beta(r)/\beta_0=1$, $\alpha(r)=.5$, and $\eta(r)/D$ increases linearly from $(1/2.5)=.40$ at the centerline of the die, to $(1/2.25)=.444$ at the die wall. We focus on compaction heights $H/L=.6$ and $.5$. In Figures 3.3 and 3.4 respectively, we show as solid curves the variations of relative green density $\rho(r)/D$ and pressure $\beta_0 p(r)$ with radial position r/b predicted by the continuous model described here. The data obtained from the model described in Chapter 2 is shown as solid circles when the powder is

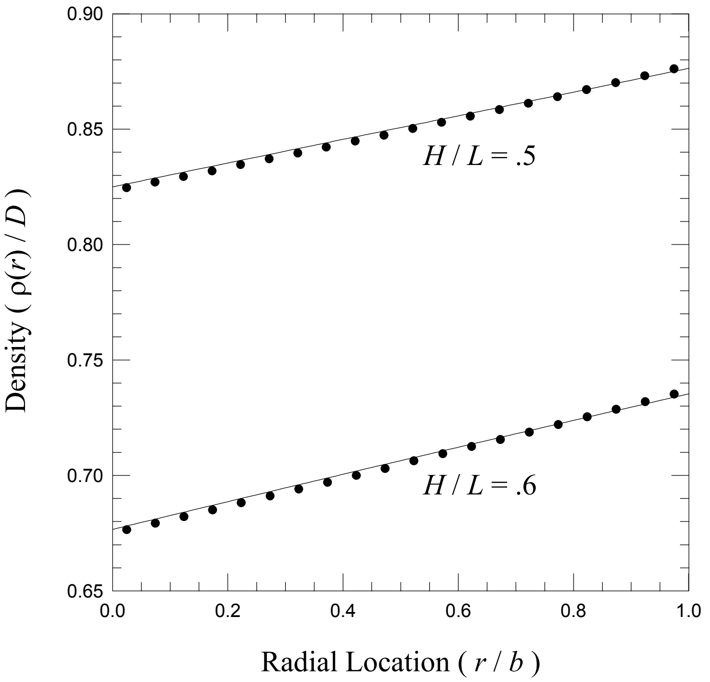

Figure 3.3: The variation of $\rho(r)/D$ with r/b when $\eta(r)/D$ varies linearly from .4 at the centerline to .444 at the die wall, $\alpha(r)$=.5, and $\beta(r)/\beta_0$=1, for H/L=.6 and .5.

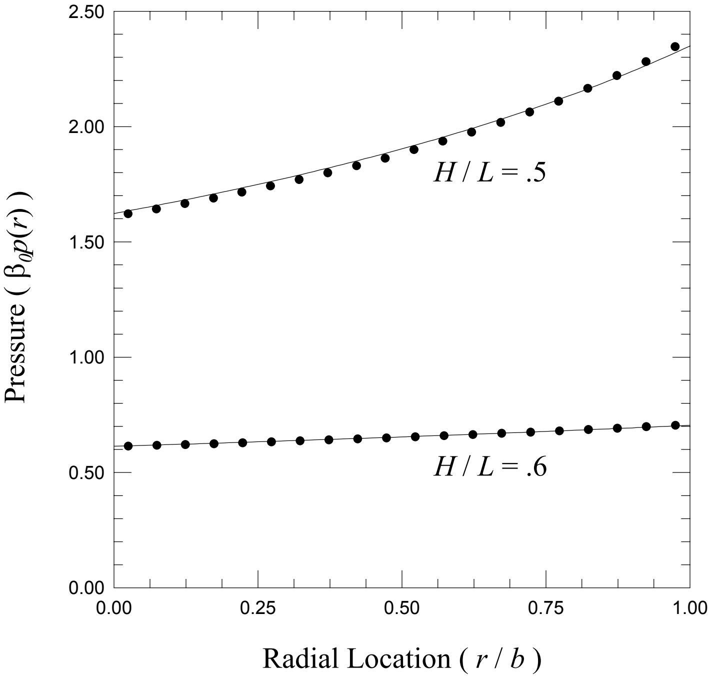

Figure 3.4: The variation of $\beta_0 p(r)$ with r/b corresponding to the two cases in Figure 3.3.

approximated by twenty discrete annular regions. Figures 3.3 and 3.4 demonstrate that there is excellent agreement between the continuous model and the discrete (20-powder) model. For this reason, in what follows, we show only the results predicted by the continuous model.

Next, we consider a case in which the compressibility $\beta(r)/\beta_0=1$ is uniform, the relative apparent density $\eta(r)/D$ is everywhere equal to (1/2.25)=.444, but due to uneven powder blend $\alpha(r)$ increases linearly from .25 at the centerline to .75 at the die wall. In Figure 3.5 we show the resulting variation of relative green density $\rho(r)/D$ with radial position r/b for compacted heights H/L=.6 and .5. As expected, the overall magnitude of the density increases as the compaction height decreases. However, because of the radial increase in fluidity, the capacity of the material to expand radially increases with distance from the centerline. Greater radial expansion further from the centerline, in turn, causes the density to decrease with radial distance from the centerline.

In Figure 3.6, we show the corresponding variations of pressure $\beta_0 p(r)$. As expected, the overall pressure levels increase with decreasing compaction height. The pressures at H/L=.5 are particularly high because the corresponding densities are approximately ninety percent of their theoretical maximum. Where $\alpha(r)$ is relatively low (i.e. near the centerline), more axial pressure is required to generate the radial pressure needed for radial equilibrium. The increase in $\alpha(r)$ with radial distance from the centerline, therefore, causes a corresponding decrease in $\beta_0 p(r)$. A secondary cause of this pressure decrease is due to the corresponding decrease in density observed in Figure 3.5. As the density decreases, the local compressibility increases, and the required

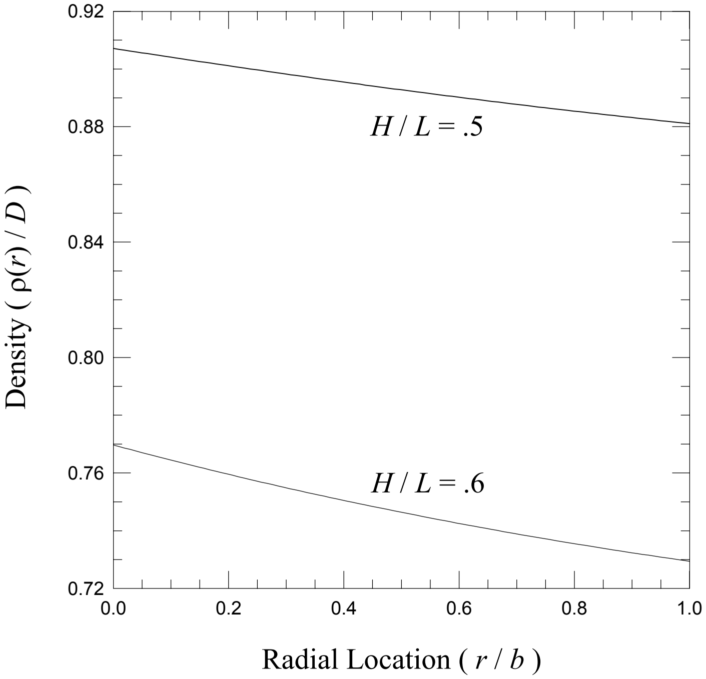

Figure 3.5: The variation of $\rho(r)/D$ with r/b when $\alpha(r)$ varies linearly from .25 at the centerline to .75 at the die wall, $\eta(r)/D$=.444, and $\beta(r)/\beta_0$=1, for H/L=.6 and .5.

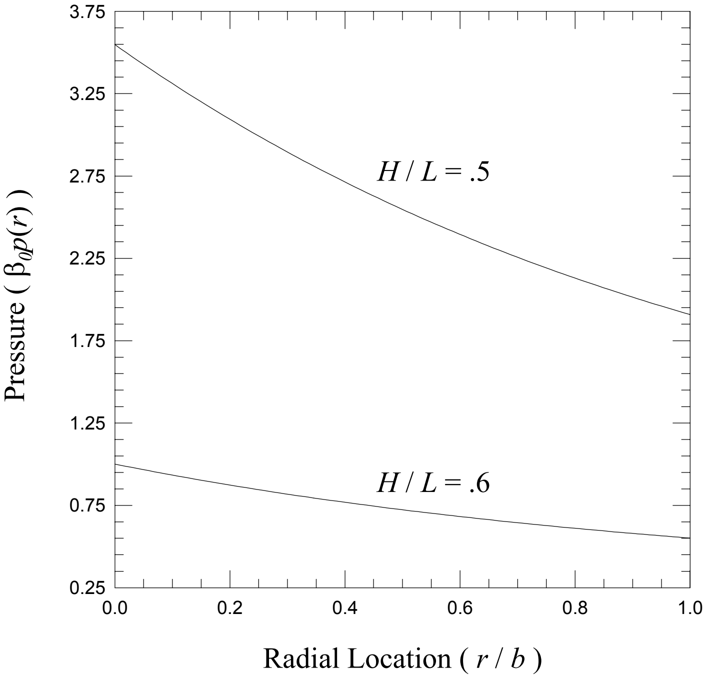

Figure 3.6: The variation of $\beta_0 p(r)$ with r/b corresponding to the two cases in Figure 3.5.

pressure decreases. The radial decrease in axial pressure is due to a combination of these two causes.

As a third case, we consider hypothetical circumstances in which the fluidity $\alpha(r)=.5$ is uniform, the relative apparent density $\eta(r)/D$ is everywhere equal to $(1/2.25)=.444$, but due to uneven powder blend the compressibility $\beta(r)/\beta_0$ decreases linearly from 1 at the centerline to .5 at the die wall. In Figure 3.7 we show the resulting variation of relative green density $\rho(r)/D$ with radial position r/b for compacted heights $H/L=.6$ and .5. As expected, the overall magnitude of the density increases as the compaction height decreases. Furthermore, regions of powder with higher compressibilities become denser than regions with lower compressibilities. As a consequence of the radial decrease in compressibility, in this case, the density decreases with radial distance from the centerline.

In Figure 3.8, we show the corresponding variations of pressure $\beta_0 p(r)$. As expected, the overall pressure levels increase with decreasing compaction height. Where $\beta(r)/\beta_0$ is relatively high (i.e. near the centerline), less axial pressure is required to compact the powder. The decrease in $\beta(r)/\beta_0$ with radial distance from the centerline, therefore, causes a corresponding increase in $\beta_0 p(r)$. Interestingly, the decrease in density observed in Figure 3.7 has an opposite effect on the pressure. As the density decreases, the local compressibility of the powder increases and the required pressure decreases. The fact that pressure ultimately increases with distance from the centerline in Figure 3.8 is evidence that the decrease of $\beta(r)/\beta_0$ with r/b dominates during compaction.

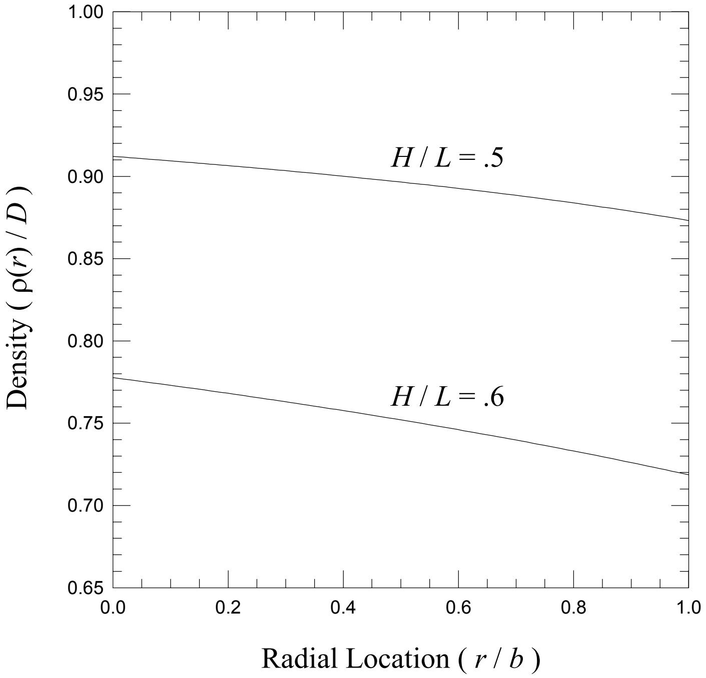

Figure 3.7: The variation of $\rho(r)/D$ with r/b when $\beta(r)/\beta_0$ varies linearly from 1 at the centerline to .5 at the die wall, $\eta(r)/D$=.444 and $\alpha(r)$=.5, for H/L=.6 and .5.

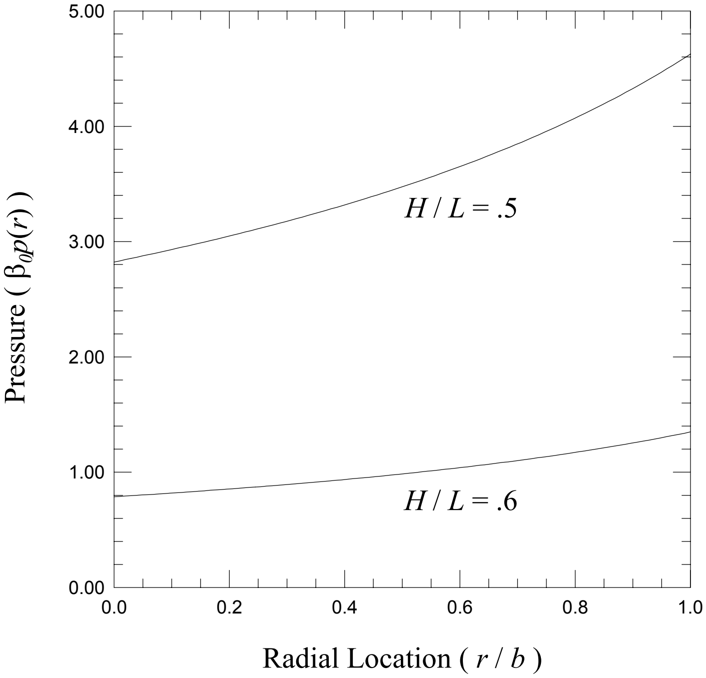

Figure 3.8: The variation of $\beta_0 p(r)$ with r/b corresponding to the two cases in Figure 3.7.

In Figure 3.9, we show the results of two inverse problems. For each problem, we specify the initial pre-compaction variations of $\alpha(r)$ and $\beta(r)/\beta_0$, the desired uniform green density $\rho(r)/D$, and the final compaction height H/L. We then compute the required initial apparent density distribution. In both problems, we assume that $\alpha(r)$ increases exponentially from .25 at r/b=0 to .75 at r/b=1, and $\beta(r)/\beta_0$ decreases exponentially from 1 at r/b=0 to .5 at r/b=1. The mathematical expressions for $\alpha(r)$ and $\beta(r)/\beta_0$ are given by:

$$\alpha(r) = .25\exp[1.0986\, r/b] \quad , \tag{3.18}$$

and

$$\beta(r)/\beta_0 = \exp[-.6931\, r/b] \quad . \tag{3.19}$$

In the first problem, we require that ρ/D=.9 at H/L=.5, and label the required apparent density distribution as H/L=.5 in Figure 3.9. In the second problem, we require that ρ/D=.5 at H/L=.9, and label the required apparent density distribution as H/L=.9. Near the centerline, where $\alpha(r)$ is relatively low and $\beta(r)/\beta_0$ is relatively high, the material tends to contract radially and densify more readily. Along the die wall, where $\alpha(r)$ is relatively high and $\beta(r)/\beta_0$ is relatively low, the material tends to expand radially and densify less readily. To offset these effects and to ensure uniform final density, the initial density must therefore be lower where $\alpha(r)$ is relatively low and $\beta(r)/\beta_0$ is relatively high. For both inverse cases, then, the initial density increases with radial distance from the

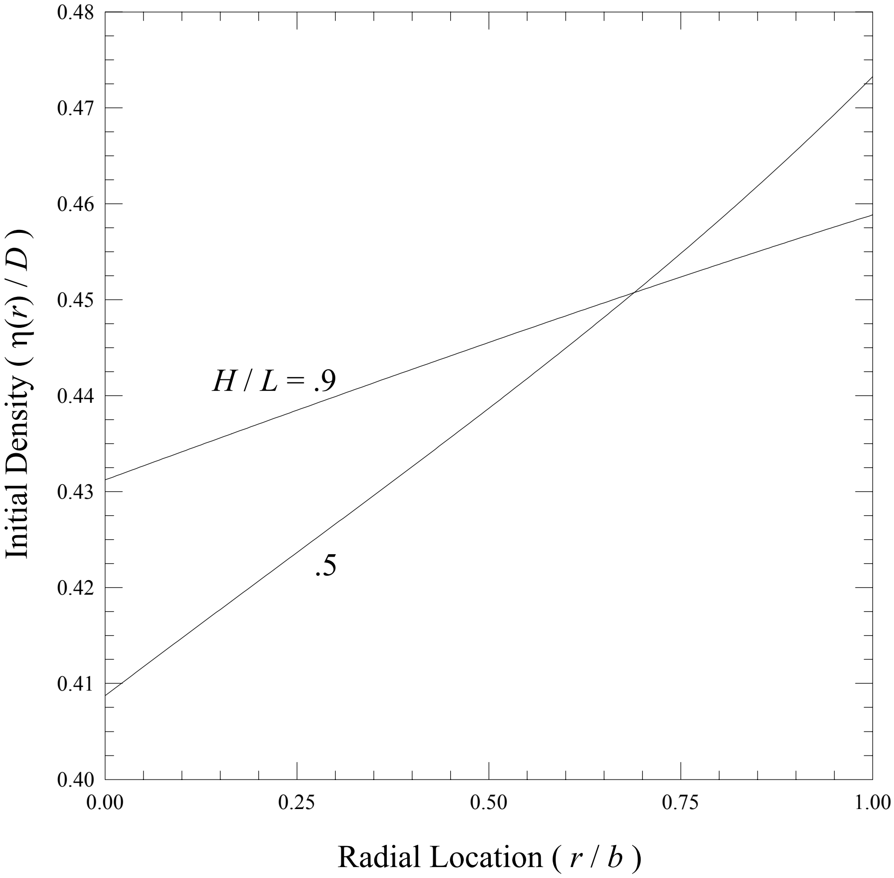

Figure 3.9: The variations of $\eta(r)/D$ with r/b required to yield ρ/D=.9 at H/L=.5 and ρ/D=.5 at H/L=.9 when $\alpha(r)$=.25exp[1.0986r/b] and $\beta(r)/\beta_0$=exp[-.6931r/b].

centerline. For the first inverse problem, this variation is more pronounced because we require a higher uniform green density at a lower compacted height.

In Figure 3.10, we show for the first inverse problem in Figure 3.9 the evolution of $\rho(r)/D$ as compacted height H/L decreases from 1 to .5. In this case, $\alpha(r)$ is given by equation (3.18), $\beta(r)/\beta_0$ is given by equation (3.19), and $\eta(r)/D$ is given by the curve labeled H/L=.5 in Figure 3.9 to yield ρ/D=.9 at H/L=.5. As expected, the overall magnitude of the density increases as compaction height decreases. At H/L=1, compaction has not yet begun, so $\rho(r)/D$ is equal to $\eta(r)/D$ given for the first inverse problem (H/L=.5) in Figure 3.9. As compaction proceeds, two effects govern the evolving density variations. The first effect is due to the variation of the powder properties. In this case, the distributions of $\alpha(r)$ and $\beta(r)/\beta_0$ cause powder near the centerline to densify more rapidly than powder near the die wall. As H/L decreases from 1 to about .6, this effect dominates the compaction behavior, and the powder near the centerline densifies more rapidly than powder near the die wall. In fact, when H/L decreases to .7, powder near the centerline becomes more dense than powder near the die wall. The second effect is due to the local compressibility of the powder. Regions of powder that are more dense than others are inherently less compressible than less dense regions. In fact, somewhere between H/L=.6 and H/L=.5, the dense powder near the centerline densifies less readily than powder near the die wall. Consequently, the density distribution flattens to the specified uniform density of ρ/D=.9 at H/L=.5.

In Figure 3.11, we show the evolution of pressure $\beta_0 p(r)$ corresponding to Figure 3.10. As expected, the overall pressure levels increase with decreasing compaction

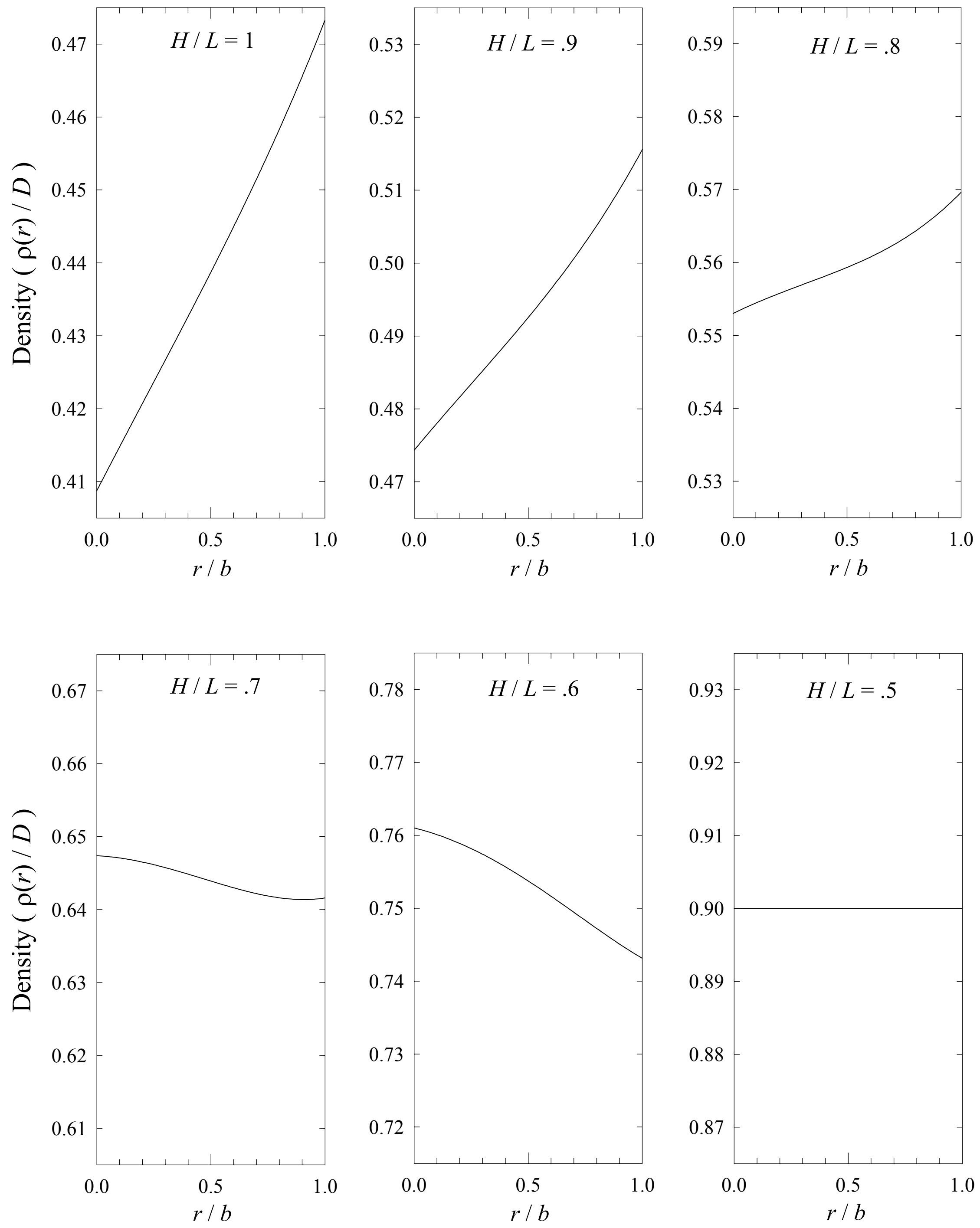

Figure 3.10: The evolution of $\rho(r)/D$ as H/L decreases from 1 to .5 when $\alpha(r)=.25\exp[1.0986r/b]$, $\beta(r)/\beta_0=\exp[-.6931r/b]$, and $\eta(r)/D$ is chosen to yield $\rho/D=.9$ at $H/L=.5$.

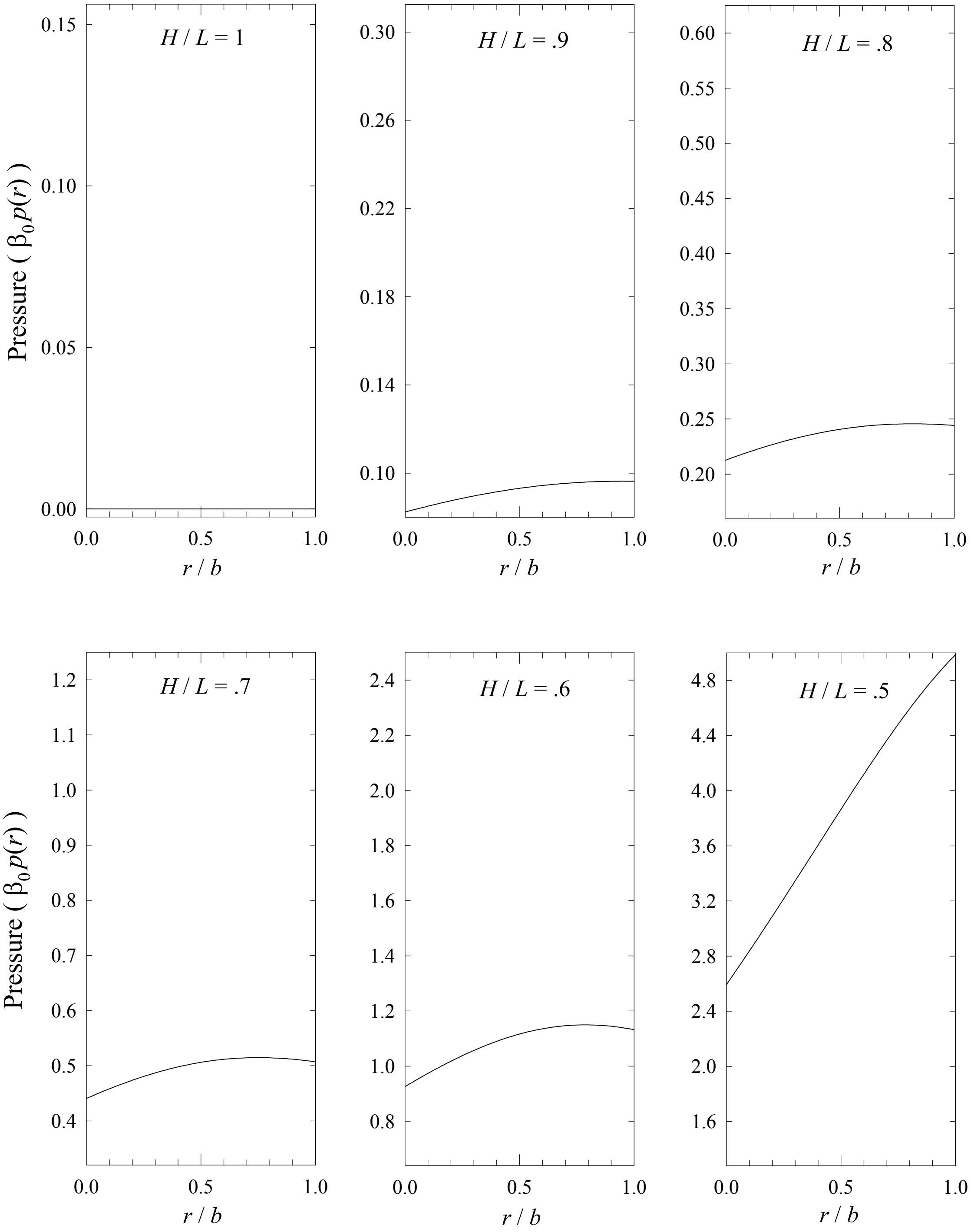

Figure 3.11: The evolution of $\beta_0 p(r)$ corresponding to Figure 3.10.

height. At H/L=1, compaction has not yet begun, and there is no pressure developed. The given variations (3.18) and (3.19) of $\alpha(r)$ and $\beta(r)/\beta_0$ actually have opposite effects on the final pressure distribution. As $\alpha(r)$ increases with radial distance, the pressure required to satisfy radial equilibrium decreases. On the other hand, as $\beta(r)/\beta_0$ decreases with radial distance, the pressure required for compression increases. Figure 3.11 demonstrates that the second of these effects is greater than the first. For any value of H/L that is less than 1, the pressure increases monotonically with radial distance from the centerline. The pressure becomes increasingly nonuniform as H/L decreases to .5. Interestingly, due to the initial nonuniformities in fluidity and compressibility, when the final density is uniform the pressure is not.

For contrast, in Figure 3.12, we show for the second inverse problem in Figure 3.9 the evolution of $\rho(r)/D$ as compacted height H/L decreases from 1 to .5. In this case, $\alpha(r)$ is given by equation (3.18), $\beta(r)/\beta_0$ is given by equation (3.19), and $\eta(r)/D$ is given by the curve labeled H/L=.9 in Figure 3.9 to yield ρ/D=.5 at H/L=.9. When H/L=1, $\rho(r)/D$ is equal to $\eta(r)/D$ given for the second inverse problem (H/L=.9) in Figure 3.9. As compaction proceeds, the variations of $\alpha(r)$ and $\beta(r)/\beta_0$ cause the material near the centerline to densify more rapidly than powder near the die wall. The density distribution flattens out and, by design, transforms into a perfectly uniform density variation at H/L=.9. As H/L decreases from .9 to .6, powder near the centerline continues to densify more rapidly than powder near the die wall and the uniform density of ρ/D evolves into variations that decrease monotonically with distance from the centerline. These variations of $\rho(r)/D$ becomes increasingly more nonuniform as H/L decreases from .9 to

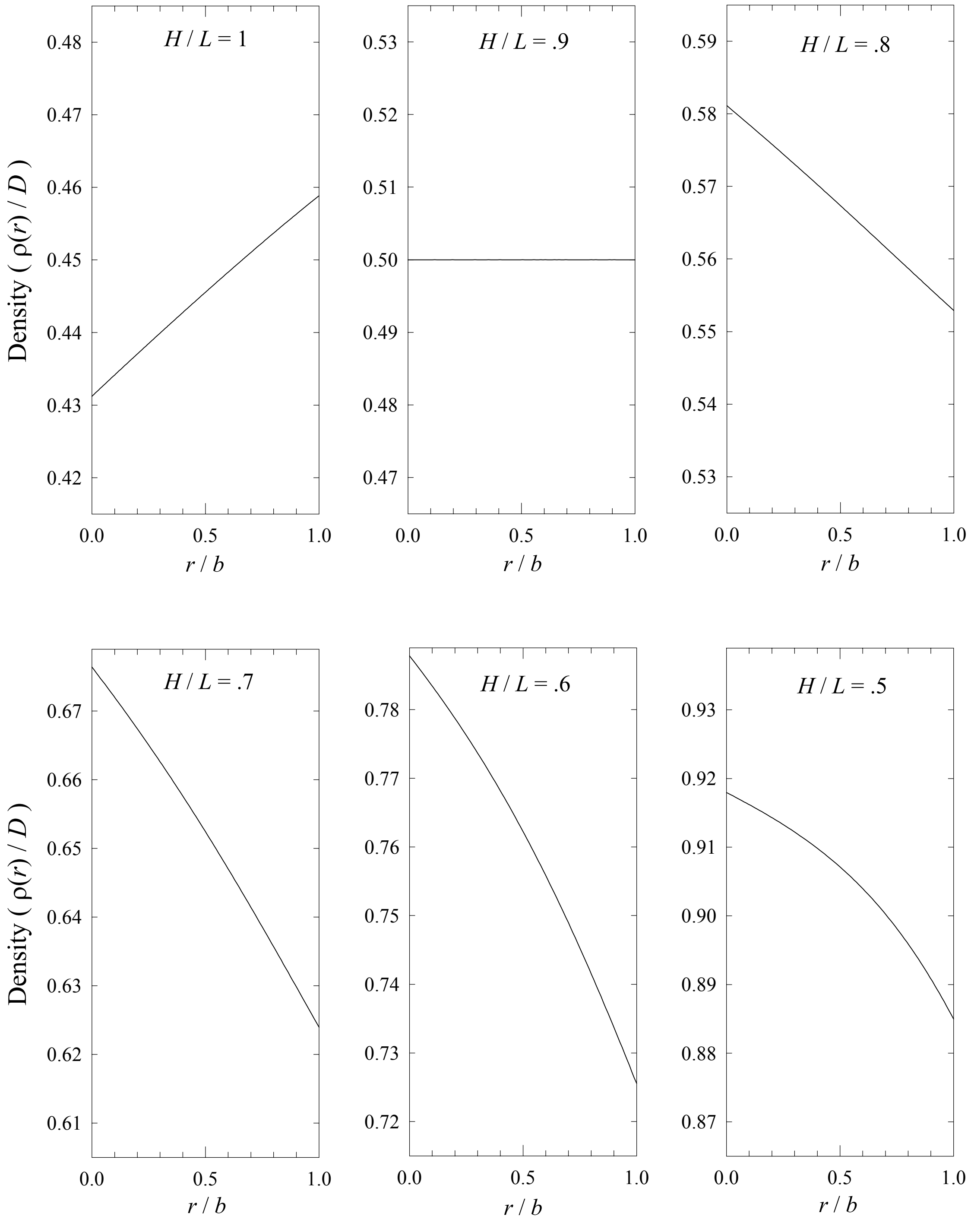

Figure 3.12: The evolution of $\rho(r)/D$ as H/L decreases from 1 to .5 when $\alpha(r)$=.25exp[1.0986r/b], $\beta(r)/\beta_0$=exp[-.6931r/b], and $\eta(r)/D$ is chosen to yield ρ/D=.5 at H/L=.9.

.6. However, somewhere between *H*/*L*=.6 and *H*/*L*=.5 the higher densities near the centerline make the powder more difficult to compress there and the density variation becomes less nonuniform as *H*/*L* proceeds to .5. In Figure 3.13, we show the variations of pressure $\beta_0 p(r)$ corresponding to Figure 3.12. The trends observed here are similar to those observed in Figure 3.11. Again, when the density is perfectly uniform (at *H*/*L*=.9), the pressure is not.

In Figure 3.14, we show the results of two additional inverse problems. In both problems, $\alpha(r)$ varies parabolically from .25 at r/b=0, to a maximum value of 1 at r/b=.5, to .25 at r/b=1. By contrast, $\beta(r)/\beta_0$ varies parabolically from 1 at r/b=0, to a minimum value of .25 at r/b=.5, to 1 at r/b=1. Mathematically, the expressions for $\alpha(r)$ and $\beta(r)/\beta_0$ are given by:

$$\alpha(r) = -3(r/b)^2 + 3r/b + .25 \quad , \tag{3.20}$$

and

$$\beta(r)/\beta_0 = 3(r/b)^2 - 3r/b + 1 \quad . \tag{3.21}$$

In the first problem, we require that ρ/D=.9 at *H*/*L*=.5, and label the required apparent density distribution as *H*/*L*=.5 in Figure 3.14. In the second problem, we require that ρ/D=.5 at *H*/*L*=.9, and label the required apparent density distribution as *H*/*L*=.9. Along the centerline and the die wall, where $\alpha(r)$ is relatively low and $\beta(r)/\beta_0$ is relatively high, the material tends to contract radially and densify more readily. At r/b=.5, where $\alpha(r)$ is

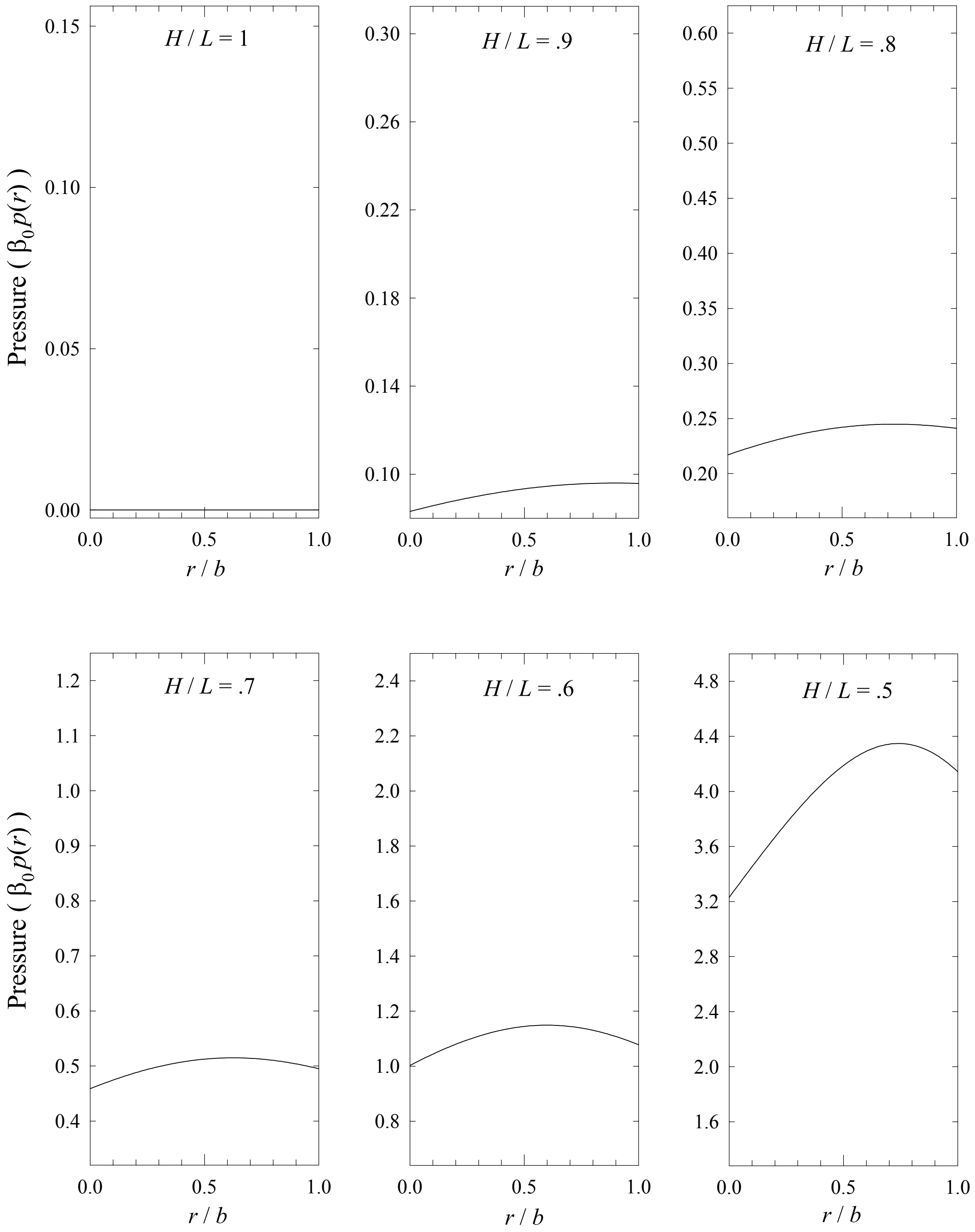

Figure 3.13: The evolution of $\beta_0 p(r)$ corresponding to Figure 3.12.

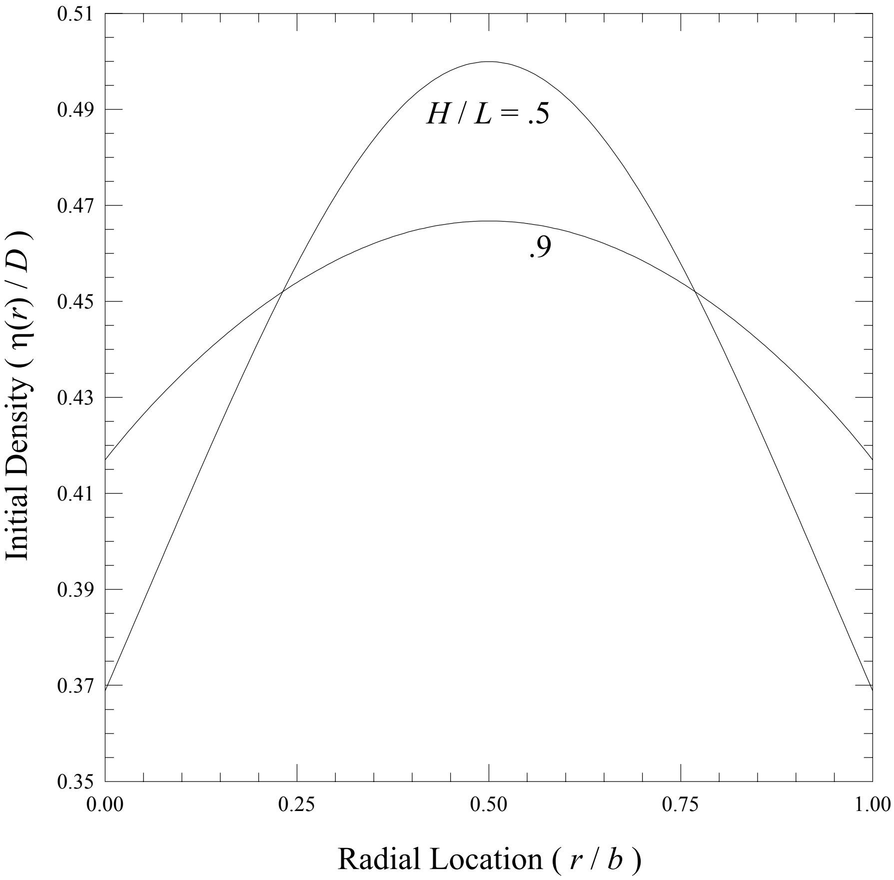

Figure 3.14: The variations of $\eta(r)/D$ with r/b required to yield ρ/D=.9 at H/L=.5 and ρ/D=.5 at H/L=.9 when $\alpha(r)=-3(r/b)^2+3r/b+.25$ and $\beta(r)/\beta_0=3(r/b)^2-3r/b+1$.

maximum and $\beta(r)/\beta_0$ is minimum, the material tends to expand radially and densify less readily. To ensure uniform final density, the initial density must therefore be lower where the material densifies more readily (i.e. near the centerline and the die wall) and higher where the material densifies less readily (i.e. near r/b=.5). For both inverse cases, therefore, the required initial density increases with radial distance from r/b=0 to r/b=.5 and decreases with radial distance from r/b=.5 to r/b=1. This variation is more pronounced for the first inverse problem because it yields a uniform green density at a much later stage in the compaction.

In Figure 3.15, we show for the first inverse problem of Figure 3.14 the evolution of $\rho(r)/D$ as compacted height H/L decreases from 1 to .5. In this case, $\alpha(r)$ is given by equation (3.20), $\beta(r)/\beta_0$ is given by equation (3.21), and $\eta(r)/D$ is given by the curve labeled H/L=.5 in Figure 3.14 to yield ρ/D=.9 at H/L=.5. At H/L=1, compaction has not yet begun and $\rho(r)/D$ is equal to $\eta(r)/D$ given for the first inverse problem (H/L=.5) in Figure 3.14. As compaction proceeds from H/L=1 to H/L=.6, the variations of $\alpha(r)$ and $\beta(r)/\beta_0$ cause powder near the centerline and the die wall to densify more rapidly than powder near r/b=.5. In fact, when H/L has decreased to .6, powder near the centerline and the die wall has actually become more dense than powder near r/b=.5. Somewhere between H/L=.6 and H/L=.5, a secondary effect reverses this trend. The dense powder near the centerline and the die wall becomes more difficult to compact than the less dense powder near r/b=.5. As a result, the densities near r/b=.5 increase most rapidly and the density distribution flattens out beyond H/L=.6. By design, the distribution becomes perfectly uniform at H/L=.5.

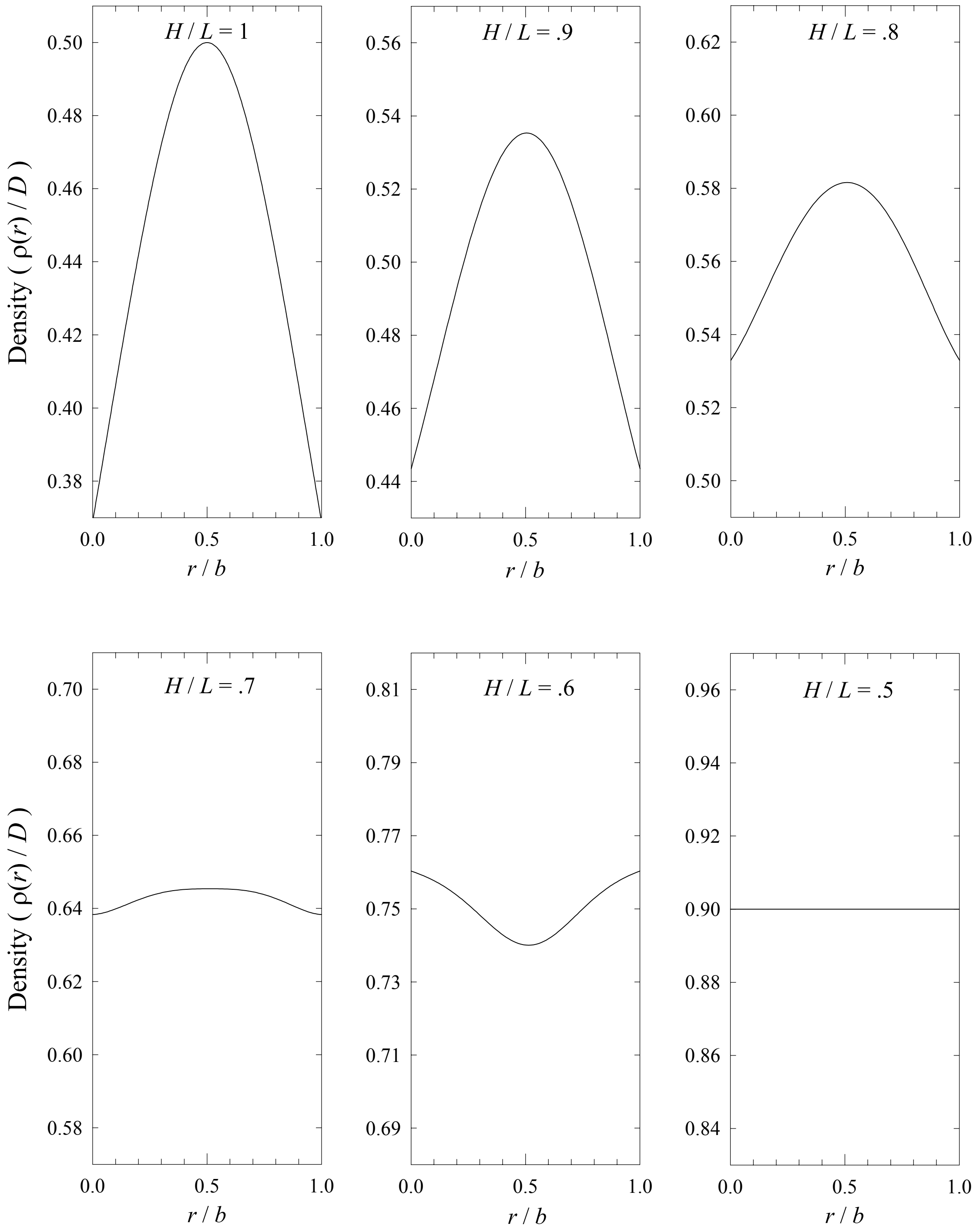

Figure 3.15: The evolution of $\rho(r)/D$ as H/L decreases from 1 to .5 when $\alpha(r)=-3(r/b)^2+3r/b+.25$, $\beta(r)/\beta_0=3(r/b)^2-3r/b+1$, and $\eta(r)/D$ is chosen to yield $\rho/D=.9$ at $H/L=.5$.

In Figure 3.16, we show the evolution of pressure $\beta_0 p(r)$ corresponding to Figure 3.15. At $H/L=1$, there is no pressure yet developed. Increases in $\alpha(r)$ and $\beta(r)/\beta_0$ cause decreases in the required pressure; decreases in $\alpha(r)$ and $\beta(r)/\beta_0$ cause increases in the required pressure. According to variations (3.20) and (3.21), $\alpha(r)$ increases where $\beta(r)/\beta_0$ decreases ($0<r/b<.5$), and $\alpha(r)$ decreases where $\beta(r)/\beta_0$ increases ($.5<r/b<1$). Consequently, the variations of $\alpha(r)$ and $\beta(r)/\beta_0$ given by equations (3.20) and (3.21) have opposite effects on the evolving pressure distribution. The variation of $\alpha(r)$ causes $\beta_0 p(r)$ to decrease in the range $0<r/b<.5$ and increase in the range $.5<r/b<1$. The variation of $\beta(r)/\beta_0$, on the other hand, causes $\beta_0 p(r)$ to increase in the range $0<r/b<.5$ and decrease in the range $.5<r/b<1$. According to Figure 3.16, apparently the effect of $\beta(r)/\beta_0$ on the pressure is greater than the effect of $\alpha(r)$. Interestingly, as H/L decreases, the density becomes more uniform but the pressure becomes more nonuniform. In fact, $\beta_0 p(r)$ is most nonuniform (at $H/L=.5$) when the density is perfectly uniform.

In Figure 3.17, we show for the second inverse problem described in Figure 3.14 the evolution of $\rho(r)/D$ as compacted height H/L decreases from 1 to .5. In this case, $\alpha(r)$ is given by equation (3.20), $\beta(r)/\beta_0$ is given by equation (3.21), and $\eta(r)/D$ is given by the curve labeled $H/L=.9$ in Figure 3.14 to yield $\rho/D=.5$ at $H/L=.9$. When $H/L=1$, $\rho(r)/D$ is equal to $\eta(r)/D$ given for the second inverse problem ($H/L=.9$) in Figure 3.14. As compaction proceeds, the variations of $\alpha(r)$ and $\beta(r)/\beta_0$ cause the material near the centerline and the die wall to densify more rapidly than powder near $r/b=.5$. Consequently, the variation of $\rho(r)/D$ flattens out and, by design, becomes uniform at

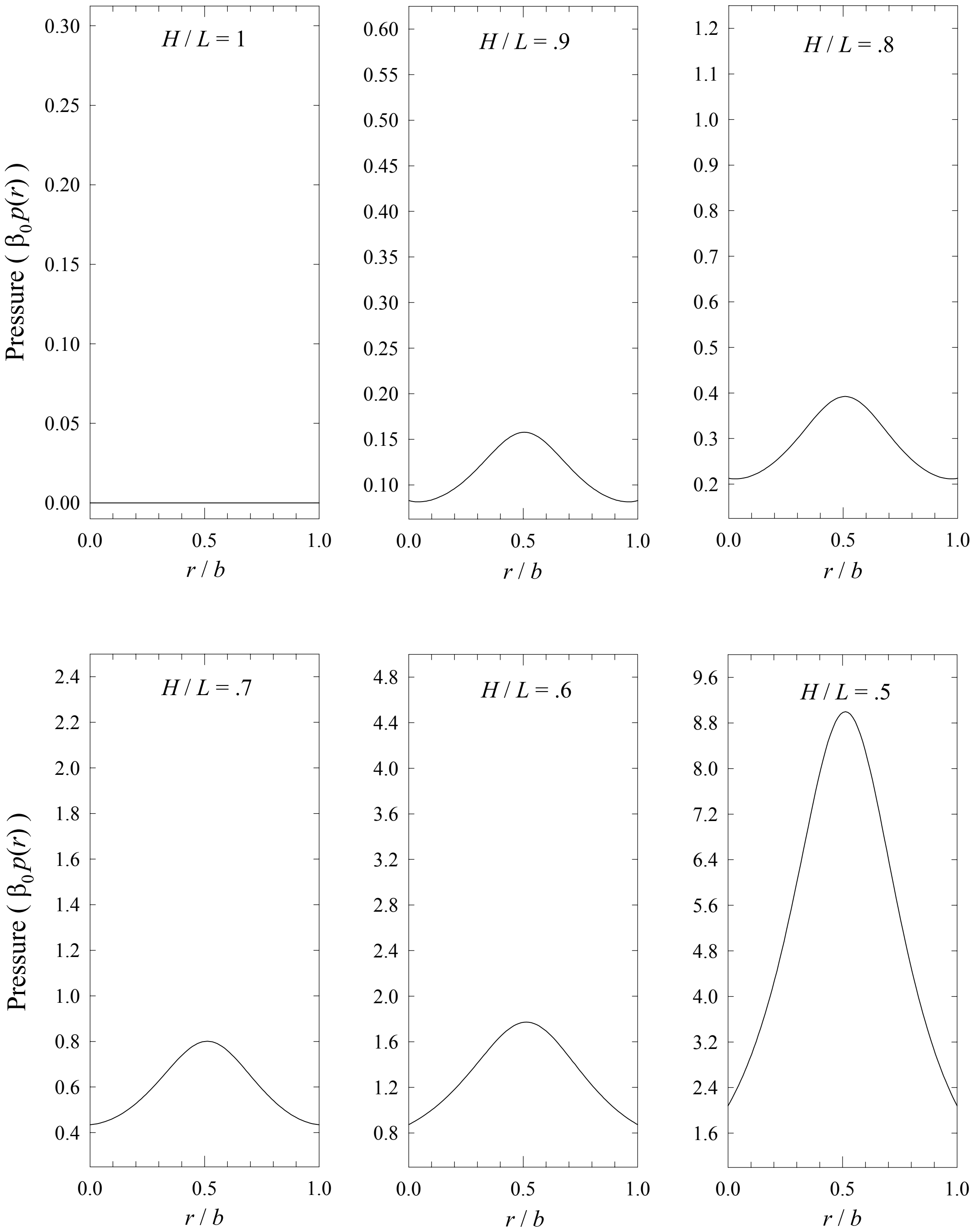

Figure 3.16: The evolution of $\beta_0 p(r)$ corresponding to Figure 3.15.

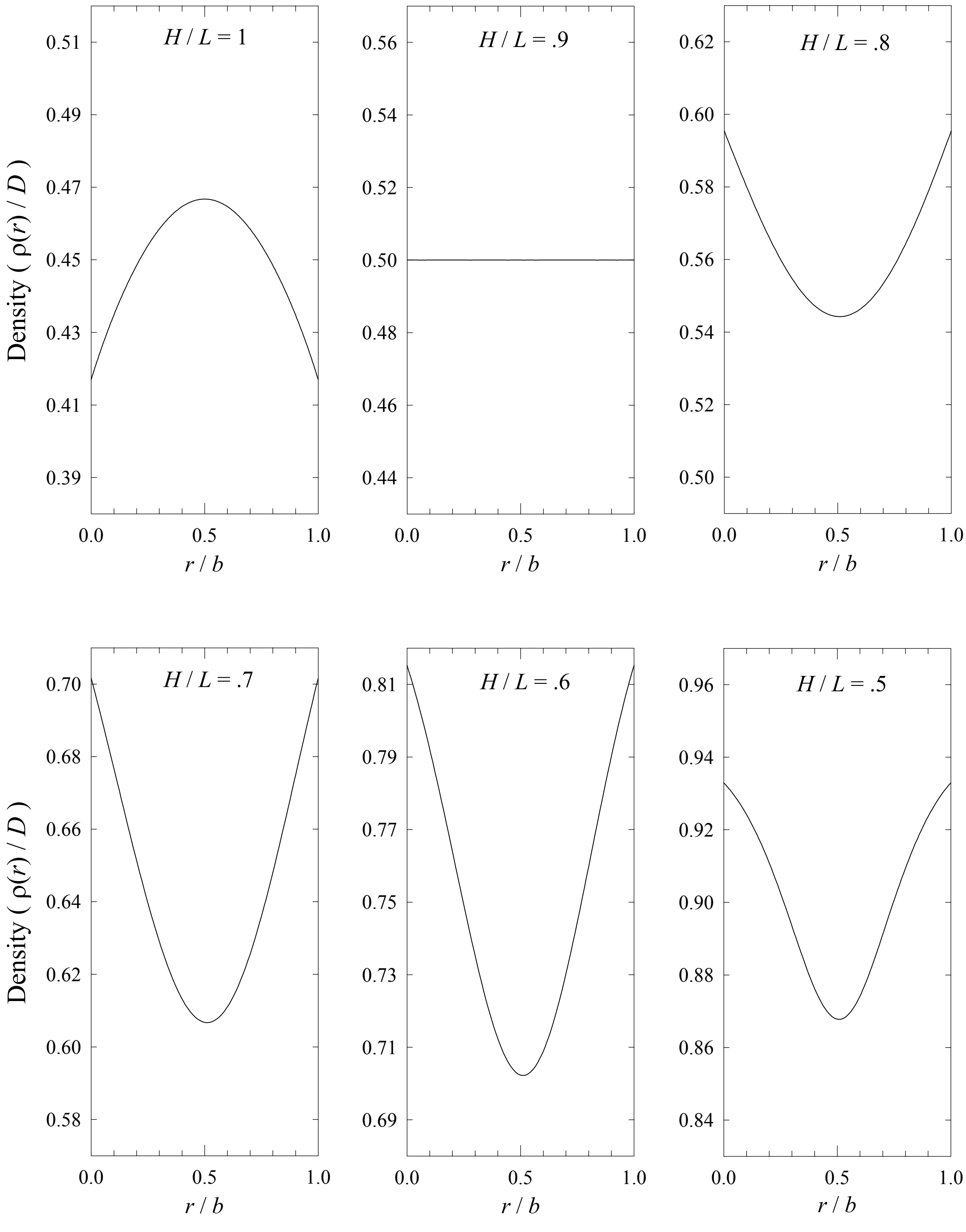

Figure 3.17: The evolution of $\rho(r)/D$ as H/L decreases from 1 to .5 when $\alpha(r)$=-3$(r/b)^2$+3r/b+.25, $\beta(r)/\beta_0$=3$(r/b)^2$-3r/b+1, and $\eta(r)/D$ is chosen to yield ρ/D=.5 at H/L=.9.

H/L=.9. As H/L decreases beyond .9 to .6, powder near the centerline and the die wall densifies more rapidly than powder near r/b=.5, the uniform density ρ/D evolves into a variation that decreases as in the range $0<r/b<.5$ and increases in the range $.5<r/b<1$, and the variation of $\rho(r)/D$ becomes increasingly nonuniform. Between H/L=.6 and H/L=.5, the denser powder near the centerline and the die wall becomes more difficult to compact than the powder near r/b=.5. The variation of $\rho(r)/D$ therefore becomes less nonuniform as H/L decreases beyond .6. In Figure 3.18, we show the variations of pressure $\beta_0 p(r)$ corresponding to Figure 3.17. As expected, the trends observed here are similar to those observed in Figure 3.16.

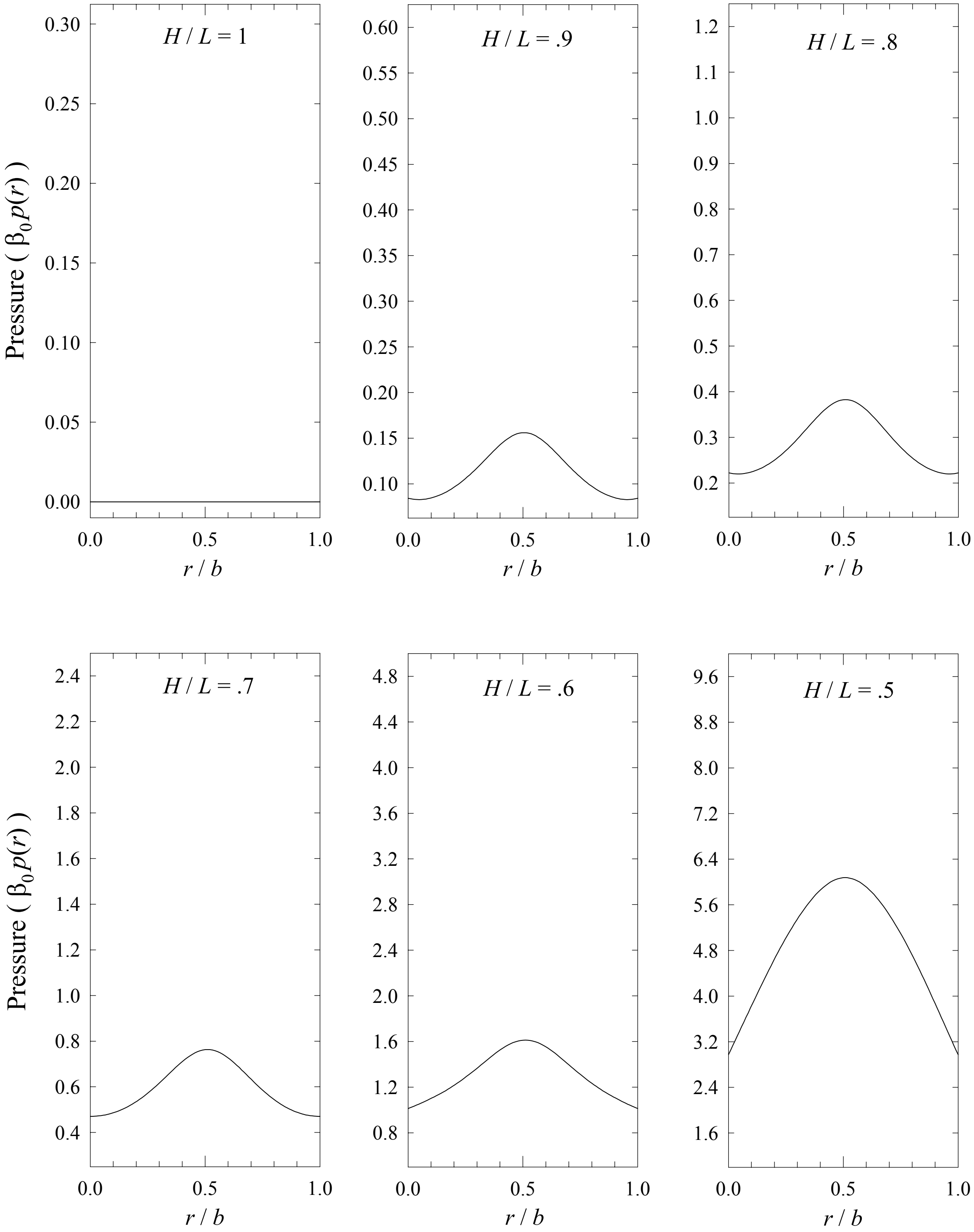

Figure 3.18: The evolution of $\beta_0 p(r)$ corresponding to Figure 3.17.

CHAPTER 4

Compaction in Hollow Cylindrical Dies with Frictional Core Rods and Die Walls

4.1 <u>Governing Equations and Boundary Conditions</u>

We are concerned with single punch compaction of a powder in a hollow cylindrical die of inside radius R_i and outside radius R_o. The height of the powder before compaction is L, and the height after compaction is H. The geometry of the compact is described by the following dimensionless quantities: the radii ratio $a \equiv R_i/R_o$, which is a measure of the wall thickness of the compact; the height ratio H/L, which is a measure of the degree of compaction; and the aspect ratio $h \equiv H/R_o$, which is a dimensionless measure of the height of the compact. The geometry of the compact is shown in Figure 4.1.

The average pressure applied over the top surface of the compact is p_o, so that the total compaction load F is equal to $\pi(R_o^2 - R_i^2)p_o$. We establish a cylindrical coordinate system in which the axial z^*–coordinate measures distance along the centerline from the lower face of the compact, and the radial r^*-coordinate measures distance from the centerline. Because of symmetry, there are no variations with angle of rotation about the centerline. The axial pressure p^*, the radial pressure σ^*, the tangential pressure φ^* and the shear stress τ^* each vary with r^* and z^* throughout the compact.

In what follows, we employ a dimensionless axial coordinate $z \equiv z^*/H$ which varies from 0 at the bottom of the compact to 1 at the top; and a dimensionless radial coordinate

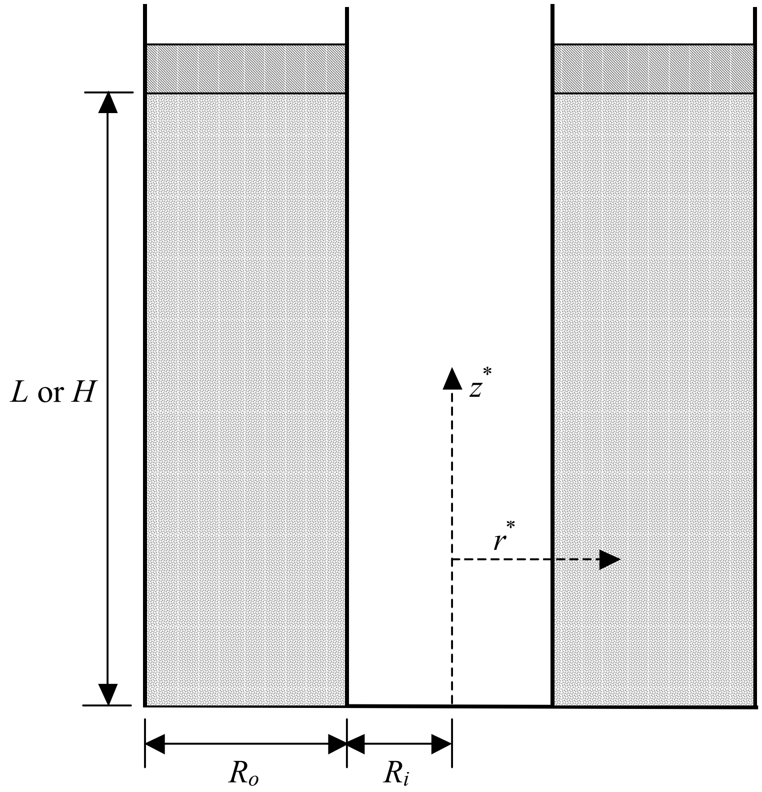

Figure 4.1: The pre- and post-compaction geometry.

$r \equiv r^*/R_o$, which varies from a at the core rod to 1 at the die wall. The dimensionless axial pressure $p \equiv p^*/p_o$ and the dimensionless radial pressure $\sigma \equiv \sigma^*/p_o$, the dimensionless tangential pressure $\varphi \equiv \varphi^*/p_o$, and the dimensionless shear stress $\tau \equiv \tau^*/p_o$ vary with r and z. In what follows, we carry out all calculations in terms of dimensionless quantities.

In terms of the axial pressure p and the shear stress τ, the axial equilibrium equation is given by,

$$\frac{\partial p}{\partial z} = \frac{h}{r}\frac{\partial (r\tau)}{\partial r} \quad . \tag{4.1}$$

In terms of the radial pressure σ and the shear stress τ, the radial equilibrium equations is,

$$\frac{\partial \sigma}{\partial r} = \frac{1}{h}\frac{\partial \tau}{\partial z} \quad . \tag{4.2}$$

The tangential equilibrium equation requires that the radial pressure balance the tangential pressure; that is $\sigma=\varphi$. In this model, the radial pressure σ is induced by an axial pressure p according to the simple constitutive relation,

$$\sigma = \alpha p \quad , \tag{4.3}$$

where α is the fluidity of the powder that measures the tendency of the powder to develop radial pressure when subjected to axial pressure. Values of α vary between 0 and 1. For simplicity, we take α to be a constant and ignore its variations with density in the course of compaction. The constant value may be crudely interpreted as an average value over the entire compact during the entire compaction process.

With appropriate boundary conditions, equations (4.1), (4.2) and (4.3) determine the variations of the axial pressure, the radial pressure, and the shear stress. Boundary conditions at the die wall and the core rod relate the shear stress to the radial pressure through Coulomb friction. If, for example, μ_o is the coefficient of friction between the die wall and the powder compact, then the boundary condition at r=1 is given by,

$$\tau(r=1,z)=\mu_o\sigma(r=1,z) \quad . \tag{4.4}$$

Similarly, if μ_i is the coefficient of friction between the core rod and the powder compact, then the corresponding boundary condition at r=a is

$$\tau(r=a,z)=-\mu_i\sigma(r=a,z) \quad . \tag{4.5}$$

It is possible to obtain closed form expressions for the pressures p and σ, and the shear stress τ that satisfy equations (4.1) to (4.3) and conditions (4.4) and (4.5).

Constitutive relation (4.3) may be employed to eliminate σ from the radial equilibrium equation (4.2). The result may be combined by cross differentiation with axial equilibrium (4.1) to yield a single equation for τ, given by,

$$\frac{\partial}{\partial r}\left[\frac{1}{r}\frac{\partial(r\tau)}{\partial r}\right]=\frac{1}{\alpha h^2}\frac{\partial^2\tau}{\partial z^2} \quad . \tag{4.6}$$

In order to express conditions (4.4) and (4.5) entirely in term of the shear stress τ, we employ constitutive relation (4.3) to write the radial pressure σ in terms of the axial pressure p, differentiate the two conditions with respect to z, and employ equation (4.1) to eliminate $\partial p/\partial z$ from the intermediate results. In this manner, we obtain

$$\frac{\partial \tau}{\partial z} = \mu_o \alpha h \left[\frac{\partial \tau}{\partial r} + \tau \right] \quad , \tag{4.7}$$

at r=1, and

$$\frac{\partial \tau}{\partial z} = -\mu_i \alpha h \left[\frac{\partial \tau}{\partial r} + \frac{\tau}{a} \right] \quad , \tag{4.8}$$

at r=a. Equation (4.6) and conditions (4.7) and (4.8) determine $\tau(r,z)$. In the case of a solid cylindrical compact, the ratio a is equal to 0, and condition (4.8) at r=a is replaced by the simple requirement that the stresses remain finite at r=0.

4.2 Determination of Dimensionless Shear Stress and Pressures

Based on the form of equation (4.6) for $\tau(r,z)$, the shear stress has the form,

$$\tau(r,z) = Z(z)R(r) \quad , \tag{4.9}$$

where the functions $Z(z)$ and $R(r)$ are to be determined. An equation for $R(r)$ and an equation for $Z(z)$ may be obtained by employing product (4.9) in equation (4.6) for τ. By separating the z-dependence from the r-dependence, we obtain

$$\frac{d^2Z}{dz^2} - \lambda^2 Z = 0 \qquad , \tag{4.10}$$

in which λ is a positive real constant to be determined, and

$$\frac{d^2R}{dr^2} + \frac{1}{r}\frac{dR}{dr} - \left(\frac{\lambda^2}{h^2\alpha^2} + \frac{1}{r^2}\right)R = 0 \qquad . \tag{4.11}$$

According to equation (4.10), the solution for $Z(z)$ has the form,

$$Z(z) = A\left[\exp(\lambda z) + B\exp(-\lambda z)\right] \qquad , \tag{4.12}$$

where A and B are constants to be determined. According to equation (4.11) the solution for $R(r)$ is,

$$R(r) = \frac{C}{A}\left[I_1(\lambda r/h\sqrt{\alpha}) + DK_1(\lambda r/h\sqrt{\alpha})\right] \qquad , \tag{4.13}$$

where I_1 and K_1 are modified Bessel functions (of the first and second kinds) of order 1, and C and D are constants to be determined.

With $Z(z)$ and $R(r)$ given by equations (4.12) and (4.13), the shear stress $\tau(r,z)$ is given according to equation (4.9) by the product:

$$\tau(r,z) = C\left[\exp(\lambda z) + B\exp(-\lambda z)\right]\left[I_1(\lambda r/h\sqrt{\alpha}) + DK_1(\lambda r/h\sqrt{\alpha})\right] \qquad . \tag{4.14}$$

Equation (4.14) gives the shear stress $\tau(r,z)$ to within four unknown constants (B, C, D, and λ). The manner in which these constants are determined depends on whether the compact is a solid cylinder (with no core rod), or a hollow cylinder (with core rod surface at $r=a$). We will treat each case separately in sections 4.4 and 4.5.

The average pressure $P(z)$ at any distance z from the bottom face of the compact is calculated according to the integral,

$$\pi(1-a^2)P(z) = 2\pi\int_a^1 p(r,z)\,rdr \qquad . \tag{4.15}$$

This average is of particular interest because it is the quantity that can be approximated by elementary force balance on thin annular slices of the compact. A comparison between $P(z)$ calculated according to equation (4.15) and the elementary expression for $P(z)$ would give an indication of how well the simplest techniques approximate the axial variations of pressure throughout the compact.

Once the shear stress $\tau(r,z)$ is completely determined, the axial pressure $p(r,z)$ and the radial pressure $\sigma(r,z)$ can be determined to within one constant of integration by equations (4.1), (4.2), and (4.3). The constant is fixed by the integral condition,

$$2\pi\int_a^1 p(r,z=1)\,rdr = \pi(1-a^2) \qquad . \tag{4.16}$$

This condition requires that the average dimensionless pressure p applied to the top face of the compact (at z=1) is equal to 1, which in turn guarantees that the average dimensional axial pressure P on the top face is equal to p_o, as it must.

4.3 Equation of State and Mass Balance

The equation of state relates the axial pressure p, the radial pressure σ, and tangential pressure φ in the compact to the corresponding local density. A relatively simple equation of state has the form,

$$\rho = \eta\left[1 + kp_o(p + \sigma + \varphi)\right] \quad , \tag{4.17}$$

where the compressibility k of the powder is the local slope of the variation of ρ with the total pressure (p+σ+φ). The average pressure p_o applied to the upper face of the compact appears because p, σ, and φ are all nondimensionalized by p_o. The compressibility k is itself a decreasing function of density, so that equation (4.17) actually describes a nonlinear relationship between density and total pressure. As ρ increases from the apparent density η of the powder, the compressibility decreases monotonically from its initial value β. Moreover, as ρ approaches its maximum theoretical value M, the local compressibility approaches zero. The simplest relation between k and ρ that satisfies these conditions is

$$k = \beta\left[1 - \frac{\rho - \eta}{M - \eta}\right] \quad . \tag{4.18}$$

By eliminating *k* between equations (4.17) and (4.18), we obtain the following equation of state:

$$\frac{\rho}{\eta} = \frac{(M-\eta) + \beta p_o (1+2\alpha) M p}{(M-\eta) + \beta p_o (1+2\alpha) \eta p} \quad , \tag{4.19}$$

where we have used tangential equilibrium (σ=φ) and constitutive relation (4.3) to eliminate the radial and tangential pressures.

The average density $d(z)$ at any height z is defined by the integral,

$$\pi(1-a^2)d(z) = 2\pi \int_a^1 \rho(r,z) r dr \quad . \tag{4.20}$$

The quantity $d(z)$ is of special interest because it can be determined experimentally by measuring the weight of very thin annular disks that are successively removed from the green compact.

Finally, the balance of mass requires that the mass before compaction be equal to the mass after compaction:

$$\pi(1-a^2)(L/H) = 2\pi \int_0^1 \int_a^1 (\rho/\eta) r dr dz \quad . \tag{4.21}$$

With ρ/η given in terms of $p(r,z)$ by equation (4.19), the balance of mass (4.21) determines the relation between the dimensionless measure βp_o of the applied pressure and the relative compaction height *H*/*L*. This in turn yields the variation of the required compaction load *F* with height *H*.

4.4 Solid Cylindrical Compacts

In the case of solid cylindrical compacts, there is no core rod and $a=0$. Coulomb friction conditions (4.5) and (4.8) at $r=a$ are replaced by the requirement that the stresses remain finite at the centerline ($r=0$) of the cylindrical compact. This in turn implies that the constant *D* must vanish in expressions (4.13) for $R(r)$ and (4.14) for $\tau(r,z)$.

The remaining constants (B, C, and λ) in $\tau(r,z)$ may be determined as follows. First, an alternative expression for $Z(z)$ can be determined by substituting the product (4.9) into the Coulomb friction condition (4.7) at the die wall at $r=1$. In this manner, we obtain,

$$\frac{dZ}{dz} = \mu_o \alpha h \left[1 + \frac{R'(1)}{R(1)} \right] Z \qquad , \tag{4.22}$$

where primes denote differentiation with respect to *r*. The solution for $Z(z)$ is then,

$$Z(z) = Q_o \exp\left\{ \mu_o \alpha h \left[1 + \frac{R'(1)}{R(1)} \right] z \right\} \qquad . \tag{4.23}$$

Equation (4.23) demonstrates that the shear stress is a simple exponential in *z*. We expect generally that at fixed radial distances *r*, the pressures and shear stress will diminish with distance from the top of the compact. Because the *z*-coordinate decreases from 1 at the top surface to 0 at the bottom surface, the sign of the coefficient multiplying z in the exponent of equation (4.23) must be positive. By comparing expressions (4.12) and (4.23) for $Z(z)$, we conclude that $Q_o = A$, $B=0$, and

$$\lambda = \mu_o \alpha h \left[1 + \frac{R'(1)}{R(1)} \right] \quad . \tag{4.24}$$

If equation (4.13) for $R(r)$ (with $D=0$) is employed in equation (4.24), the result is

$$\mu_o \sqrt{\alpha}\, I_o(\lambda / h\sqrt{\alpha}) = I_1(\lambda / h\sqrt{\alpha}) \quad , \tag{4.25}$$

which determines λ as a function of the products $\mu_o\sqrt{\alpha}$ and $h\sqrt{\alpha}$. For prescribed values of these products, equation (4.25) may be solved numerically by Newton-Raphson iteration to determine λ.

With the constants $B=0$ and $D=0$, the product (4.14) for $\tau(r,z)$ reduces to,

$$\tau(r,z) = C \exp(\lambda z)\, I_1(\lambda r / h\sqrt{\alpha}) \quad . \tag{4.26}$$

The corresponding expression for the pressure $p(r,z)$ is obtained by integrating axial equilibrium equation (4.1) with respect to z, integrating radial equilibrium equation (4.2) (with $\sigma = \alpha p$) with respect to r, and ensuring that the two results are consistent. In this manner, we obtain

$$p(r,z) = \frac{C}{\sqrt{\alpha}} \exp(\lambda z)\, I_o(\lambda r / h\sqrt{\alpha}) \quad , \tag{4.27}$$

and

$$\sigma(r,z) = C\sqrt{\alpha}\,\exp(\lambda z)\,I_o(\lambda r/h\sqrt{\alpha}) \quad . \tag{4.28}$$

In order to completely specify the shear stress and the pressures, it remains only to determine the constant of integration *C*.

Constant *C* is determined by integral force balance (4.16). With *p*(*r*,*z*) given by equation (4.27), the integration yields,

$$C = \frac{\lambda e^{-\lambda}}{2hI_1(\lambda/h\sqrt{\alpha})} \quad . \tag{4.29}$$

With *C* determined in this fashion, equations (4.26), (4.27), and (4.28) completely specify the *r*- and *z*-variations of the dimensionless shear stress, axial pressure, and radial pressure throughout a solid cylindrical compact. Each of these quantities is scaled by the as yet undetermined average pressure p_0 applied to the top surface of the compact.

A dimensionless measure βp_o of the average pressure is determined by balance of mass (4.21). With the density ratio ρ/η given by equation of state (4.19), the dimensionless pressure *p*(*r*,*z*) given by equation (4.27), and λ determined by equation (4.25), the balance of mass determines the variation of βp_o with H/L, $h \equiv H/R_o$, μ_o, and α.

If expression (4.27) for *p*(*r*,*z*) is employed in equation of state (4.19) for ρ/η, and the intermediate result is substituted into the balance of mass (4.21), then it is possible to carry out all the z-integrations and some of the r-integrations explicitly. In this manner, we obtain

$$\left[\frac{L}{H}-1\right]=\frac{2}{\lambda}\left[\frac{M}{\eta}-1\right]\int_0^1 \ln\left\{\frac{1+be^{\lambda}I_o(\lambda r/h\sqrt{\alpha})}{1+bI_o(\lambda r/h\sqrt{\alpha})}\right\}rdr \quad , \tag{4.30}$$

in which the constant b is defined in terms of the unknown βp_o by,

$$b\equiv\frac{C\eta(1+2\alpha)\beta p_o}{\sqrt{\alpha}(M-\eta)} \quad . \tag{4.31}$$

For prescribed values of h, H/L, η, M, μ_o, and α, equation (4.30) may be solved by numerical integration and Newton-Raphson iteration to determine b. With b known, the dimensional pressures ($p_o p$ and $p_o\sigma$) and shear stress ($p_o\tau$) are fixed to within a prescribed factor β of compressibility. Finally, and perhaps most importantly, with βp_o and $p(r,z)$ completely determined, the density distribution $\rho(r,z)$ is fixed by equation of state (4.19).

4.5 Hollow Cylindrical Compacts

For hollow cylindrical compacts, Coulomb friction conditions (4.7) and (4.8) apply at r=1 and r=a, respectively. As in the case of solid cylinders, condition (4.7) at r=1 yields exponential solution (4.23) for $Z(z)$. But now, an additional expression for $Z(z)$ can be determined by substituting the product (4.9) into the Coulomb friction condition (4.8) at r=a. In this manner, we obtain,

$$\frac{dZ}{dz} = -\mu_i \alpha h \left[\frac{1}{a} + \frac{R'(a)}{R(a)} \right] Z \qquad , \tag{4.32}$$

with solution,

$$Z(z) = Q_i \exp\left\{ -\mu_i \alpha h \left[\frac{1}{a} + \frac{R'(a)}{R(a)} \right] z \right\} \qquad . \tag{4.33}$$

By comparing the three expressions (4.12), (4.23) and (4.33) for $Z(z)$, we conclude that $Q_o = Q_i = A$, $B=0$, and

$$\lambda = \mu_o \alpha h \left[1 + \frac{R'(1)}{R(1)} \right] \qquad \text{and} \qquad \lambda = -\mu_i \alpha h \left[\frac{1}{a} + \frac{R'(a)}{R(a)} \right] \qquad . \tag{4.34}$$

If equation (4.13) for $R(r)$ is employed in the first of equations (4.34), then the result is

$$D = \frac{\mu_o \sqrt{\alpha} I_o(\lambda / h\sqrt{\alpha}) - I_1(\lambda / h\sqrt{\alpha})}{\mu_o \sqrt{\alpha} K_o(\lambda / h\sqrt{\alpha}) + K_1(\lambda / h\sqrt{\alpha})} \qquad . \tag{4.35}$$

In a similar manner, the second of equations (4.34) yields:

$$D = \frac{\mu_i \sqrt{\alpha} I_o(\lambda a / h\sqrt{\alpha}) + I_1(\lambda a / h\sqrt{\alpha})}{\mu_i \sqrt{\alpha} K_o(\lambda a / h\sqrt{\alpha}) - K_1(\lambda a / h\sqrt{\alpha})} \qquad . \tag{4.36}$$

Equations (4.35) and (4.36) simultaneously determine the dependence of λ and D on $\mu_o\sqrt{\alpha}$, $\mu_i\sqrt{\alpha}$, and a. Solutions are obtained numerically via Newton-Raphson iteration.

With B=0, the product (4.14) for $\tau(r,z)$ reduces to,

$$\tau(r,z) = C\exp(\lambda z)\left[I_1(\lambda r/h\sqrt{\alpha}) + DK_1(\lambda r/h\sqrt{\alpha})\right] \quad . \tag{4.37}$$

The corresponding expression for the pressure $p(r,z)$ is obtained by integrating axial equilibrium equation (4.1) with respect to z, integrating radial equilibrium equation (4.2) (with $\sigma=\alpha p$) with respect to r, and ensuring that the two results are consistent. In this manner, we obtain

$$p(r,z) = \frac{C}{\sqrt{\alpha}}\exp(\lambda z)\left[I_o(\lambda r/h\sqrt{\alpha}) - DK_o(\lambda r/h\sqrt{\alpha})\right] \quad , \tag{4.38}$$

and

$$\sigma(r,z) = C\sqrt{\alpha}\exp(\lambda z)\left[I_o(\lambda r/h\sqrt{\alpha}) - DK_o(\lambda r/h\sqrt{\alpha})\right] \quad . \tag{4.39}$$

With D and λ determined by equations (4.35) and (4.36), the dimensionless shear stress and pressures are known to within a constant C.

Constant C is determined by integral condition (4.16). With $p(r,z)$ given by equation (4.38), the integration yields,

$$2C = \frac{(1-a^2)(\lambda/h)\exp(-\lambda)}{\left[I_1(\lambda/h\sqrt{\alpha}) - aI_1(\lambda a/h\sqrt{\alpha})\right] + D\left[K_1(\lambda/h\sqrt{\alpha}) - aK_1(\lambda a/h\sqrt{\alpha})\right]} \quad . \tag{4.40}$$

With *C* determined in this fashion, equations (4.37), (4.38), and (4.39) completely specify the *r*- and *z*-variations of the dimensionless shear stress, axial pressure, and radial pressure throughout the compact. Each of these quantities is scaled by the as yet undetermined average pressure p_o applied to the top surface of the compact.

A dimensionless measure βp_o of the average pressure is determined by balance of mass (4.21) in a manner similar to that employed for the solid cylinder. With the density ratio ρ/η given by equation of state (4.19), the dimensionless pressure $p(r,z)$ given by equation (4.38), and λ and *D* determined by equations (4.35) and (4.36), the balance of mass determines the variation of βp_o with H/L, $a \equiv R_o/R_i$, $h \equiv H/R_o$, μ_o, μ_i, and α.

If expression (4.38) for $p(r,z)$ is employed in equation of state (4.19) for ρ/η, and the intermediate result is substituted into the balance of mass (4.21), then it is possible to carry out all the *z*-integrations and some of the *r*-integrations explicitly. In this manner, we obtain

$$(1-a^2)\left[\frac{L}{H}-1\right] = \frac{2}{\lambda}\left[\frac{M}{\eta}-1\right]\int_a^1 \ln\left\{\frac{1+be^{\lambda}\left[I_o(\lambda r/h\sqrt{\alpha})-DK_o(\lambda r/h\sqrt{\alpha})\right]}{1+b\left[I_o(\lambda r/h\sqrt{\alpha})-DK_o(\lambda r/h\sqrt{\alpha})\right]}\right\} r\,dr \quad , \quad (4.41)$$

in which the constant *b* is defined in terms of the unknown βp_o by equation (4.31). For prescribed values of *a*, *h*, H/L, η, *M*, μ_o, μ_i, and α, equation (4.41) may be solved by numerical integration and Newton-Raphson iteration to determine *b*. With *b* known, the dimensional pressures ($p_o p$ and $p_o\sigma$) and shear stress ($p_o\tau$) are fixed to within a prescribed factor β of compressibility. Finally, with βp_o and $p(r,z)$ completely determined, the density distribution $\rho(r,z)$ is fixed by equation of state (4.19).

4.6 Results and Discussion

In this section we present results obtained in the manner described above. In all that follows, we take the initial fill aspect ratio L/R_o=10 and the relative apparent density η/M=.45 unless otherwise specified. In the cases that we consider, as compaction proceeds, H/L decreases from 1 to .5. The corresponding aspect ratio $h \equiv H/R_o$ decreases from 10 to 5.

In Figure 4.2, we show the variation of the dimensionless axial pressure $p=p^*/p_o$ with radial location $r=r^*/R_o$, at the top ($z=z^*/H=1$) of the compact, for coefficients of friction $\mu_i=\mu_o$=.75, powder fluidity α=.5, and radii ratio $a=R_i/R_o$=.5. Non-uniformities throughout the compact are caused by the friction between the powder and the core rod, and between the powder and the outer die wall. Because the coefficients of friction are relatively high, the resulting axial and radial non-uniformities are rather severe and are probably greater than those that would be produced in an actual powder compact. In this case, (as indicated on the figure) there is an 18.89% variation in the pressure at z=1 from its minimum value at r=.7 to maximum value at r=1. The pressure is relatively high near the core rod and the die wall in order to balance the friction forces generated there. As guaranteed by integral (4.16), the average value of $p(r,z=1)$ is always equal to 1. Of

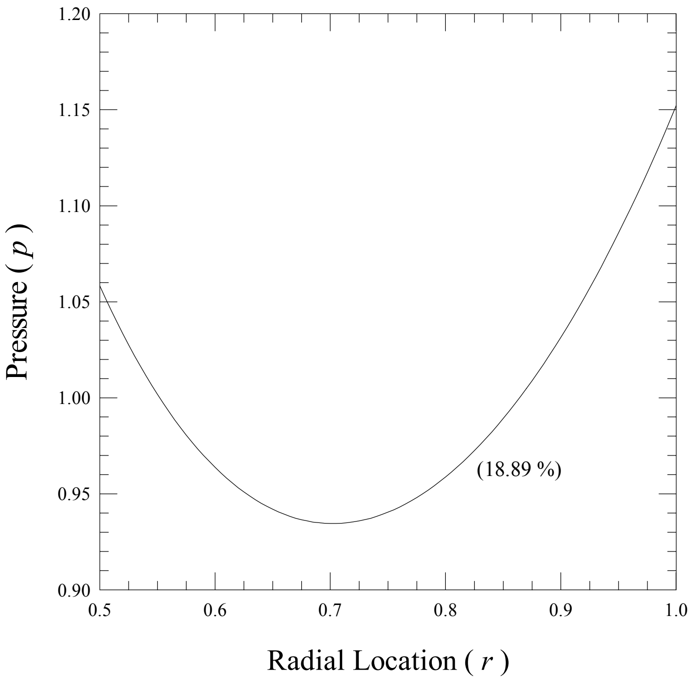

Figure 4.2: The variation of p with r at z=1 for μ_i=μ_o=.75, α=.5, a=.5, L/R_o=10, and η/M=.45. Also shown is the percent variation from minimum to maximum value.

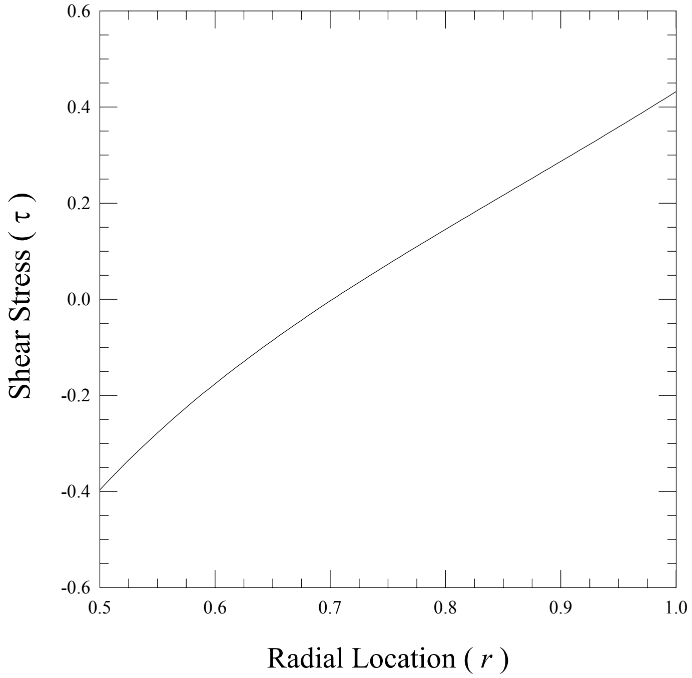

Figure 4.3: The variation of τ with r corresponding to Figure 4.2.

course, the value of p_o and the overall magnitude of the dimensional pressure $p^* \equiv p_o p$ will increase monotonically as H/L decreases from 1.

In Figure 4.3, we show the corresponding variation of shear stress τ. Interestingly, at the top of the compact (z=1), neither the dimensionless pressure nor shear stress varies with H/L, although both contain explicit dependence on $h=(H/L)\times(L/R_o)$. Mathematically, this is because (according to equations (4.37), (4.38), and (4.40)) the quantities $p(z=1)$ and $\tau(z=1)$ depend on both λ and h only through the combination λ/h, which (according to equations (4.35) and (4.36)) is independent of H/L. Physically, this is because $1/\lambda$, which is a characteristic axial length over which the stresses decay, scales with h, which is a measure of the current height of the compact. At axial locations other than z=1, both p and τ do depend on H/L.

In Figure 4.4, we show the corresponding radial variations in relative green density ρ/M at z=1 for a succession of heights H/L=1, .9, .8, .7, and .5. When H/L=1, the compact is not yet compressed, and the density ρ/M has a uniform value equal to the relative apparent density η/M=.45. As compaction occurs, the height $h \equiv H/R_o$ decreases, the densities increase, and nonuniformities develop. On each curve in Figure 4.4, we have indicated the percentage variation in densities from the minimum to the maximum value at each height H/L. Interestingly, the variations in density are considerably smaller than the corresponding variation in the pressure. In the early stages of compaction, the density becomes progressively more nonuniform but in the later stages (H/L<.9) this trend is reversed. The reversal occurs because, according to equation of state (4.19), at

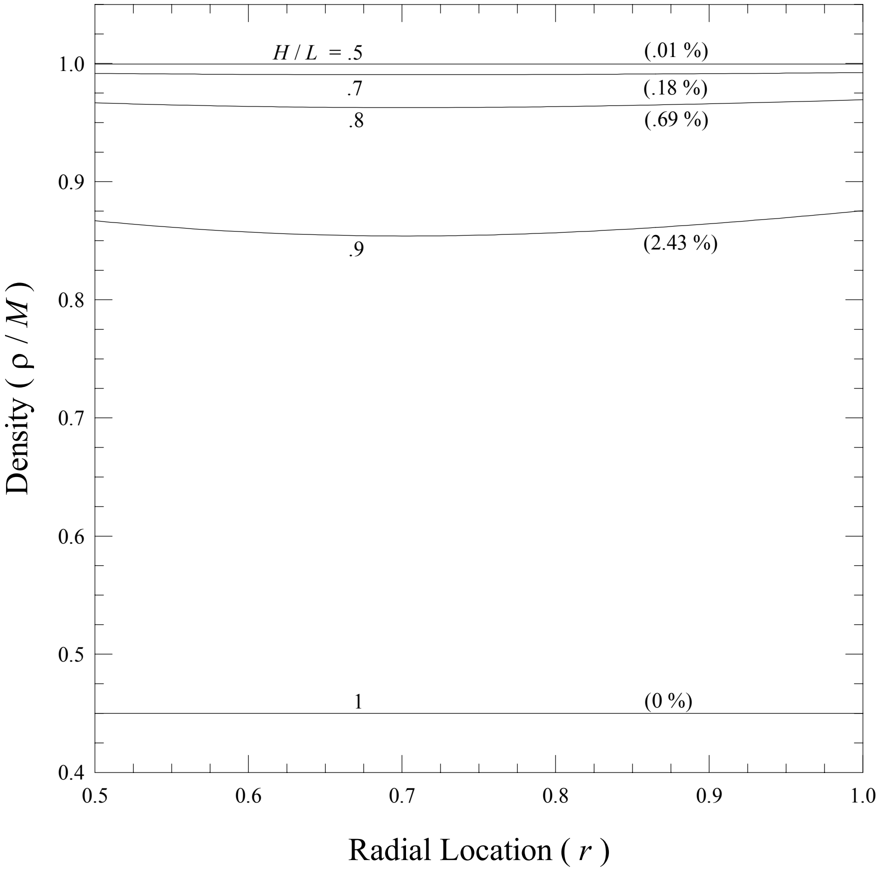

Figure 4.4: The variations of ρ/M with r for H/L=1, .9, .8, .7, .6, and .5 corresponding to Figure 4.2. Also shown are the percent variations from minimum to maximum value.

relatively high pressures equal pressure differences give rise to density differences that decrease with increasing pressure. The profiles in Figure 4.4 are typical in that they demonstrate that the densities vary only slightly in the radial direction. This is true even though the values $\mu_i=\mu_o=.75$ probably overestimate the actual coefficients of friction between the powder and the containing surfaces with which they interact. For this reason, we show no more radial variations, and instead focus on axial variations due to frictional effects, geometry changes, and changes in fluidity.

In order to focus on axial variations of the pressure and the density, we compute the average pressure $P(z)$ and the average density $d(z)$ at any distance z from the bottom of the compact. The quantities $P(z)$ and $d(z)$ are defined by integrals (4.15) and (4.20) respectively. Because the radial variation in density is quite small, we expect that the average density $d(z)$ at any height z does not vary appreciably from the density $\rho(r,z)$ at any radial location r at the same z.

In Figures 4.5 and 4.6, we show axial profiles of the average pressure P and the average density d/M for $\mu_i=\mu_o=0$, .25, .5, and .75 when $\alpha=.25$, $a=.5$, and $H/L=.5$. When the core rod and the die wall are frictionless ($\mu_i=\mu_o=0$), both the pressure and the density are uniform throughout the compact. In fact, the uniform value of the average density ($d/M=.9$) in the frictionless case is equal to the average value of d/M in each non-uniform frictional case. As expected, the axial variations of both the pressure and density increase as the frictional forces at the core rod and die wall increase. As the coefficients of friction μ_i and μ_o increase from .25 to .5 to .75, the top-to-bottom decrease in the pressure increases from 71.6% to 92.2% to 98.1%, while the corresponding top-to-bottom

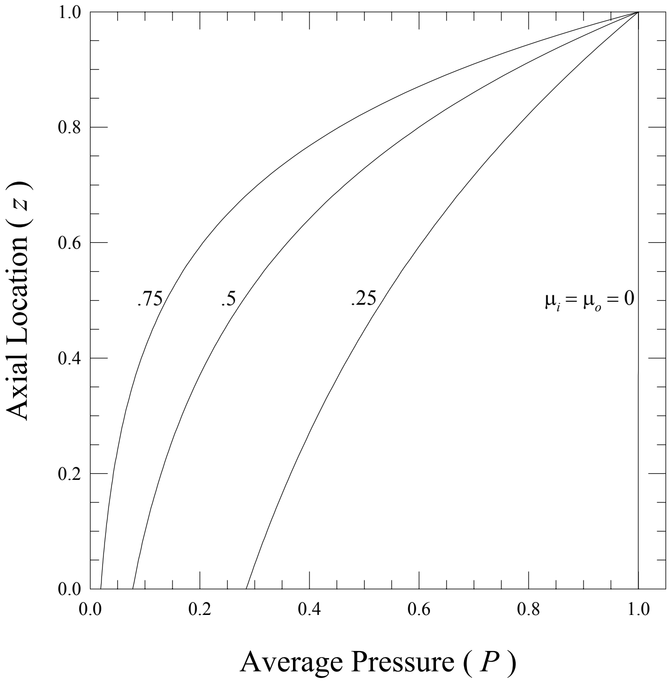

Figure 4.5: The variations of P with z for μ_i=μ_o=0, .25, .5, and .75 when α=.25, a=.5, H/L=.5, h=5, and η/M=.45.

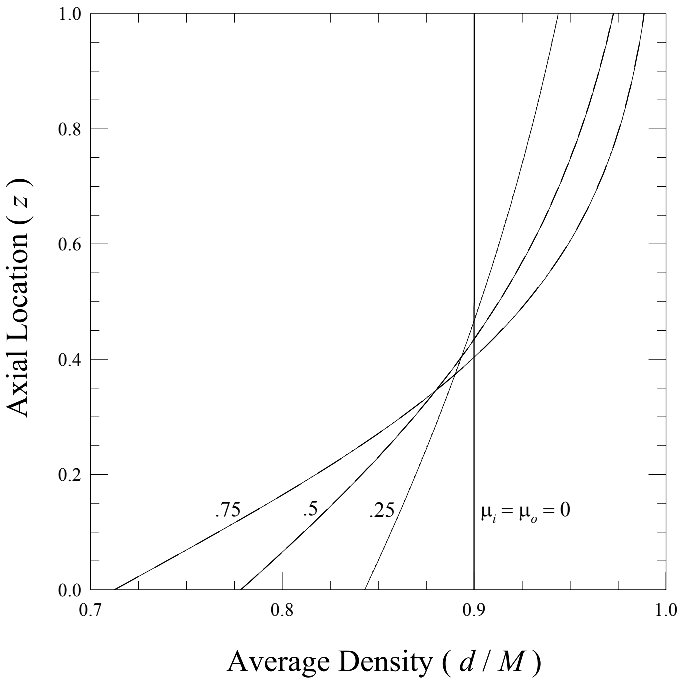

Figure 4.6: The variations of d/M with z corresponding to the four cases shown in Figure 4.5.

decrease in the density increases more modestly from 10.7% to 20.0% to 27.9%. The observation that large variations in pressure yield relatively small variations in density demonstrates the fact (described by the equation of state) that at high pressures the density changes only slightly with relatively large changes in pressure.

In Figures 4.7 and 4.8, we show axial profiles of the average pressure P and the average density d/M for $a \equiv R_i/R_o=0$, .25, .5, and .75 when $\mu_i=\mu_o=.25$, $\alpha=.25$, and $H/L=.5$. For fixed values of the outside radius R_o, as the geometric parameter a increases, the surface area of the core rod increases. This in turn increases the friction forces at the core rod, even though the coefficient of friction between the powder and the core rod remains unchanged. As the friction forces increase, the inhomogeneities in average pressure and average density caused by friction also increase. Consequently, increasing a has the same qualitative effect on the pressure and density variations as does increasing the coefficient of friction at the core rod.

In Figures 4.9 and 4.10, we show axial profiles of the average pressure P and the average density d/M for $\alpha=0$, .25, and .5 when $\mu_i=\mu_o=.25$, $a=.5$, and $H/L=.5$. When $\alpha=0$, no radial pressure is developed, no friction forces are established between the powder and either the die wall or the core rod, and both the pressure and the density are uniform throughout the compact. As α increases, the radial pressures induced by the applied axial pressure also increase. This in turn increases the Coulomb friction forces that develop at the core rod and the die wall. Increasing the friction force increases the axial variations of average pressure and average density in the compact. Consequently, increasing α has

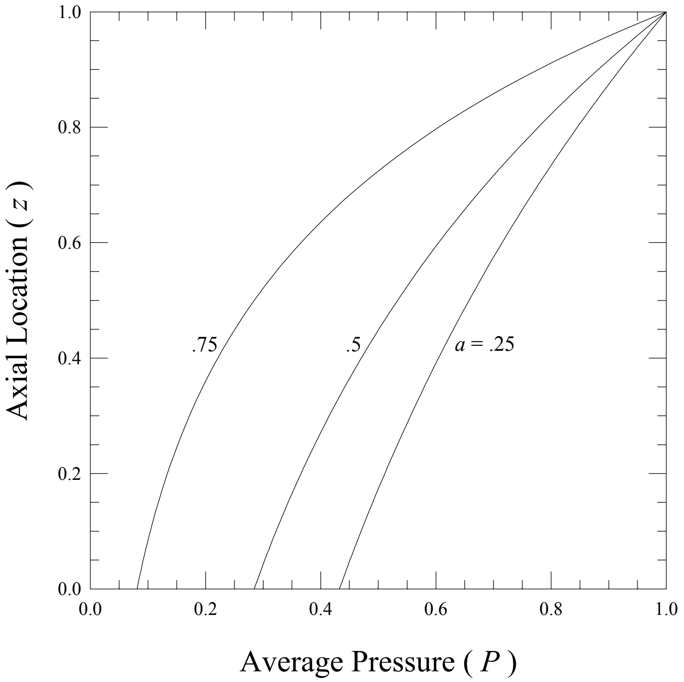

Figure 4.7: The variations of P with z for a=.25, .5, and .75 when $\mu_i=\mu_o$=.25, α=.25, H/L=.5, h=5, and η/M=.45.

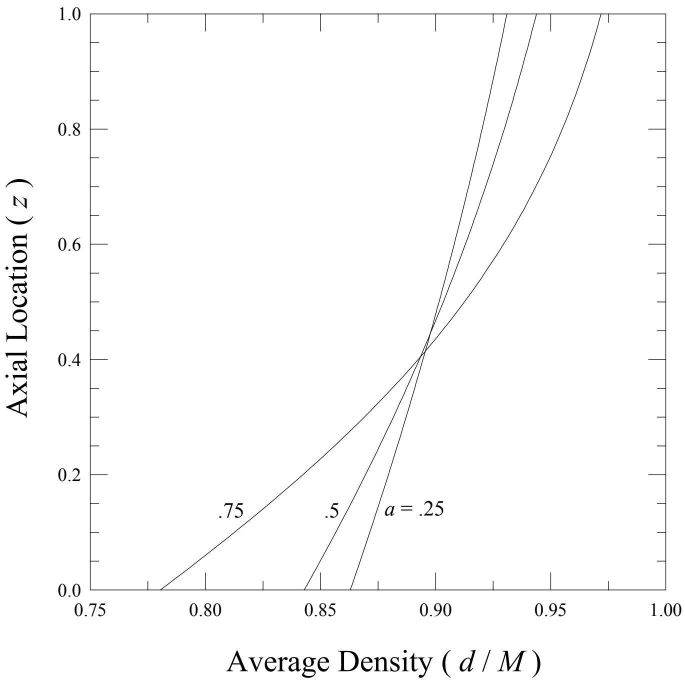

Figure 4.8: The variations of d/M with z corresponding to the three cases shown in Figure 4.7.

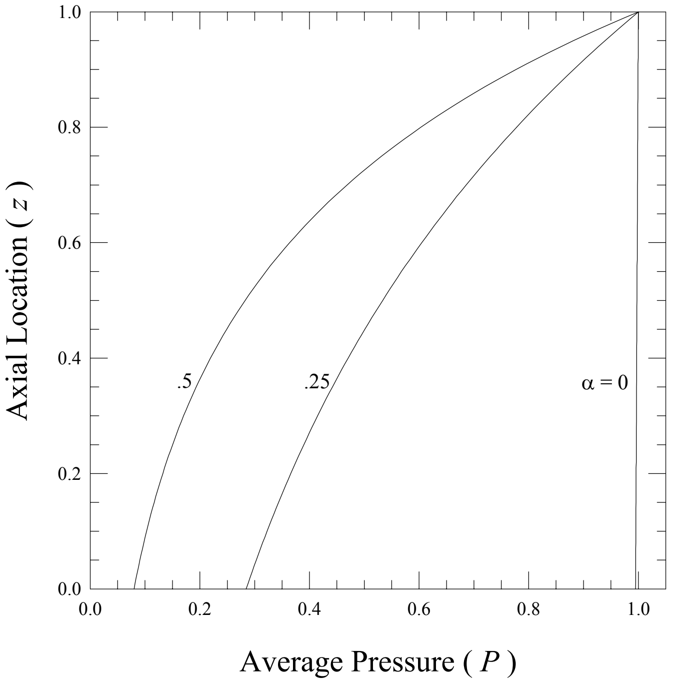

Figure 4.9: The variations of P with z for α=0, .25, and .5 when μ_i=μ_o=.25, a=.5, H/L=.5, h=5, and η/M=.45.

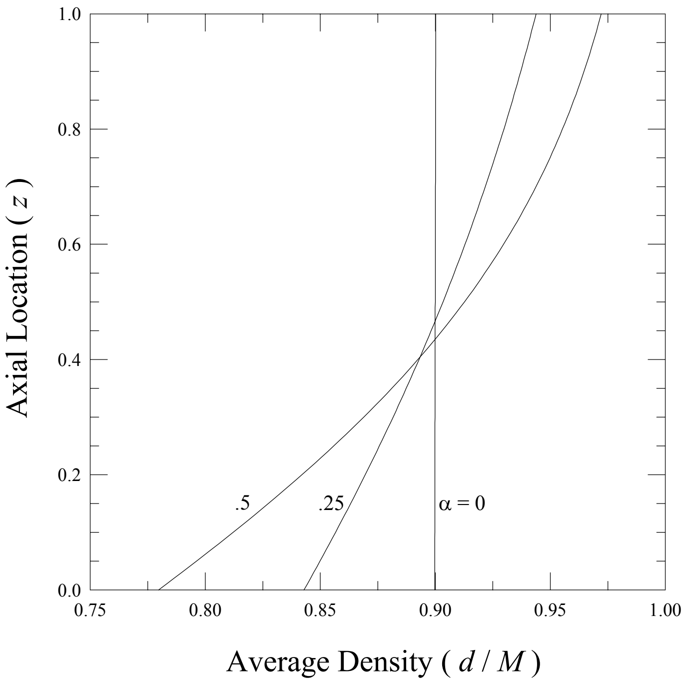

Figure 4.10: The variations of d/M with z corresponding to the three cases shown in Figure 4.9.

the same qualitative effect on the pressure and density variations as does increasing the coefficients of friction at the core rod and die wall.

In Figure 4.11, we show the variations of the dimensionless average applied pressure βp_o with scaled compaction height H/L for $\mu_i=\mu_o=0$, .25, .5, and .75 when $\alpha=.25$ and $a=.5$. As expected, in all cases the required pressure increases as the height of the compact decreases. At first, the pressure increases gradually as the height decreases from $H/L=1$, and increases rapidly as H/L approaches its minimum value (i.e. the value at which the density approaches its maximum). In this case, the minimum value of H/L is equal to $\eta/M=.45$. When $\mu_i=\mu_o=0$, the required pressure is due entirely to the compressive resistance of the powder. As μ_i and μ_o increase from zero, the frictional forces at the core rod and die wall increase, as does the pressure required to overcome them. By comparing the curve for $\mu_i=\mu_o=0$ to the curve for $\mu_i=\mu_o=.25$, we can conclude that even for coefficients of friction as low as .25, a significant fraction of the total applied pressure is required to overcome the friction forces exerted by the die wall and the core rod.

In Figure 4.12, we show the variation of the dimensionless average applied pressure βp_o with compact height H/L for $a=.25$, .5, and .75 when $\mu_i=\mu_o=.25$ and $\alpha=.25$. The dependence of applied pressure on H/L has already been described in Figure 4.11. At any height H/L, the required pressure increases with increasing radii ratio a, even though μ_i and μ_o are the same for each value of a. This is because increasing a corresponds to increasing the surface area of the core rod, which in turn increases the friction force there and the pressure required to balance it.

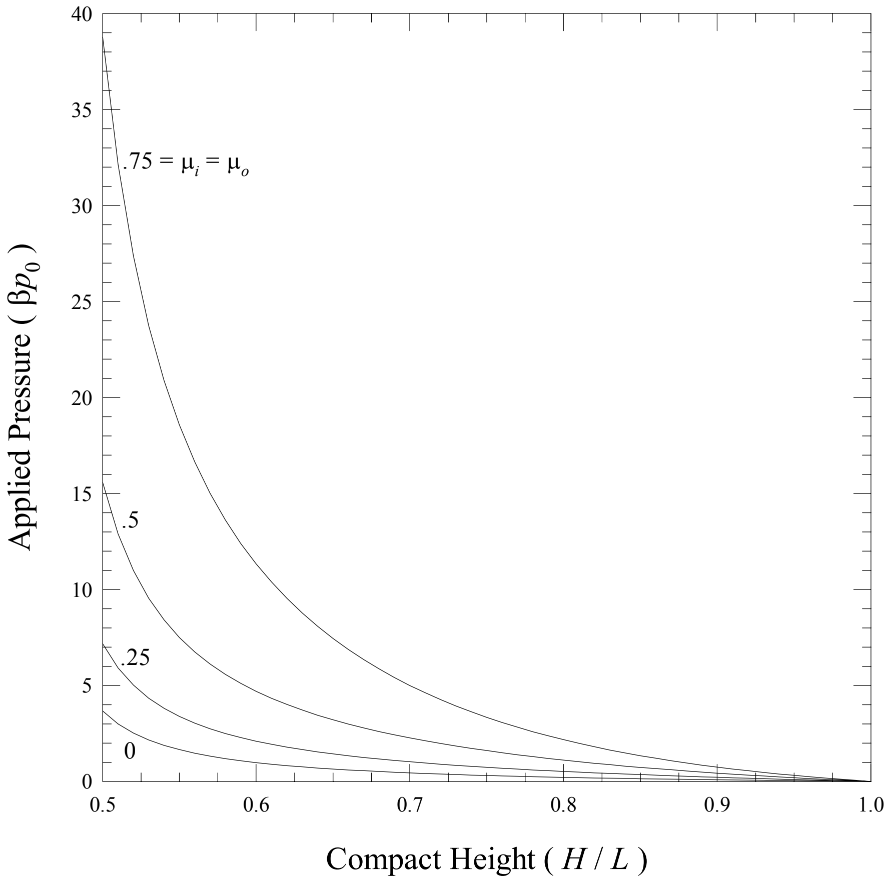

Figure 4.11: The variations of βp_o with H/L for μ_i=μ_o=0, .25, .5, and .75 when α=.25, a=.5, L/R_o=10, and η/M=.45.

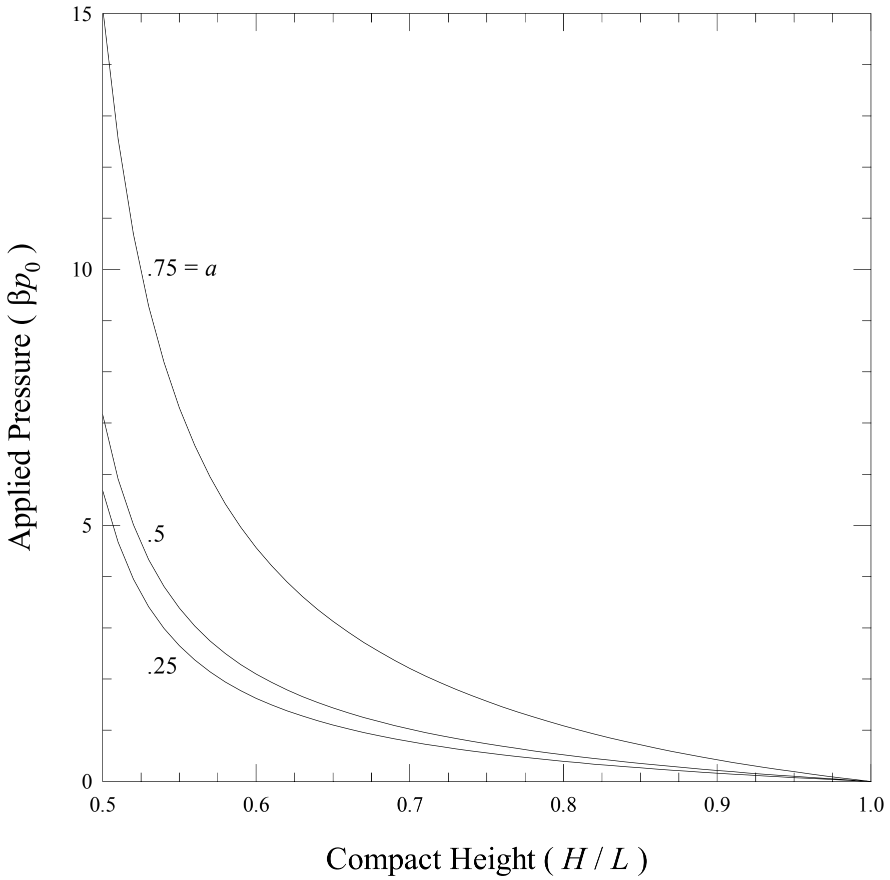

Figure 4.12: The variations of βp_o with H/L for a=.25, .5, and .75 when μ_i=μ_o=.25, α=.25, L/R_o=10, and η/M=.45.

In Figure 4.13, we show the variation of the dimensionless average applied pressure βp_o with compact height H/L for α=0, .25, and .5 when μ_i=μ_o=.25 and a=.5. As fluidity α increases, the radial pressure and the induced friction forces at the core rod and the die wall also increase. Consequently, for fixed compaction heights H/L, the effect of increasing α on the required compaction pressure is qualitatively similar to that of increasing the coefficients of friction μ_i and μ_o.

Rather than detailed density profiles, in Figure 4.14, we show the variation of average density d/M with aspect ratio $h \equiv H/R_o$ at five distinct axial locations (z=0, .25, .5, .75, and 1) when μ_i=μ_o=.25, α=.1, a=.5, and H/L=.5. For a fixed value of outside radius R_o, as the compact becomes taller, the surface areas of the core rod and the die wall get larger, and the total friction between the powder and its containing surfaces increases. Therefore, as h increases, the average density varies more widely between the top (z=1) and bottom (z=0) of the compact.

The percent top-to-bottom density decrease measures the drop in average density (from z=1 to z=0) relative to the density at z=1. This percent decrease is a quantitative measure of nonuniformity in a powder metal compact. In Figures 4.15, 4.16, and 4.17, we show how the percent top-to-bottom density decrease varies with aspect ratio $h \equiv H/R_o$. In Figure 4.15, for example, we consider three pairs of friction coefficients (μ_i=μ_o=.25, .5, and .75) for fixed values α=.1, a=.5, and H/L=.5. In Figure 4.16, we consider three values of the geometric parameter a (a=.25, .5, and .75) for fixed values μ_i=μ_o=.25, α=.1, and H/L=.5; and in Figure 4.17, we consider three values of fluidity α (α=.1, .3, and .5)

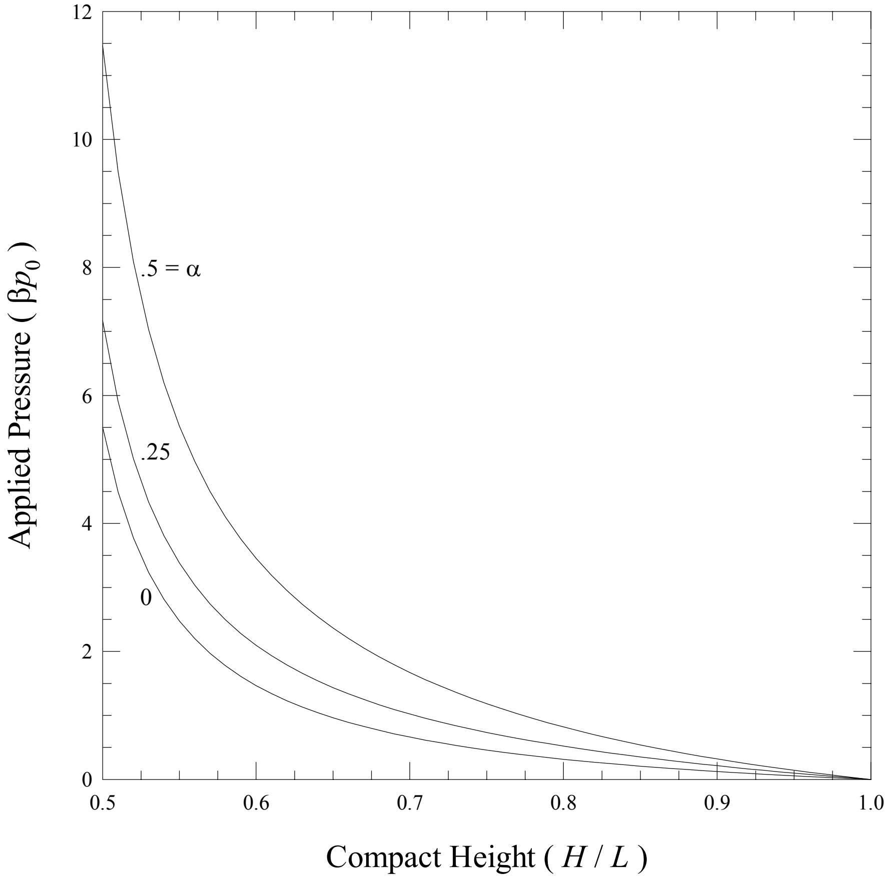

Figure 4.13: The variations of βp_o with H/L for α=0, .25, and .5 when μ_i=μ_o=.25, a=.5, L/R_o=10, and η/M=.45.

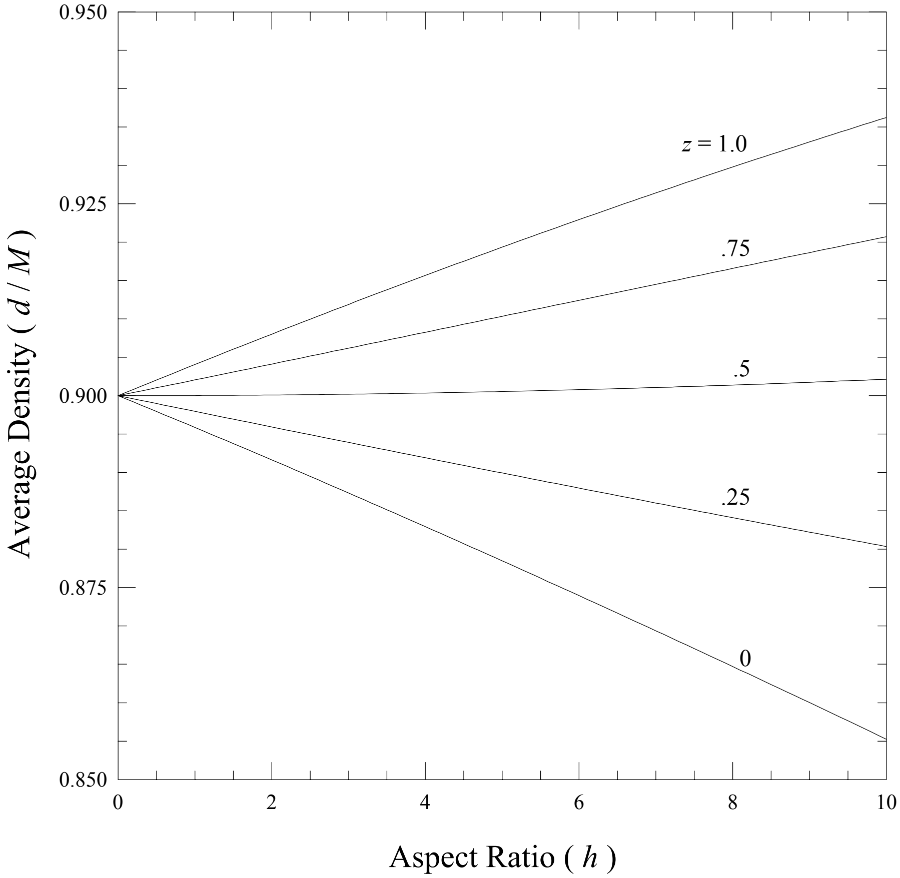

Figure 4.14: The variations of d/M with h for z=0, .25, .5, .75, and 1 when $\mu_i=\mu_o=.25$, $\alpha=.1$, $a=.5$, $H/L=.5$, and $\eta/M=.45$.

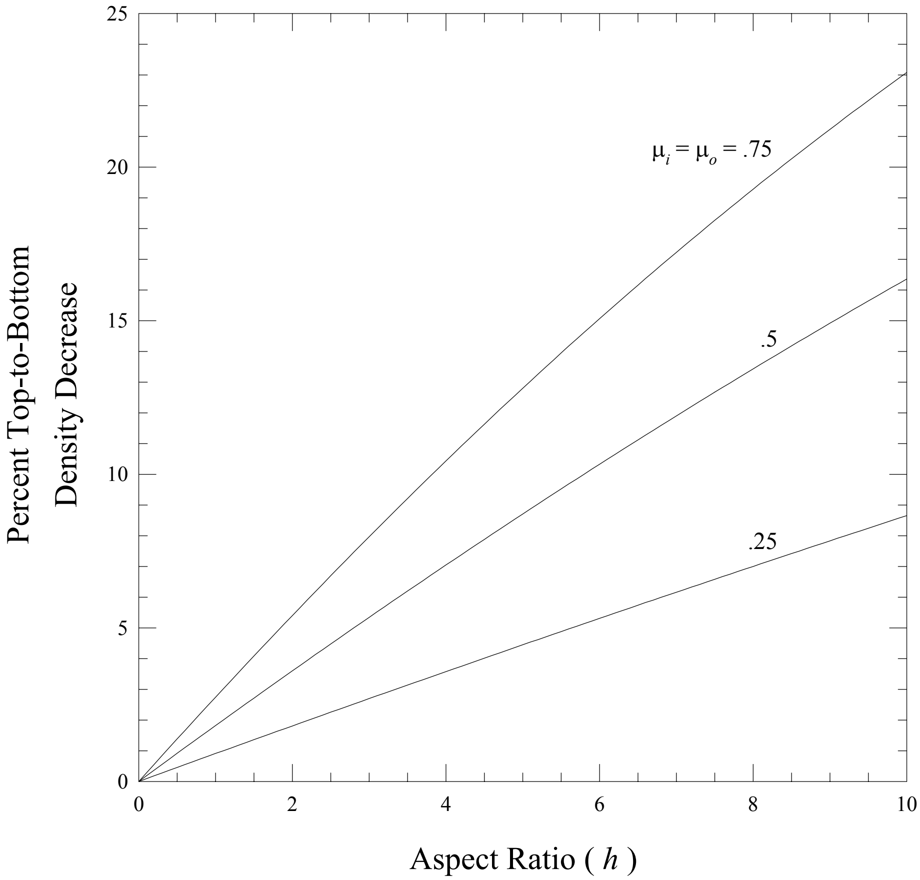

Figure 4.15: The variations of percent top-to-bottom density decrease with h for $\mu_i=\mu_o=.25$, .5, and .75 when $\alpha=.1$, $a=.5$, $H/L=.5$, and $\eta/M=.45$.

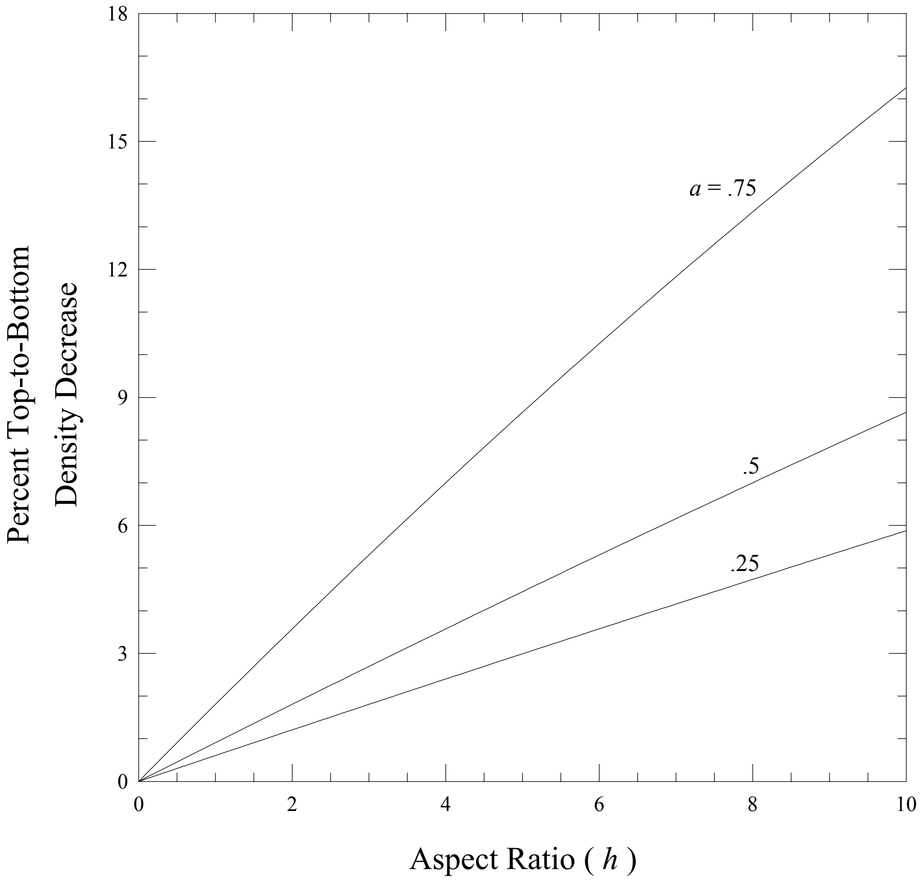

Figure 4.16: The variations of percent top-to-bottom density decrease with *h* for *a*=.25, .5, and .75 when $\mu_i=\mu_o=.25$, $\alpha=.1$, $H/L=.5$, and $\eta/M=.45$.

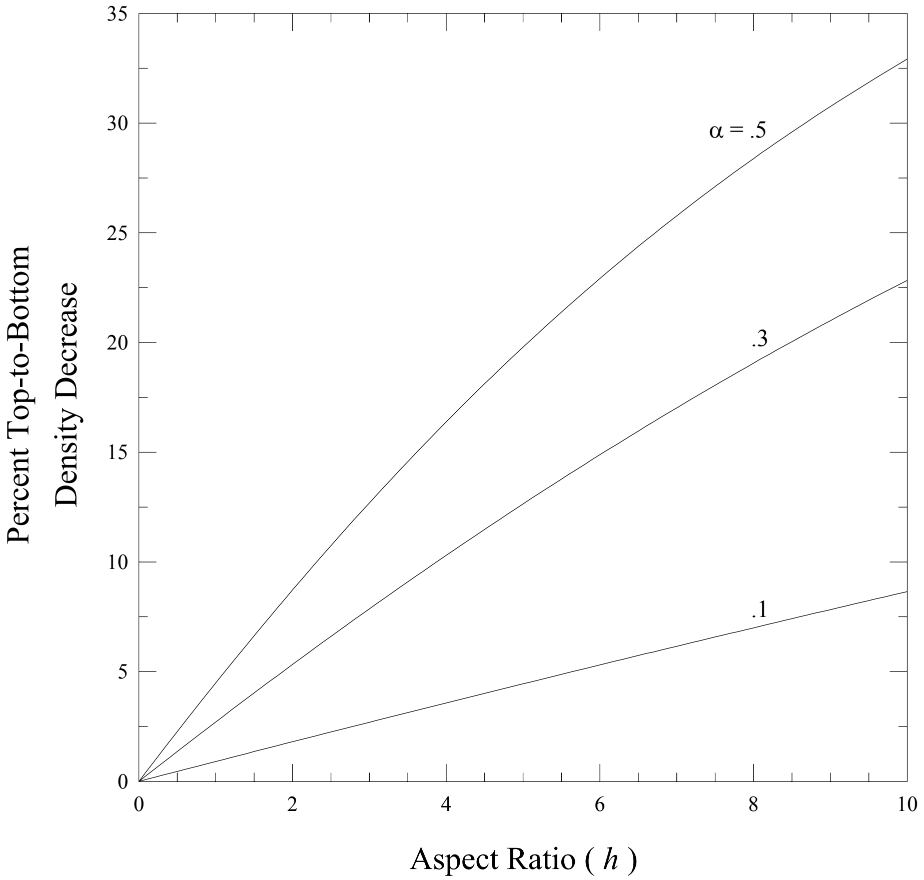

Figure 4.17: The variations of percent top-to-bottom density decrease with *h* for α=.1, .3, and .5 when μ_i=μ_o=.25, *a*=.5, *H*/*L*=.5, and η/*M*=.45.

for fixed values μ_i=μ_o=.25, *a*=.5, and *H*/*L*=.5. As expected, in all cases, the variation of density throughout the compact increases with increasing aspect ratio. Moreover, for fixed values of aspect ratio, the net influence of friction and therefore the density variations also increase with increasing μ_i=μ_o, *a*, or α.

Thus far, we have focused on cases in which the coefficients of friction at the core rod and the die wall have been equal. This obscures an inherent asymmetry with respect to the separate effects of μ_i and μ_o. In Figure 4.18, for example, we fix the coefficient of friction of the die wall (at μ_o=.25) and show how the percent top-to-bottom density decrease varies with the coefficient of friction of the core rod μ_i for *a*=.01, .25, .5, and .75 when α=.25 and *H*/*L*=.5. In general, the density variation increases with increasing μ_i, as expected. For a fixed value of outside radius R_o, when *a* is small (i.e. *a*=.01), the surface area of the core rod is small, and increasing μ_i therefore has almost no effect on the density variation throughout the compact. As *a* increases, the surface area of the core rod increases, and the degree to which μ_i effects the density variation increases as well.

By contrast, in Figure 4.19, we fix the coefficient of friction of the core rod (at μ_i=.25) and show how the percent top-to-bottom density decrease varies with the coefficient of friction of the die wall μ_o for *a*=.01, .25, .5, and .75 when α=.25 and *H*/*L*=.5. In this case, even when *a* is small, the surface area of the die wall is large. Consequently, the density variation increases rapidly as μ_o increases. As *a* increases, so too does the surface area of the core rod and the friction force developed there. This causes the density variation to increase as well. However, the degree to which μ_o effects

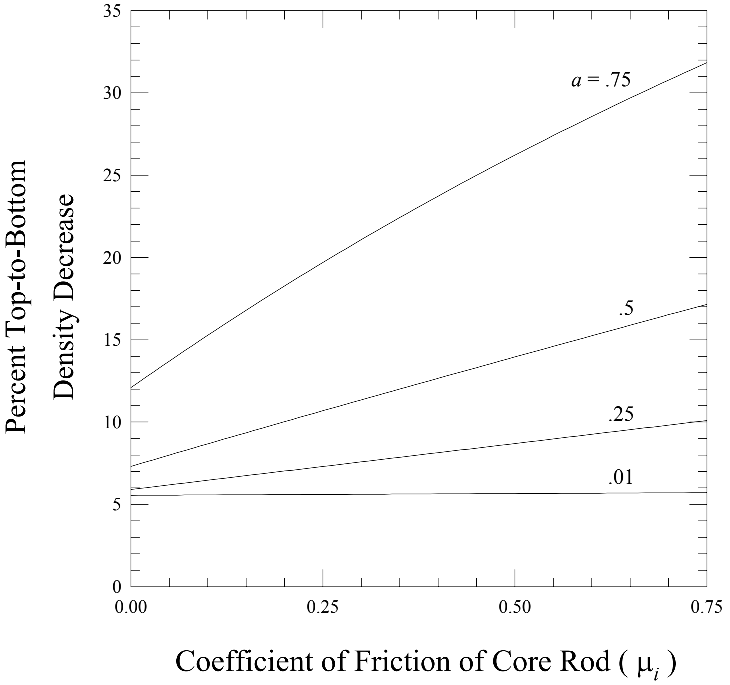

Figure 4.18: The variations of percent top-to-bottom density decrease with μ_i for a=.01, .25, .5, and .75 when μ_o=.25, α=.25, H/L=.5, L/R_o=10, and η/M=.45.

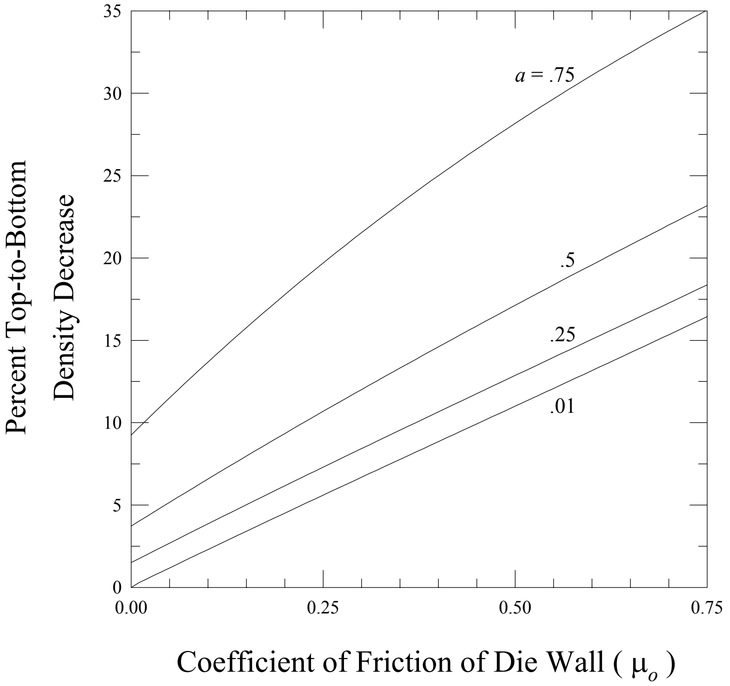

Figure 4.19: The variations of percent top-to-bottom density decrease with μ_o for a=.01, .25, .5, and .75 when μ_i=.25, α=.25, H/L=.5, L/R_o=10, and η/M=.45.

the density variation does not change appreciably as a increases, because the outside radius of the compact is fixed.

To verify the validity of the model developed in this chapter, we must compare our theoretical predictions with data obtained by experiment. Trasorras and Parameswaran [1999] experimentally constructed axial density profiles for two identical valve guides made by the double punch compaction of an iron powder, Distalloy AE, supplied by Hoganas. A valve guide is a hollow cylindrical part used in internal combustion engines to guide the movement of intake and exhaust poppet valves. The apparent density η of the powder is 3.04 g/cm^3. The maximum density M reported by Pavier and Doremus [1999] for Distalloy AE is 7.33 g/cm^3. The average density in each valve guide was 6.80 g/cm^3. The initial fill height L of the iron powder can be calculated according to $L=(6.80/3.04)H$. The compacted valve guide had a height H of 4.05 in (=102.87 mm), an inside radius R_i of .152 in (=3.861 mm), and an outside radius R_o of .375 in (=9.525 mm). With these parameters specified, the relative apparent density of the powder η/M is equal to .415, the geometric parameter $a \equiv R_i/R_o$ is equal to .405, the relative compaction height H/L is equal to 3.04/6.8=.447, and the initial fill aspect ratio L/R_o is equal to $(H/R_o)/(H/L)=12.08$.

The axial density profiles were constructed by successively machining annular disks of known thickness away from the valve guide, and by weighing the remaining part after each machining operation. In this manner, the mass and density of each removed disk was determined. Calculated in this manner, the density is actually an average of the point-to-point density that varies radially in the removed disks. This density is precisely the average density $d(z)$ defined by equation (4.20) that our model can predict.

The valve guide used by Trasorras and Parameswaran [1999] was produced by double punch compaction. To compare our theoretical results for single punch compaction to their experimental results, we approximate the double punch compaction as two simultaneous single punch compactions. In doing so, we interpret the axial density variation from the midplane to the top of the compact and from the midplane to the bottom of the compact as two separate profiles that might result from the single punch compaction of a part that is half the height of the parts produced by Trasorras and Parameswaran [1999]. In Figure 4.20, we show the experimental profile of average density d for the top half of the first valve guide. Here $z^*=0$ corresponds to the center of the valve guide and $z^*=51.435$ mm corresponds to its top surface. The corresponding profile for the bottom half of the first valve guide is shown in Figure 4.21, in which $z^*=0$ identifies the center of the valve guide and $z^*=51.435$ mm identifies its bottom surface. In Figure 4.22 and 4.23, we show the axial density profiles corresponding to the top and bottom halves of the second valve guide, respectively. In these four profiles, the density decreases by an average of 9.7%.

In constructing the profiles shown in Figures 4.20, 4.21, 4.22, and 4.23, Trasorras and Parameswaran [1999] machined slices that were .1 mm thick within 3 mm of the top or bottom of the compact, .5 mm thick between 3 mm and 13 mm of the top or bottom, and 2 mm thick beyond 13 mm of the top or bottom. In presenting the experimental results, we have omitted the wide fluctuations in density that were measured within the

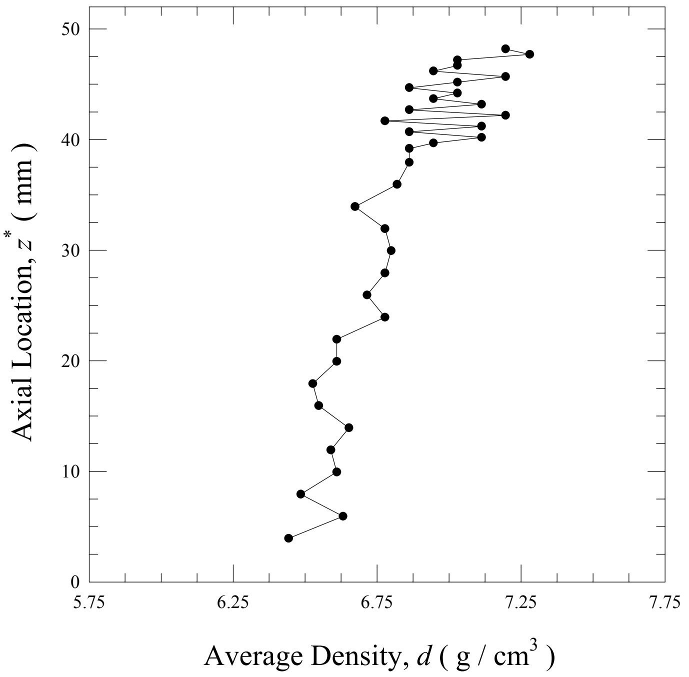

Figure 4.20: The variation of d with z^* for the top half of the first valve guide used in the experiment by Trasorras and Parameswaran [1999].

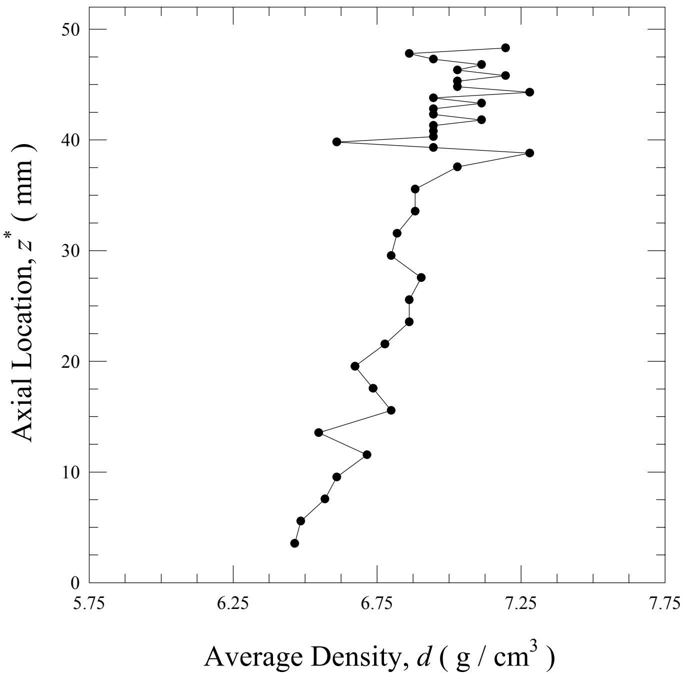

Figure 4.21: The variation of d with z^* for the bottom half of the first valve guide used in the experiment by Trasorras and Parameswaran [1999].

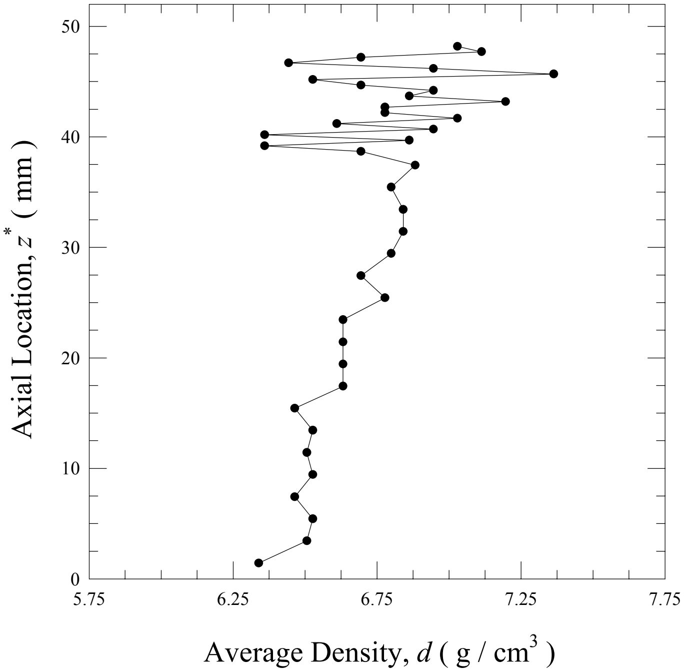

Figure 4.22: The variation of d with z^* for the top half of the second valve guide used in the experiment by Trasorras and Parameswaran [1999].

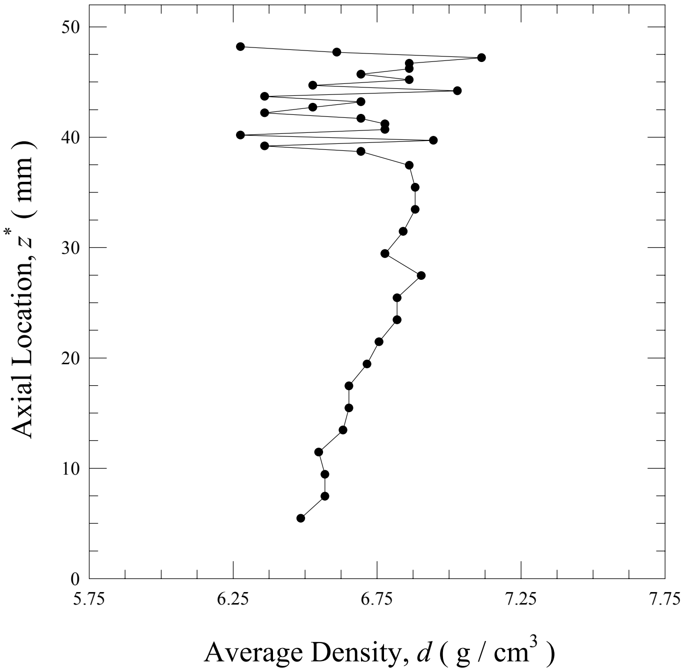

Figure 4.23: The variation of d with z^* for the bottom half of the second valve guide used in the experiment by Trasorras and Parameswaran [1999].

first 3 mm of the top or bottom surfaces of the compacts. It is possible that these fluctuations in density are due to small errors in the measured thickness (and volume) of the slices. Even with the widest fluctuations removed, there is still considerable scatter in the experimental data where the slices are .5 mm thick, and there is much less fluctuation where the slices are 2 mm thick.

To compare theoretical density profiles to those obtained by experiment, we need to know the values of μ_i, μ_o, and α. These values are not known for the experiment, but if we assume that μ_i is equal to μ_o, then we can infer the values of μ_i, μ_o, and α based on our observation that the top-to-bottom density decrease is 9.7%. In Figure 4.24, for example, we show how the percent top-to-bottom density decrease varies with coefficients of friction μ_i=μ_o for α=.1, .2, .3, and .5 when the parameters a=.405, H/L=.447, L/R_o=12.080, and η/M=.415 are chosen match the experimental conditions. As expected, the variation in density increases as μ_i=μ_o and α increase. Figure 4.24 demonstrates that there is a range combinations of μ_i=μ_o and α that yield a fixed density variation. To show these combinations explicitly, in Figure 4.25 we show the locus of points in the α-μ_i=μ_o plane that yield four top-to-bottom density variations (2%, 5%, 9.7%, 15%) when a=.405, H/L=.447, L/R_o=12.080, and η/M=.415.

Finally, we focus on the darkened solid curve in Figure 4.25 corresponding to a density variation of 9.7%. In particular, we consider three points that lie on the curve: α=.25 and μ_i=μ_o=.423, α=.5 and μ_i=μ_o=.213, and μ_i=μ_o=.75 and α=.139. In Figure 4.26 we plot the density profile that corresponds to each point. It turns out that not only do these three profiles have the same overall density variation of 9.7%, as they must, but the

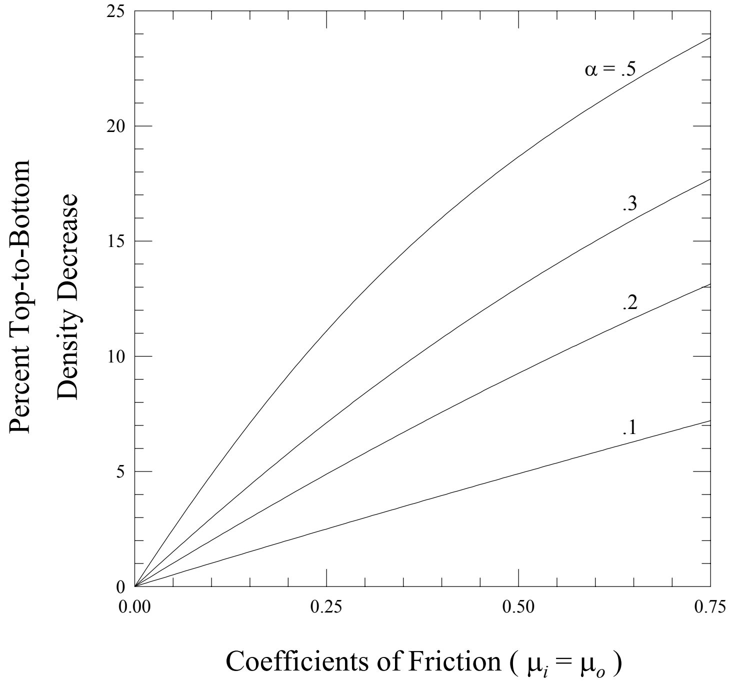

Figure 4.24: The variations of percent top-to-bottom density decrease with $\mu_i = \mu_o$ for α =.1, .2, .3, and .5 when a=.405, H/L=.447, L/R_o=12.08, and η/M=.415.

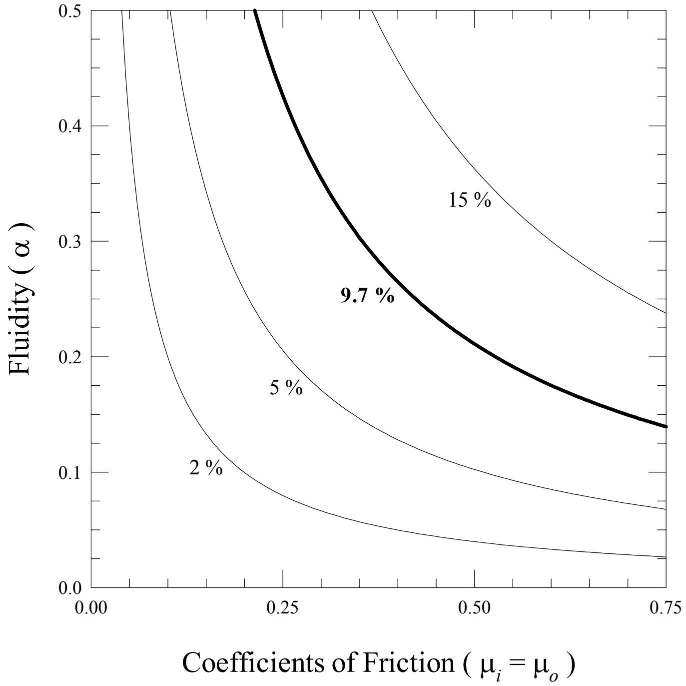

Figure 4.25: The variations of α with $\mu_i = \mu_o$ for density variations of 2%, 5%, 9.7%, and 15% when a=.405, H/L=.447, L/R_o=12.08, and η/M=.415.

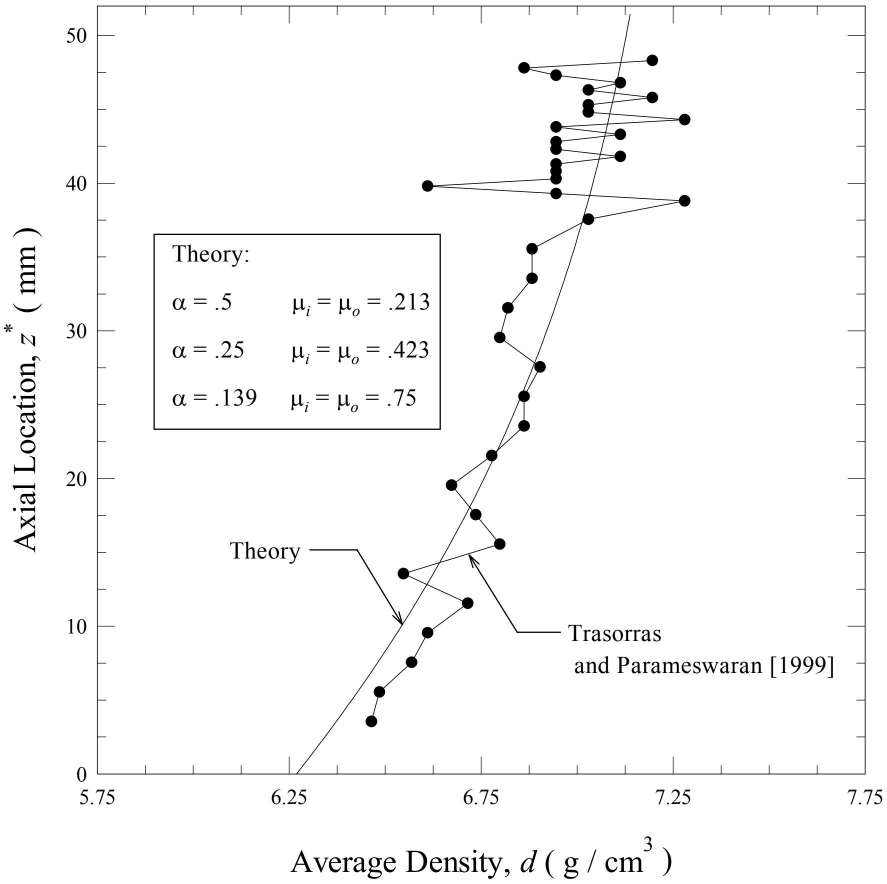

Figure 4.26: The variation of d with z^* for α=.5 and μ_o=μ_i=.213, α=.25 and μ_o=μ_i=.423, and α=.139 and μ_o=μ_i=.75 when a=.405, H/L=.447, L/R_o=12.08, and η/M=.415. The three combinations of μ_i=μ_o and α are chosen to yield a 9.7% top-to-bottom density decrease. Superposed is the experimental data from Trasorras and Parameswaran [1999] shown in Figure 4.21.

details of the profiles are indistinguishable. We have also superposed the density profile experimentally determined by Trasorras and Parameswaran [1999] shown in Figure 4.21. For the appropriate choice of $\mu_i=\mu_o$ and α, there is excellent agreement between theory and experiment.

CHAPTER 5

Conclusion

The focus of this thesis was on developing relatively simple models for powder compaction in order to clarify the physical mechanisms that govern the process, and to study the effects of fill conditions on the final green state. In Chapter 2, we focused on the effects of varying powder properties on pressure distributions, density distributions, and radial movements of powder in cylindrical dies. We isolated the effects of dissimilar powder properties by neglecting the influence of die wall friction. In this manner, any pressure and density variations in the green compact were necessarily due to initial fill variations. We focused specifically on radial variations of the powder properties, and employed a simple model in which the cylinder is initially filled with *n* distinct powders, each of which occupies successive annular regions about the centerline of the cylinder. The powders were distinguished by their compressibilities, their fluidities, and their apparent densities.

Of special interest were two sub cases of the *n*-powder model. In the first case, we set *n*=2 in order to study the compaction behavior of two-powder parts. Here, the dies were initially filled with an inner powder at the core of the cylinder and an outer powder that occupies the remaining annular region of the cylinder. For prescribed values of the properties of each powder, we computed the inward or outward radial movement of the interface that separates the powder, the fraction of the total compaction load that is supported by each powder, and the final densities of the powders. The interface movement, and how it depended on the mismatch in properties of the two powders provided insights into how local nonuniformities in powders properties produce corresponding inhomogeneities in green densities.

In the second case, we set *n* equal to twenty, to approximate a single powder with properties that vary continuously in the radial direction. Following (by analogy) the two-powder cases, when the properties of all twenty powders were specified, we computed the pressures and densities in each powder, and in this manner we constructed the pressure and density profiles throughout the green compact.

In Chapter 3, we developed a model for a single powder with continuously varying powder properties, and demonstrated how it could be obtained by taking the appropriate limit of the discrete powder model developed in Chapter 2. We employed this model to study the effects of initial nonuniformities by prescribing initial radial variations of compressibility, fluidity, and apparent density and by predicting the final density and pressure distributions in the green compact. The radial variations represent uneven fill conditions, and the nonuniformities in green density were due entirely to these undesirable but unavoidable pre-compaction conditions. Perhaps of greatest interest were solutions to the inverse problem, in which, we calculated a variety of initially nonuniform fill states that guarantee perfectly uniform green densities. These pre-compaction states were typically characterized by combinations of radially varying compressibilities, fluidities, and apparent densities that were calculated to exactly balance one another in the final state.

In Chapter 4, we included the effects of friction between the powder and the outer die wall, and between the powder and the inner core rod to compute the final pressure and density distributions of parts pressed in hollow cylindrical dies. The hollow cylindrical geometry is of practical importance in the production of such parts as bushings and valve guides.

Our primary focus was on the forward problem, in which the pre-compaction fill was perfectly uniform and the densities became distorted during compaction. We predicted how the pressures and green densities depend on the coefficient of friction between the die wall and the powder, the coefficient of friction between the core rod and the powder, the ratio of the inside radius of the green part to its outside radius, the compressibility of the powder, the fluidity of the powder, and the aspect ratio of the green compact.

Our secondary focus was on comparing the results predicted by the model to the experimental results of Trasorras and Parameswaran [1999]. In order to make the comparison, we matched the percent top-to-bottom density variations in the experiments to those predicted by the theory. In this manner, we could infer possible values for the coefficients of friction and fluidity, which were not measured. For those parameters that give agreement between the experimental and theoretical top-to-bottom density variations, the details of the axial variations in density predicted by the theory agreed remarkably well with those obtained experimentally.

In Chapter 4, we restricted our attention to uniform initial fill densities. In practice, because of uneven powder flow into the die, shadow effects from the core rod, and imperfect feed shoe mechanisms, the pre-compaction density (η) could vary in the radial (r), axial (z), and tangential (θ) directions. Incorporating the dependence of η on r and z is straightforward and would involve little modification to the model. Incorporating θ-dependence is more complex, because the fundamental equilibrium equations were based on rotational symmetry. Without rotational symmetry, the model developed in Chapter 4 would have no closed-form solution. A solution could only be obtained by implementing an elaborate finite element scheme.

In the context of hollow cylindrical dies with friction, it would also be of interest to study inverse problems, in which variations of initial density are computed in such a way to guarantee perfectly uniform green densities. Given the distortive effects of friction in the powder compaction process, it may be entirely possible that such solutions do not exist, or that such solutions contain impractically large variations in fill densities. In these cases, it would be possible to solve for variations of initial density that yield a minimum variation in the green density.

The coefficients of friction at the core rod and the die wall were assumed to be constant in Chapter 4. In practice, the manner in which powder particles interact with the core rod and the die wall will change fundamentally as the density of the powder increases. To account for these effects, it would be necessary to model the coefficients of friction at the die wall and the core rod as functions of density.

For simplicity, we have also assumed that fluidity is constant in all our compaction models. However, the degree to which the applied pressure induces a corresponding radial pressure will vary according to the density of the powder. In fact, the fluidity α is an increasing function of density whose value approaches unity as the density approaches it theoretical maximum. A more elaborate model would incorporate this complication as well.

REFERENCES

Aydin, I., Briscoe, B.J., Ozkan, N., (1997). Modeling of Powder Compaction: A Review. MRS Bulletin, Vol. 22, No. 12, pp. 45-51.

Chtourou, H., Gakwaya, A., Guillot, M., (1996). Assessment of the Predictive Capabilities of the Cap Material Model for Simulating Powder Compaction Problems. Advances in Powder Metallurgy & Particulate Materials-1996, Vol. 1, Part 7, Metal Powder Industries Federation, pp. 245-255.

Cooper, A.R., Eaton. L.E., (1962). Compaction Behavior of Several Ceramic Powders. Journal of the American Ceramic Society, Vol. 45, pp. 97-101.

Crawford, J., Lindskog, P., (1983). Constitutive Equations and Their Role in the Modeling of the Cold Pressing Process. Scandinavian Journal of Metallurgy, Vol. 12, pp. 271-281.

Duwez, P., Zwell, L., (1949). Pressure Distribution in Compacting Metal Powders. Arch. Eisenhuttenw., Vol. 18 [Nov.-Dec.], pp. 137-144.

Fleck, N.A., Kuhn, L.T., McMeeking, R.M., (1992). Yielding of Metal Powder Bonded by Isolated Contacts. Journal of the Mechanics and Physics of Solids, Vol. 40, pp. 1139-1162.

German, R., (1994). Powder Metallurgy Science, 2nd edition, Metal Powder Industries Federation, Princeton, New Jersey.

Gethin, D.T., Lewis, R.W., Ariffin, A.K., (1995). Modeling Compaction and Ejection Processes in the Generation of Green Powder Compacts. Net Shape Processing of Powder Materials, 1995 ASME Int. Congress and Exposition, AMD-Vol. 216, S. Krishnaswami, R.M. McMeeking, and J.R.L. Trasorras, Editors, ASME, pp. 27-45.

Janssen, H.A., (1895). Z. Ver. Deutsch. Ing., Vol. 39, p. 1045.

Krishnaswami, K., Trasorras, J.R.L., (1995). Modeling the Compaction of Metallic Powders with Ductile Particles. Simulation of Materials Processing: Theory, Methods, and Application, Shen and Dawson, Editors, Balkerma, Rotterdam, pp. 863-858.

Morimoto, Y., Hayashi, T., Takei, T., (1982). Mechanical Behavior of Powders in a Mold with Variable Cross Sections. International Journal of Powder Metallurgy and Powder Technology, Vol. 18, No. 1, pp. 129-145.

Mroz, Z., Zeinkiewicz, O.C., (1984). Mechanics of Engineering Materials, C.S. Desai and R.H. Gallagher, Editors, John Wiley and Sons, New York, p. 415.

Pavier, E., Doremus, P., (1999). Mechanical Behavior of Lubricated Iron Powder. Institute National Polytechnique de Grenoble, France.

Shima, S., (1975). A Study of Forming of Metal Powders and Porous Metals. Ph.D. Thesis, Kyoto University.

Thompson, R.A., (1982). Mechanics of Powder Pressing. Ceramic Bulletin, Vol. 60, No. 2, pp. 237-243.

Thummler, F., Oberacker, R., (1993). Introduction to Powder Metallurgy. Institute of Materials, Cambridge, Great Britain.

Trasorras, J.R.L., Krauss, T.M., Ferguson, B.L., (1989). Modeling of Powder Compaction Using the Finite Element Method. Advances in Powder Metallurgy, Vol. 1, T. Gasbarre and W.F. Jandeska, Editors, American Powder Metallurgy Institute, pp. 271-281.

Trasorras, J.R.L., Armstrong, S., McCabe, T.J., (1994). Modeling the Compaction of Steel Powder Parts. Advances in Powder Metallurgy & Particulate Materials-1994, Vol.7, American Powder Metallurgy Institute, pp. 33-50.

Trasorras, J.R.L., Krishnaswami, S., Goodby, L.V., Armstrong, S., (1995). Finite Element Modeling for the Design of Steel Powder Compaction. Advances in Powder Metallurgy & Particulate Materials-1995, Vol. 1, Part 3, Metal Powder Industries Federation, pp. 31-41.

Trasorras, J.R.L., Parameswaran, R., Cocks, A., (1998). Mechanical Behavior of Metal Powders and Powder Compaction Modeling. ASM Handbook, ASM International, Materials Park, OH, Vol. 7, pp. 326-342.

Trasorras, J.R.L., Parameswaran, R., (1999). Private Communication.

Walker, D.M., (1966). An Approximate Theory for Pressures and Arching in Hoppers. Chemical Engineering Science, Vol. 21, pp. 975-997.

Watson, T.J., Wert, J.A., (1993). On the Development of Constitutive Relations for Metallic Powders. Metallurgical Transactions A, Vol. 24, pp. 2071-2081.